Semileptonic $b \to c\tau\nu_\tau$ Decays as a Probe to Beyond Standard Model Physics

Srimoy Bhattacharya

A thesis
submitted for the degree of
Doctor of Philosophy

Department of Physics
Indian Institute of Technology Guwahati
Guwahati 781039, India

December 2018

Semileptonic $b \to c\tau\nu_\tau$ Decays as a Probe to Beyond Standard Model Physics

Srimoy Bhattacharya

A thesis
submitted for the degree of
Doctor of Philosophy

Supervisor:
Dr. Soumitra Nandi

Department of Physics
Indian Institute of Technology Guwahati
Guwahati 781039, India

December 2018

Declaration

The work in this thesis is based on research carried out at the Department of Physics, Indian Institute of Technology Guwahati, India under the supervision of Dr. Soumitra Nandi. No part of this thesis has been submitted elsewhere for award of any other degree or qualification. Works presented in the thesis are entirely my own unless referenced to the contrary in the text.

Signed: ____________________

Date: ____________________


भारतीय प्रौद्योगिकी संस्थान गुवाहाटी
Indian Institute of Technology Guwahati

Certificate

Dr. Soumitra Nandi
Assistant Professor
Department of Physics, IIT Guwahati
Email: soumitra.nandi@iitg.ernet.in

It is certified that the work contained in the thesis entitled **“Semileptonic $b \to c\tau\nu_\tau$ Decays as a Probe to Beyond Standard Model Physics”** by Mr. Srimoy Bhattacharya, a PhD student of the Department of Physics, IIT Guwahati was carried out under my supervision and has not been submitted elsewhere for award of any degree.

Dr. Soumitra Nandi

Acknowledgements

I am deeply thankful to my supervisor Dr. Soumitra Nandi for his constant guidance and involvement throughout this Ph.D. work. His positive energy always motivated me in my research. He always welcomed me whenever I knocked his door for a discussion. I learnt various aspects of high energy physics from these discussions. His enthusiasm and friendly behavior helped me a lot to interact with him. I am really privileged to work with him and once again express my gratitude to him.

I would also like to take this opportunity to thank the doctoral committee members Prof. Poulose Poulose, Dr. Arunansu Sil and Dr. K.V. Srikanth for reviewing my progress and for giving me valuable comments and suggestions. I specially thank my collaborator Dr. Sunando Patra for his support and valuable suggestions. I also thank all the high energy faculty members Dr. Subhaditya Bhattacharya, Dr. Debasish Borah, Dr. Sayan Chakrabarti, Dr. Sovon Chakraborty, Dr. Meduri C Kumar, Dr. Debaprasad Maity, Dr. Bibhas Ranjan Majhi,, Dr. Udit Raha and Dr. Bipul Bhuyan of IIT Guwahati for useful discussions and introducing me to various new topics in the journal club meetings. I also thank Prof. Paolo Gambino, Prof. Marco Ciuchini and Prof. Paride Paradisi for giving me the opportunity to visit INFN Turin, INFN Roma Tre and INFN Padova and fruitful discussions.

I thank Basab Bijoy Purkayastha for helping me on issues related to linux systems. I also thank all the anonymous peer reviewers for helping me with their critical thoughts which improved the quality of my publications.

I thank Dr. Biswajit Karmakar, Dr. Rashidul Islam, Dr. Asmita Das, Dr. Amit Dutta Banik for helping me to understand particle physics in my early days of Ph.D. It is my pleasure to thank my colleague Sneha Jaiswal, Lopamudra Mukherjee, Ipsita Ray for our endless interactions on physics as well as non-physics stuff. I also thank Rishav Roshan, Dibyendu Nanda, Kajal Samanta and Sayandeep for various discussions on different topics.

During my Ph.D tenure I also got several friends. I thank Basabendu and Krishnanjan for being there during my ups and downs and waste their precious time on me! Anabil da was always there to cheer me up. I also thank my good old friend Srikrishna for his

wisdom. I thank Asish da, Sourav da, Kallol da, Ramiz da and Abhijit da for being there every time.

Last but not the least, I am extremely grateful to my parents Mr. Sanjit Bhattacharya and Mrs. Parbati Bhattacharya and my sister Sreerupa and brother Sreejit for their love, support and encouragement throughout my career. I also thank Kalyan da for loving me throughout my life.

Abstract

In this thesis we have studied the semileptonic $b \to c\tau\nu_\tau$ decays which is found to be a sensitive probe of physics beyond standard model. Over the last few years, data for the semitaunic decays of B meson from different experimental collaborations have provided an excellent environment for testing the standard model in this sector. In particular, the measurements on $R(D^{(*)}) = \mathcal{B}(B \to D^{(*)}\tau\nu_\tau)/\mathcal{B}(B \to D^{(*)}\ell\nu_\ell)$ by *BABAR*, Belle and LHCb have shown some significant deviations from their SM predictions, indicating an indirect hint of new physics in $b \to c\tau\nu_\tau$ transitions. This thesis mainly focuses on two important aspects in the search of new physics via the above mentioned decays. First, the test of the new physics sensitivities of different observables associated with these decays in the future high luminosity experiments. In this regard, we have used the Optimal Observable technique which has been proven to be an useful tool in the collider searches. Here, for the first time we have applied this technique in the context of flavour physics observables. We have compared the sensitivities of different observables in $B \to D^{(*)}\tau\nu_\tau$ decays towards various new interactions. It has been also shown that the decay rate distributions could be an useful probe in discriminating different new interactions, in particular at very high luminosity. Secondly, we look for possible new physics scenarios in $b \to c\tau\nu_\tau$ decays that are most compatible with the available data using the Akaike Information Criterion. We have also updated the standard model predictions of the asymmetric and angular observables in $b \to c\tau\nu_\tau$ decays using the results of the recent up-to-date analysis in $B \to D^{(*)}\ell\nu_\ell$. Furthermore, in the selected scenarios with Akaike Information Criterion, best-fit values and correlations of the new parameters are extracted. Using these results, predictions are made on various observables in the exclusive and inclusive semitaunic $b \to c$ decays which can then be further checked for consistency with the future measurements. The graphical correlations among these observables are shown as well. These are found to be useful in discriminating various new physics scenarios.

List of Publications Included in the Thesis:

1. **“$b \to c\tau\nu_\tau$ Decays: A Catalogue to Compare, Constrain, and Correlate New Physics Effects”**
   S. Bhattacharya, S. Nandi and S. Kumar Patra.
   arXiv:1805.08222 [hep-ph]

2. **“Looking for possible new physics in $B \to D^{(*)}\tau\nu_\tau$ in light of recent data”**
   S. Bhattacharya, S. Nandi and S. K. Patra.
   arXiv:1611.04605 [hep-ph]
   DOI:10.1103/PhysRevD.95.075012
   Phys. Rev. D **95**, no. 7, 075012 (2017)

3. **“Optimal-observable analysis of possible new physics in $B \to D^{(*)}\tau\nu_\tau$”**
   S. Bhattacharya, S. Nandi and S. K. Patra.
   arXiv:1509.07259 [hep-ph]
   DOI:10.1103/PhysRevD.93.034011
   Phys. Rev. D **93**, no. 3, 034011 (2016)

Contents

List of Figures

List of Tables

Chapter 1

Introduction

A major endeavor of human civilization is to understand the laws of nature at their most fundamental level. In this process, practice of science enables us to dig into the very minute details of the universe both at microscopic and macroscopic levels. With the constant evolution in modern science, experimental discoveries and theoretical ideas have moved forward together. Today's tens of kilometers long particle accelerators in underground tunnels, that speed protons, antiprotons, electrons to near the speed of light and make them collide head-on with each other or with stationary targets are the modern versions of Rutherford's table-top experiment on the scattering of alpha particles. Over the years we have achieved several breakthroughs in understanding the nature but still there are some unsolved puzzles to be understood. Hence the purpose of constructing a successful theory is such that it can explain the observed phenomenon or make predictions which can be tested by future experiments to answer these open puzzles.

The Standard Model (SM) of particle physics, proposed and developed in 70's [1–3], is one of the most successful accomplishments of high energy physics to date. This is essentially considered as the mathematical compactification of our theoretical knowledge about elementary particles and their interactions. Over the last few decades, it has withstood rigorous experimental tests and all its predictions and parameters have been substantiated to an appreciable degree of accuracy. As an instance, for the muon's gyromagnetic ratio 'g', the standard model prediction of muon $g-2$ is accurate to 400 parts per billion. The Fermilab muon $g-2$ experiment tries to make a measurement of it with the precision of 140 parts per billion. The latest achievement of SM came from the evidence of the

Brout-Englert-Higgs field at CERN's Large Hadron Collider (LHC). In 2012, almost half a century after the prediction of Higgs boson [4, 5], the ATLAS [6] and CMS [7] collaboration discovered the Higgs. With this disclosure of the last missing piece of fundamental particles, the experimental validation of the SM was complete.

Keeping all these in mind and considering the standard model to be the most flourishing theory so far [8], there do exist some clear indications that this is not the ultimate theory to explain all the observed phenomena in nature. There are experimentally observed phenomenon which are unexplained and hence cannot be regarded as a complete theory of fundamental interactions. For example, the phenomenon of neutrino oscillations [9], the evidence the accelerating expansion of the universe [10], presence of dark matter [11] and the matter-antimatter asymmetry [12] cannot be explained within the framework of the SM. This model is also affected by some theoretical issues even within the Higgs sector, termed as Higgs mass hierarchy problem [13]. As we all know that Higgs is the only scaler candidate of SM due to which all the elementary particle posses their masses. But the first order radiative correction to the squared Higgs mass exhibits a quadratically divergent expression arising from the SM fermions in the loops, while considering the validity of the theory up to Planck scale (10^{19} GeV). There is no parameter within SM with which one can control this quadratic divergence of Higgs mass, unless some unnatural fine tuning is done order by order in the perturbation theory. The quadratic divergence in the mass renormalization of Higgs boson is related to the hierarchy problem which refers to the large gap ($\sim 10^{-16}$) between the two fundamental energy scales, electroweak (m_{EW}) and Planck (M_{Pl}). Another very striking feature of the charged fermion spectrum is the hierarchy of quark-lepton masses. Fermions in SM have different masses ranging from 0.5 MeV to 170 GeV. The origin of this hierarchical masses also cannot be explained within the framework of SM.

These puzzles suggest the necessity to extend the theory further. Any new physics (NP) search can follow one of two tracks : direct detection of new particles at the collider or indirect probes for new physics from precision measurements. As far as direct detection is concerned, so far, there are no evidences of beyond standard model (BSM) particles at the collider. In the second approach, the NP will be identified by their virtual effects. Hence, one needs to define various observables which could be predicted in the SM very precisely, and the NP can show up as tiny deviations in the measured values of one or many of those observables from their respecitve SM predictions.

It is well established that the B-meson system is one of the ideal scenarios to look for indirect effects of physics, both CP-conserving and CP-violating, beyond the standard model [14, 15]. Briefly the reasons are following:

- b-quark is heavier than charm, lighter than top. Top will not produce any hadrons. This heavy mass of b-quark corresponds to many theoretical niceties : Heavy Quark Symmetries (HQS), validity of parton model, etc. This also indicates that there are many final states and thus a scope of rich phenomenology.
- b-quark is quite stable. According to the Wolfenstein's parameterization the coupling of b-quark with the other two generations are small $\mathcal{O}(\lambda^2)$. Initially this feature indicated the measurement of CP violation in B decay. This was essentially the main reason of the widely spread enthusiasm for B physics.
- The short-distance box diagram with the top quark running inside the loop dominates the $B-\bar{B}$ mixing. Hence, CP-violation is large and this is calculable to a good precision. The long-distance part is anyway negligible in B decays. This can be compared with D decays where it is the dominant one.
- Dut to the m_c/m_b suppression, the soft QCD effects are less pronounced for B decays than for D.
- As the lifetime of B meson is sufficiently large, it can be accurately measured.

In early nineties, the least known CKM parameters concerned the third generation of quarks. Back then these parameters were indispensable to test the CKM sector of SM and imperative for venturing into the unchartered territories of said theory. In this context, semileptonic decays of B meson had played very important role in the extractions of the CKM elements and to understand the origin of CP violation in SM. Apart from $|V_{ub}|$, $|V_{cb}|$, $|V_{td}|$ and $|V_{ts}|$ most of the other CKM elements are measured with an accuracy less then 0.1%. Currently intensive research work is concentrated on studies of the semileptonic decays of B meson from both theoretical and experimental sides. In the SM, these decays are tree level processes so NP effects are expected to be small. Hence, the $B \to \pi\ell\nu_\ell$ and $B \to D^{(*)}\ell\nu_\ell$ ($\ell = e$ or μ) decays are analyzed for the extractions of V_{ub} and V_{cb}, respectively [16–26]. However, the $B \to D^{(*)}\tau\nu_\tau$ decays could be sensitive to NP because of the large τ mass. Several collaborations like *BABAR*, Belle and LHCb have observed these decays, and they have measured the ratios of the branching fractions like $R(D^{(*)}) = \mathcal{B}(B \to D^{(*)}\tau\nu_\tau)/\mathcal{B}(B \to D^{(*)}l\nu_l)$. One of the motivations for defining such observables is to test the Lepton Flavor Universality (LFU) of weak interactions, which is an important ingredient of the SM.

As an example, let us consider the decay of Z boson, the carrier for the neutral weak interaction, into two leptons. In the process of electron positron annihilation $e^+e^- \to \ell^+\ell^-$, we can observe this decay. SM prediction of the partial width $\Gamma_{\ell\ell}^{SM}$ for the decay $Z \to \ell^+\ell^-$ (at $m_\ell \to 0$) is 83.42 MeV. The experimental measurements of this leptonic decay width for different leptons results [27] :

$$\Gamma_{ee} = (83.96 \pm 0.15) MeV,$$
$$\Gamma_{\mu\mu} = (83.79 \pm 0.22) MeV,$$
$$\Gamma_{\tau\tau} = (83.72 \pm 0.26) MeV.$$

The measurement give similar values for all three final states. Hence, these numbers substantiate the LFU. However, over the past several years, data for the semitaunic decays of B meson from different experimental collaborations tell us a different story. In particular, the measurements on $R(D^{(*)})$ by *BABAR*, Belle and LHCb collaborations have shown some significant deviations from their SM predictions, indicating a possible signature of NP in $b \to c\tau\nu_\tau$. This thesis focuses on the indirect detections of NP via the virtual effects of the new particle(s) in the semi-leptonic decay of B meson, in particular, we have studied $b \to c\tau\nu_\tau$ decays in a model independent framework of NP. The possible signature of NP can be identified from the mismatch of experimental data with SM.

Theoretically, these hadronic decays are studied in an effective theory approach at an energy scale of b quark mass. In this approach, the effects of all the heavy degrees of freedom are encapsulated in the Wilson Coefficients (WC). These WCs are perturbatively calculable, and depend on the cut off scale of the respective theory. The WC relevant at the scale m_b could be obtained from those calculated at the high scale theory by an appropriate renormalization-group (RG) running. The main sources of uncertainties in hadronic decays or mixing are the non-perturbative matrix elements of the low energy effective operators. So far, methods are not available which will allow us to calculate those elements using the principles of QCD. As for example, in the semileptonic decays the main source of uncertainty is the form-factor. Therefore, in such decays the inputs from lattice QCD play an important role for a reliable predictions of the decay rate distributions, and many other observables like branching fraction, helicity fraction, asymmetries etc. At the moment, the SM accuracy is limited by the errors in the hadronic inputs. Hence, in order to identify the presence of BSM physics from the excess in the experimental data, accurate knowledge of hadronic inputs are crucial.

In the remaining part of chapter 1, after presenting a brief overview on flavor physics in SM (For detailed and involved reviews Ref.[28–32] can be useful.), a discussion on several observables which are important for $b \to c\tau\nu_\tau$ is provided. The current experimental status of these observables is presented thereafter.

1.1 Flavor in the standard model

Any discussion on particle physics will be incomplete without the knowledge of SM. It is the quantum field theory of fundamental interactions that accommodates the three fundamental forces of nature namely, strong, weak and electromagnetic forces. SM gauge theory is developed through the following steps :

- The gauge symmetry of the model : $\mathcal{G}_{SM} = SU(3)_c \times SU(2)_L \times U(1)_Y$. Here $SU(3)$ illustrates the strong interactions of colored quarks and gluons. $SU(2) \times U(1)$ models the electroweak interactions.

- The representation of the gauge fields :

  Here Q^i_L and L^i_L are the left-handed quark and lepton doublets respectively. u^i_R, d^i_R are the right handed up-type and down-type quark doublets and e^i_R are the right-handed lepton doublets. The only scaler ingredient of the SM is the Brout-Englert-Higgs (BEH) field, Φ.

- The non-zero vacuum expectation value of Higgs field Φ breaks the $SU(2)_L \times U(1)_Y$ symmetry spontaneously to $U(1)_{EM}$.

The most general renormalizable Lagrangian in SM can be split into three parts.

				$SU(3)_c$	$SU(2)_L$	$U(1)_Y$
$Q^i_L =$	$\begin{pmatrix} u_L \\ d_L \end{pmatrix}$	$\begin{pmatrix} c_L \\ s_L \end{pmatrix}$	$\begin{pmatrix} t_L \\ b_L \end{pmatrix}$	3	2	$\frac{1}{6}$
$u^i_R =$	u_R	c_R	t_R	3	1	$\frac{2}{3}$
$d^i_R =$	d_R	s_R	b_R	3	1	$-\frac{1}{3}$
$L^i_L =$	$\begin{pmatrix} \nu_{eL} \\ e_L \end{pmatrix}$	$\begin{pmatrix} \nu_{\mu L} \\ \mu_L \end{pmatrix}$	$\begin{pmatrix} \nu_{\tau L} \\ \tau_L \end{pmatrix}$	1	2	$-\frac{1}{2}$
$e^i_R =$	e_R	μ_R	τ_R	1	1	-1
$\Phi =$	$\begin{pmatrix} \phi^+ \\ \phi^0 \end{pmatrix}$			1	2	1/2

TABLE 1.1: The fermion fields of the standard model and their gauge quantum numbers.

$$\mathcal{L}_{SM} = \mathcal{L}_{kin} + \mathcal{L}_{Higgs} + \mathcal{L}_{Yukawa} \tag{1.1}$$

The kinetic part of the lagrangian, $\mathcal{L}_{kin}$ contains the gauge interactions through the covarient derivative and non-Abelian field strengths. Here, the covarient derivative is defined as :

$$D^\mu = \partial^\mu + ig_s G^\mu_a L_a + igW^\mu_b T_b + ig' B^\mu Y \tag{1.2}$$

Here G^μ_a are the eight gluon fields, W^μ_b the three weak interaction bosons and B^μ the single hypercharge boson. The L_as are $SU(3)_C$ generators, the T_bs are $SU(2)_L$ generators , and the Ys are the $U(1)_Y$ charges. The kinetic part of lagrangian has three parameters g, g' and g_s.

The Higgs lagrangian ($\mathcal{L}_{Higgs}$) brings the Maxican hat potential

$$\mathcal{L}_{Higgs} = \mu^2|\Phi|^2 - \lambda|\Phi|^4 \tag{1.3}$$

$\mathcal{L}_{Higgs}$ involves two parameters, λ and μ. Vacuum stability condition needs $\lambda > 0$. The pattern of sponteneous symmetry breaking (SSB) requires $\mu^2 < 0$.

The Yukawa lagrangian $\mathcal{L}_{Yukawa}$ contains

$$\mathcal{L}_{Yukawa} = y^e_{ij}\bar{L}^i \Phi e^j_R + y^d_{ij}\bar{Q}^i \Phi d^j_R + y^u_{ij}\bar{Q}^i \tilde{\Phi} u^j \tag{1.4}$$

The first term in Eq.(1.4) corresponds to the Lepton Yukawa term which involves three physical parameters (three charged lepton masses). Last two terms refer quark Yukawa interactions. This is the part where quarks masses and flavor arises. Yukawa interaction for the quarks are described by ten physical parameters. They can be chosen to be the six quark masses and the four parameters of the Cabibbo-Kobayashi-Maskawa (CKM) Matrix. The detailed discussion on this CKM matrix is given in the following subsection.

1.1.1 Cabibbo-Kobayashi-Maskawa Matrix

As a consequence of spontaneous symmetry breaking from $SU(2)_L \times U(1)_Y$ to $U(1)_{EM}$, Φ acquires a vacuum expectation value, $\langle \Phi \rangle = (0, v/\sqrt{2})$. Thus the quark sector of Eq.(1.4) yields Dirac mass terms for quarks of the form

$$\mathcal{L}_{mass,q} = m^d_{ij}\bar{d^i_L} d^j_R + m^u_{ij}\bar{u^i_L} u^j_R \tag{1.5}$$

where

$$m^q_{ij} = \frac{v}{\sqrt{2}} y^q_{ij} \tag{1.6}$$

These m^qs are not diagonal and contain many unphysical parameters. To remove these, we have to move from the flavor basis to mass basis by diagonalizing these matrices. For that, a bi-unitary transformation is performed. We can always find two unitary matrices V^q_L and V^q_R such that :

$$\hat{m}^q_{ij} = (V^q_L)_{ik} m^q_{kl} (V^{q\dagger}_R)_{lj} \tag{1.7}$$

With this diagonalization left chiral and right chiral fields are also rotated accordingly :

$$
\begin{aligned}
q_L^i &= (V_L^q)_{ij} q_L'^j \\
q_R^i &= (V_R^q)_{ij} q_R'^j
\end{aligned}
\qquad (1.8)
$$

In these two equations, left hand side corresponds to the interaction-basis field and in the right hand side we have shown the corresponding linear combination of mass-basis fields. In this thesis, from here on we will assume the mass basis and drop the prime.

As the mass matrices are proportional to the Yukawa matrices, in the mass basis, the Yukawa interactions are diagonal. But the coupling of W contains off-diagonal terms. From the interaction to mass basis, we get

$$
\mathcal{L}_{Wqq} = \frac{g}{\sqrt{2}} \bar{u}_L i\gamma_\mu d_L W^\mu \rightarrow \frac{g}{\sqrt{2}} \bar{u}_L i\gamma_\mu (V_{ul} V_{dl}^\dagger) d_L W^\mu \qquad (1.9)
$$

Here, due to the normalization of the $W^\pm$ states relative to the $W^{1,2}$ states, the $\sqrt{2}$ factor is coming in denominator. In Eq.(1.9) the term in parenthesis is identified as the famous CKM matrix [33, 34],

$$
V_{CKM} = V_{uL} V_{dL}^\dagger \qquad (1.10)
$$

As an outcome of non-diagonal V_{CKM}, the $W^\pm$ gauge bososns couple to quark mass eigenstates of different generations. Within the SM, this is the only source of flavor-changing quark interactions. The neutral current part of the lagrangian in the mass basis remains unchanged, i.e., in SM the flavor changing neutral currents (FCNC) are disallowed at tree level.

This CKM matrix has some very significant properties :

- The index structure of the CKM matrix is :

$$V_{CKM} = \begin{pmatrix} V_{ud} & V_{us} & V_{ub} \\ V_{cd} & V_{cs} & V_{c_b} \\ V_{td} & V_{ts} & V_{tb} \end{pmatrix} \tag{1.11}$$

- According to the definition of V_{CKM}, this is a product of two unitary matrices. Hence this itself is unitary, $V_{CKM}V^{\dagger}_{CKM} = \mathrm{I}$

- Using the unitarity condition and utilizing the freedom to arbitrary choose the global phases of the quark fields, we can actually reduce the initial nine unknown complex elements of V_{CKM} to three real numbers and one phase. This phase is the only source of CP-volation in SM.

Considering the fact that V_{CKM} is unitary and depends on only four independent physical parameters, the CKM matrix can be parametrized in several ways. Here we recall the two most popular ones. According to the Standard Parametrization [35] this matrix can be expressed as follows :

$$V_{CKM} = \begin{pmatrix} c_{12}c_{13} & s_{12}c_{13} & s_{13}e^{-i\delta} \\ -s_{12}c_{23} - c_{12}s_{23}s_{13}e^{-i\delta} & c_{12}c_{23} - s_{12}s_{23}s_{13}e^{-i\delta} & s_{23}c_{13} \\ s_{12}s_{23} - c_{12}c_{23}s_{13}e^{i\delta} & c_{12}s_{23} - s_{12}c_{23}s_{13}e^{-i\delta} & c_{23}c_{13} \end{pmatrix} \tag{1.12}$$

Here $c_{ij} \equiv cos\theta_{ij}$ and $s_{ij} \equiv sin\theta_{ij}$. The θ_{ij}s and δ are the three real mixing parameters and Kobayashi-Maskawa phase respectively. Experimental outcomes suggest $s_{13} << s_{23} << s_{12} << 1$. For a proper manifestation of this hierarchy, it is useful to choose a different parametrization. Wolfenstein parametrization [36] is the most popular one where all nine CKM matrix elements are parameterized by four parameters : (λ, A, ρ, η). Here $\lambda = |V_{us}|$ plays the role of an expansion parameter and η representing the CP-violating phase :

$$V_{CKM} = \begin{pmatrix} 1-\frac{1}{2}\lambda^2-\frac{1}{8}\lambda^4 & \lambda & A\lambda^3(\rho-i\eta) \\ -\lambda+\frac{1}{2}A^2\lambda^5[1-2(\rho+i\eta)] & 1-\frac{1}{2}\lambda^2-\frac{1}{8}\lambda^4(1+4A^2) & A\lambda^2 \\ A\lambda^3[1-(1-\frac{1}{2}\lambda^2)(\rho+i\eta)] & -A\lambda^2+\frac{1}{2}A\lambda^4[1-2(\rho+i\eta)] & 1-\frac{1}{2}A^2\lambda^4 \end{pmatrix} \tag{1.13}$$

1.1.2 Unitarity Triangle

The concept of Unitarity Triangle (UT) is very useful. Various relations among the matrix elements are coming from the unitarity condition of V_{CKM}, e.g.,

$$V_{ud}V_{us}^* + V_{cd}V_{cs}^* + V_{td}V_{ts}^* = 0, \tag{1.14}$$

$$V_{us}V_{ub}^* + V_{cs}V_{cb}^* + V_{ts}V_{tb}^* = 0, \tag{1.15}$$

$$V_{ud}V_{ub}^* + V_{cd}V_{cb}^* + V_{td}V_{tb}^* = 0. \tag{1.16}$$

Each of these equations can be geometrically represented in the complex plane as a triangle. The UT corresponding to Eq.(1.16) is depicted in fig. 1.1.

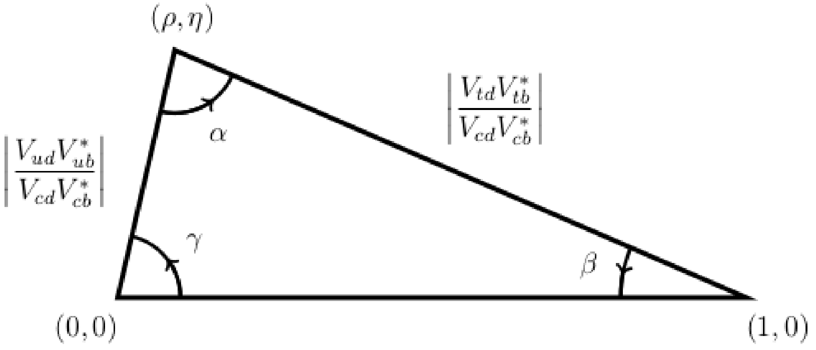

Fig. 1.1 Graphical representation of Eq.(1.16) as a UT in complex plane.

We can express the three angles of the above triangle α, β, γ in terms of the CKM parameters as :

$$\alpha = arg\Big(-\frac{V_{td}V_{tb}^*}{V_{ud}V_{ub}^*}\Big), \quad \beta = arg\Big(-\frac{V_{td}V_{tb}^*}{V_{ud}V_{ub}^*}\Big), \quad \gamma = arg\Big(-\frac{V_{ud}V_{ub}^*}{V_{cd}V_{cb}^*}\Big) \tag{1.17}$$

The length of the sides of the UT can be identified in terms of these parameters as follows:

$$R_u = \left|\frac{V_{ud}V_{ub}^*}{V_{cd}V_{cb}^*}\right| = \sqrt{\rho^2+\eta^2}, \quad R_t = \left|\frac{V_{td}V_{tb}^*}{V_{cd}V_{cb}^*}\right| = \sqrt{(1-\rho)^2+\eta^2} \tag{1.18}$$

The remaining side is, by normalization, set to unity.

1.1.3 Determination of CKM parameters

With the economical structure of CKM matrix having only four independent parameters and its consequences for CP-violation, we can determine these matrix elements through several quark level transitions. In this regard, different experimental collaborations around the globe have performed extensive measurements on K, D, and B mesons. The measurements of most of the observables in K meson decays are obtained from some dedicated experiments like NA48 [37], KLOE [38, 39], and KTeV. Initial measurements of CKM parameters which are related to D and B meson observables were performed by ARGUS [40] at DESY,CLEO, and CLEO-c [41] at Cornell, followed by the B factory experiments *BABAR* [42] at SLAC and Belle [43] at KEK. Previously these were operated at a center-of-mass energy corresponding to the mass of the $\Upsilon(4S)$ resonance. Significant contributions also came from the CDF and D0 experiments at FNAL [44], especially for the obervables involving B_s mesons which are not accessible at the $\Upsilon(4S)$ resonance. These experiments have been terminated, whereas Belle is being upgraded [45]. Over the last decade, LHCb experiment at LHC is playing an important role in the determination of the CP- observables via the study of B_s decays and mixing. The general-purpose detector experiments ATLAS [46] and CMS [47] contribute in selected areas, and the BESIII experiment [48] also provides many results for charm hadrons.

To determine the magnitudes of the CKM matrix elements, we need to use a number of sophisticated theoretical and experimental techniques. Based on the type of decay process useful for the measurements, they are classified in two distinct way. One is the direct measurement which involves the tree level processes in SM and the other one is the indirect measurement where we consider the loop level processes. The measurements of the elements related to u-quark and c-quark (ie. $|V_{ud}|$,$|V_{us}|$,$|V_{ub}|$,$|V_{cd}|$,$|V_{cs}|$,$|V_{cb}|$) is attained by the direct measurements. Among rest of the three elements related to t-

	Dominated by experimental uncertainties		Dominated by theoretical uncertainties	
	Process	Constraint	Process	Constraint
Tree	$B \to D^{(*)}K^{(*)}$	γ	$B \to D^{(*)}\ell\nu$	$\lvert V_{cb}\rvert$ versus form factor $F^{B\to D^{(*)}}$
			$B \to X_c\ell\nu$	$\lvert V_{cb}\rvert$ versus OPE
			$B \to \pi\ell\nu$	$\lvert V_{ub}\rvert$ versus form factor $F^{B\to\pi}$
			$B \to X_u\ell\nu$	$\lvert V_{ub}\rvert$ versus OPE
			$M \to \ell\nu$	$\lvert V_{UD}\rvert$ versus decay constant f_M
			$M \to N\ell\nu$	$\lvert V_{UD}\rvert$ versus form factor $F^{M\to N}$ or $M \to N$ amplitude
Loop	$B \to (c\bar{c})K^{(*)}$	β	ϵ_K ($K\overline{K}$ mix)	$V_{ts}V_{td}^*$ and $V_{cs}V_{cd}^*$ versus bag parameter B_K
	$B \to \pi\pi, \rho\pi, \rho\rho$	α	Δm_d ($B^0\bar{B}^0$ mix)	$\lvert V_{tb}V_{td}^*\rvert$ versus bag parameter B_{B^0}
	$\mathrm{B_s} \to J/\psi\phi$	β_s	Δm_s ($B_s^0\bar{B}_s^0$ mix)	$\lvert V_{tb}V_{ts}^*\rvert$ versus bag parameter $B_{B_s^0}$

Table 1.2: A partial list of measurements generally used to determine the CKM parameters. The measurements are classified according to the dominant type of uncertainties (experimental or theoretical) and the type of processes involved (tree or loop). Abbreviation: OPE, operator product expansion.

quark, V_{tb} is determined from top quark decays with b-quark reconstruction or from single top production processes. The rest of two elements, V_{ts} and V_{td} are determined by the indirect measurements through the one loop level FCNC processes.

Table 1.2 [49] summaries the processes for which a good accuracy can be reached in the measurements of CKM matrix elements both experimentally and theoretically. These processes are used to assess the validity of the Kobayashi–Maskawa mechanism for CP-violation and to perform the metrology of the CKM parameters, assuming the validity of the SM.

The UT angles α, β, γ mentioned in the left pannel of the table 1.2 can be determined experimentally from CP-violating measurements with less theoretical uncertainties ($\leq$ 10%). Current world average which includes the measurements from LHCb [50] and B Factories [22] have determined the value of β as $\sin 2\beta = 0.691 \pm 0.017$ in charmonium decays, which is the most precise constraints on UT. In case of the UT angle α, fig. 1.1 shows that it is the angle between $V_{tb}^*V_{td}$ and $V_{ub}^*V_{ud}$. Therefore the time-dependent CP-asymmetries in the decay mode $b \to u\bar{u}d$ can directly measure $\sin 2\alpha$. So far, all the measurements for α has been performed in $B \to \pi\pi$, $\rho\pi$ and $\rho\rho$ decay modes. Combining all of these decay modes [22, 51], the recent value of α is $\alpha = (84.5^{+5.9}_{-5.2})^\circ$. Again, From Eq.1.17 we get that the definition of γ is independent of CKM elements involving top quark. Hence it can be measured in tree level B decays like $B \to D^{(*)}K^{(*)}$ channels. Here the CP violating phase occurs in the interference of $b \to c$ and $b \to u$ topologies followed by carefully chosen D decay process. Depending on this subsequent D meson decay, three different methodologies,(The Gronau-London-Wyler (GLW) method [52, 53], Atwood-Dunietz-Soni (ADS) method [54, 55], Grossman-Soffer-Zupan (GGSZ) method (based on Dalitz analysis) [56]) have been devised to obtain the information about γ. Combining all these three methods, the recent update on γ is $\gamma = (73.5^{+4.2}_{-5.1})^{\circ}$. Figure 1.2 depicts the $\bar{\rho} - \bar{\eta}$ plane showing the result of the SM fit by UTfit collaboration [57] using only the UT angles as constraints. The black contours display the 68% and 95% probability regions selected by the given global fit.

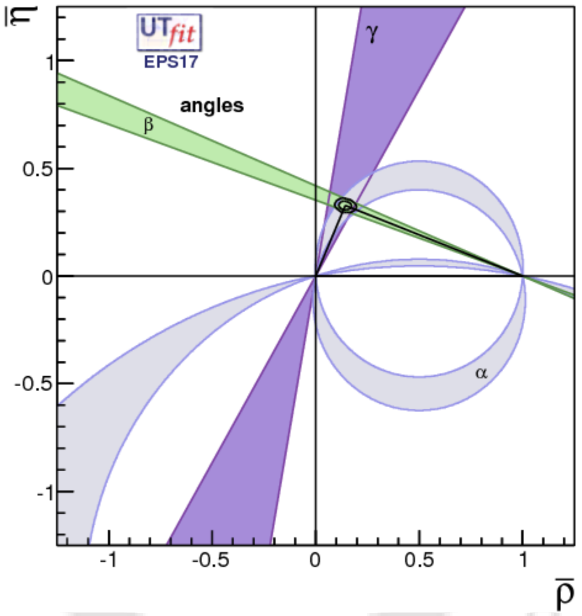

Fig. 1.2 $\bar{\rho} - \bar{\eta}$ plane showing the result of the SM fit by UTfit collaboration.

In the right panel of table 1.2, the decays relevant to measure the moduli of different CKM matrix elements are enlisted. Here, among all these matrix elements, $|V_{ub}|$ and $|V_{cb}|$ play a major role to identify the apex of UT in the (ρ, η) plane. The semileptonic decays $b \to c\ell\nu$ where $(\ell = e, \mu)$ are crucial for the determination of $|V_{cb}|$. These semileptonic decays, being tree level, at the lowest order in SM, are expected to be free from any new physics effects, hence provide a clean environment for the measurement of the V_{cb}. It can be extracted from both exclusive decays, like $B \to D^{(*)}\ell\nu$ and inclusive decays, like $B \to X_c\ell\nu$. The inclusive and exclusive semi-leptonic searches rely on different theoretical calculations. For the inclusive decay, the decay rate can be described through the Operator Product Expansion (OPE) [58, 59] and the non perterbative unknowns can be fitted from final state lepton and hadron energy distribution.

Hence, in the SM, precise predictions with reliable uncertainties are possible. On the other hand for the exclusive decays, the non-perturbative unknowns are the hadronic formfactors. It is hard to extract these formfactors directly from the experimental information alone. Here, we need to rely on Heavy Quark Effective Theory (HQET) and lattice inputs [60]. At the moment, the most precise determinations of $|V_{cb}|$ from inclusive [22] and exclusive decays [26] are $(42.19 \pm 0.78) \times 10^{-3}$ and $(40.90 \pm 0.94) \times 10^{-3}$, respectively. As the possibility of NP to explain this discripency is ruled out by electrowek constraints on the effective $Zb\bar{b}$ vertex the underestimation of theoretical and/or experimental uncertainties in semileptonic decays can be a plausible explanetion of this mismatch.

1.2 New Physics and the Observables

As mentioned in the last subsection, being a tree level process, semileptonic decays $b \to c\ell\nu$, where $\ell = e, \mu$, are expected to be free from any NP effects. However, the mass of τ lepton being large compared to the other observed leptons, measurements of branching fractions and the other related observables in semileptonic decays of B meson to τ can be interesting for an indirect probe of NP. Here, the large τ mass can uplift the helicity suppression of certain semileptonic decay amplitudes which are unobserved in decays with light leptons in the final state. Moreover, $B \to D^*\tau\nu_\tau$ decay having two detectable particles of nonzero spin in the final state (D^*, τ) offers the opportunity to investigate the structure of possible NP contribution to $b \to c\tau\bar{\nu_\tau}$ transitions [61]. The experimental reconstruction of D^* in the $D\pi$ final state allows one to obtain the helicity structure of this state directly. Similarly the τ lepton helicity can be inferred from the decay to $\pi\nu_\tau$ final state [62, 63]. This means that a number of experimental observables sensitive to possible NP effects, can be introduced.

1.2.1 New Operators

There are varieties of NP models that can contribute to $b \to c\tau\nu_\tau$ decays , and the characteristics of each of those models could be very different from each other. For example, two higgs doublet model (2HDM) has only scalar-type of interactions ; new gauge bosons Z' and W' interact via vector currents ; the models with leptoquarks have both scalar and/or vector effective operators [64], while, the extra dimensional models have tensor interaction in addition to scalar or vector-type of interactions [65].

In an effective theory framework, one can write down the most general effective new operators which may include new scalar, vector and tensor currents other than those in SM, to analyse these $b \to c\tau\nu_\tau$ decays. The most general effective Hamiltonian describing the $b \to c\ell\nu_\ell$ transitions (where $\ell = e$, μ or τ) with all possible four-fermion operators in the lowest dimension is given by [66],

$$\mathcal{H}_{eff} = \frac{4G_F}{\sqrt{2}} V_{cb} \Big[(\delta_{\ell\tau} + C^{\ell}_{V_1}) \mathcal{O}^{\ell}_{V_1} + C^{\ell}_{V_2} \mathcal{O}^{\ell}_{V_2} + C^{\ell}_{S_1} \mathcal{O}^{\ell}_{S_1} + C^{\ell}_{S_2} \mathcal{O}^{\ell}_{S_2} + C^{\ell}_{T} \mathcal{O}^{\ell}_{T} \Big], \tag{1.19}$$

where the operator basis is defined as

$$\begin{aligned}
\mathcal{O}^{\ell}_{V_1} &= (\bar{c}_L \gamma^{\mu} b_L)(\bar{\tau}_L \gamma_{\mu} \nu_{\ell L}), \\
\mathcal{O}^{\ell}_{V_2} &= (\bar{c}_R \gamma^{\mu} b_R)(\bar{\tau}_L \gamma_{\mu} \nu_{\ell L}), \\
\mathcal{O}^{\ell}_{S_1} &= (\bar{c}_L b_R)(\bar{\tau}_R \nu_{\ell L}), \\
\mathcal{O}^{\ell}_{S_2} &= (\bar{c}_R b_L)(\bar{\tau}_R \nu_{\ell L}), \\
\mathcal{O}^{\ell}_{T} &= (\bar{c}_R \sigma^{\mu\nu} b_L)(\bar{\tau}_R \sigma_{\mu\nu} \nu_{\ell L}),
\end{aligned} \tag{1.20}$$

and the corresponding Wilson coefficients are given by C^{ℓ}_{W} ($W = V_1, V_2, S_1, S_2, T$). In this basis, neutrinos are assumed to be left handed.

1.2.2 Observables

In this subsection, we discuss several important observables in different channels of $b \to c\tau\nu_\tau$ decays which are potentially sensitive to various new physics interactions mentioned in Eq. (1.20). It is possible that different observables will be affected differently by a particular type of NP. Hence in different NP scenarios, correlation studies among these observables will be an important probe for an indirect detection of NP.

1.2.2.1 $B \to D^{(*)}\tau\nu_\tau$

The complete expressions for the q^2-distributions of the differential decay rates $d\Gamma/dq^2$ in $B \to D^{(*)}\tau\nu_\tau$ decays, obtained using the effective Hamiltonian in Eq.(1.19), are given by [67]

$$
\begin{aligned}
\frac{d\Gamma\left(\overline{B} \to D\tau\overline{\nu}_\tau\right)}{dq^2} &= \frac{G_F^2\,|V_{cb}|^2}{192\pi^3 m_B^3} q^2 \sqrt{\lambda_D(q^2)} \left(1-\frac{m_\tau^2}{q^2}\right)^2 \bigg\{ |1+C_{V_1}+C_{V_2}|^2 \bigg[\bigg(1+\frac{m_\tau^2}{2q^2}\bigg) H_{V,0}^{s2} \\
&\quad + \frac{3}{2}\frac{m_\tau^2}{q^2} H_{V,t}^{s2}\bigg] + \frac{3}{2}\,|C_{S_1}+C_{S_2}|^2\, H_S^{s2} + 8\,|C_T|^2 \left(1+\frac{2m_\tau^2}{q^2}\right) H_T^{s2} + 3\mathcal{R}e\left[(1+C_{V_1}+C_{V_2})\right. \\
&\quad \left.\left(C_{S_1}^* + C_{S_2}^*\right)\right] \frac{m_\tau}{\sqrt{q^2}} H_S^s H_{V,t}^s - 12\mathcal{R}e\left[(1+C_{V_1}+C_{V_2})\, C_T^*\right] \frac{m_\tau}{\sqrt{q^2}} H_T^s H_{V,0}^s \bigg\}\,,
\end{aligned}
\tag{1.21}
$$

and

$$
\begin{aligned}
\frac{d\Gamma\left(\overline{B} \to D^*\tau\overline{\nu}_\tau\right)}{dq^2} &= \frac{G_F^2\,|V_{cb}|^2}{192\pi^3 m_B^3} q^2 \sqrt{\lambda_D^*(q^2)} \left(1-\frac{m_\tau^2}{q^2}\right)^2 \bigg\{ \left(|1+C_{V_1}|^2 + |C_{V_2}|^2\right) \bigg[\left(1+\frac{m_\tau^2}{2q^2}\right) \\
&\quad \left(H_{V,+}^2 + H_{V,-}^2 + H_{V,0}^2\right) + \frac{3}{2}\frac{m_\tau^2}{q^2} H_{V,t}^2\bigg] - 2\mathcal{R}e\left[(1+C_{V_1})\, C_{V_2}^*\right] \bigg[\left(1+\frac{m_\tau^2}{2q^2}\right) \left(H_{V,0}^2 + 2H_{V,+}H_{V,-}\right) \\
&\quad + \frac{3}{2}\frac{m_\tau^2}{q^2} H_{V,t}^2\bigg] + \frac{3}{2}\,|C_{S_1}-C_{S_2}|^2\, H_S^2 + 8\,|C_T|^2 \left(1+\frac{2m_\tau^2}{q^2}\right) \left(H_{T,+}^2 + H_{T,-}^2 + H_{T,0}^2\right) \\
&\quad + 3\mathcal{R}e\left[(1+C_{V_1}-C_{V_2})\left(C_{S_1}^* - C_{S_2}^*\right)\right] \frac{m_\tau}{\sqrt{q^2}} H_S H_{V,t} \\
&\quad - 12\mathcal{R}e\left[(1+C_{V_1})\, C_T^*\right] \frac{m_\tau}{\sqrt{q^2}} \left(H_{T,0}H_{V,0} + H_{T,+}H_{V,+} - H_{T,-}H_{V,-}\right) \\
&\quad + 12\mathcal{R}e\left[C_{V_2} C_T^*\right] \frac{m_\tau}{\sqrt{q^2}} \left(H_{T,0}H_{V,0} + H_{T,+}H_{V,-} - H_{T,-}H_{V,+}\right) \bigg\}\,.
\end{aligned}
\tag{1.22}
$$

where $\lambda_D^{(*)}(q^2) = ((m_B - m_D^{(*)})^2 - q^2)((m_B + m_D^{(*)})^2 - q^2)$. Here, the helicity amplitudes $H_{i,\lambda}^{\lambda_M}$'s are defined through the hadronic matrix elements

$$H_{i,\lambda}^{\lambda_M} = \epsilon_\mu^* \langle M(\lambda_M)|\bar{c}\gamma^\mu(1-\gamma_5)b|\bar{B}\rangle, \tag{1.23}$$

where λ_M and λ are the helicities of the final state meson M and the virtual intermediate boson in the B meson rest frame respectively. Also note that whereas for D meson $\lambda_M = s$, for D^* meson $\lambda_M = \pm 1,\ 0$ and $\lambda = 0,\ \pm 1$ and t. These helicity amplitudes are related to the form-factors (f_+ and f_0 for $B \to D$ and V,A_0,A_1 and A_2 for $B \to D^*$) as follows :

$$\begin{aligned}
H_{V,0}^s(q^2) &= \sqrt{\frac{\lambda_D(q^2)}{q^2}} f_+(q^2), \\
H_{V,t}^s(q^2) &= \frac{m_B^2 - m_D^2}{\sqrt{q^2}} f_0(q^2), \\
H_{V,\pm}(q^2) &= (m_B + m_{D^*})A_1(q^2) \mp \frac{\sqrt{\lambda_{D^*}}}{m_B + m_{D^*}} V(q^2), \\
H_{V,0}(q^2) &= \frac{(m_B + m_{D^*})}{2m_{D^*}\sqrt{q^2}} \Big[(m_B^2 - m_{D^*}^2 - q^2)A_1(q^2) + \frac{\lambda_{D^*}}{(m_B + m_{D^*})^2} A_2(q^2)\Big] \\
H_{V,t}(q^2) &= \sqrt{\frac{\lambda_D(q^2)}{q^2}} A_0(q^2)\,.
\end{aligned} \tag{1.24}$$

Here, the form-factors are defined as the matrix elements of various currents,

$$\begin{aligned}
\langle D(K)|\bar{c}\gamma_\mu b|\bar{B}(p)\rangle = [(p+k)_\mu - \frac{m_B^2 - m_D^2}{q^2} q_\mu] f_+(q^2) \\
+ q_\mu \frac{m_B^2 - m_D^2}{q^2} f_0(q^2)\,,
\end{aligned} \tag{1.25}$$

and

$$\begin{aligned}
\langle D^*(k,\varepsilon)|\bar{c}\gamma_\mu b|\bar{B}(p)\rangle &= i\epsilon_{\mu\nu\rho\sigma}\varepsilon^{\nu *} p^\rho k^\sigma \frac{2V(q^2)}{m_B + m_{D^*}} \\
\langle D^*(k,\varepsilon)|\bar{c}\gamma_\mu\gamma_5 b|\bar{B}(p)\rangle &= \varepsilon_\mu^*(m_B + m_{D^*})A_1(q^2) \\
&\quad - (p+k)_\mu(\varepsilon^* q)\frac{A_2(q^2)}{m_B + m_{D^*}} \\
&\quad - q_\mu(\varepsilon^* q)\frac{2m_{D^*}}{q^2}[A_3(q^2) - A_0(q^2]\,,
\end{aligned} \tag{1.26}$$

where

$$A_3(q^2) = \frac{m_B + m_{D^*}}{2m_{D^*}} A_1(q^2) - \frac{m_B - m_{D^*}}{2m_{D^*}} A_2(q^2)\,. \tag{1.27}$$

In the HQET the above matrix elements are defined as [68]

$$\langle D(v')|\bar{c}\gamma_\mu b|\bar{B}(v)\rangle = \sqrt{m_B m_D}\left[h_+(w)(v+v')_\mu + h_-(w)(v-v')_\mu\right]\,, \tag{1.28a}$$

$$\begin{aligned}
\langle D^*(v',\varepsilon)|\bar{c}\gamma_\mu b|\bar{B}(v)\rangle &= i\sqrt{m_B m^*_D}\, h_V(w)\epsilon_{\mu\nu\rho\sigma}\varepsilon^{*\nu} v'^{\rho} v^{\sigma}\,, \\
\langle D^*(v',\varepsilon)|\bar{c}\gamma_\mu\gamma_5 b|\bar{B}(v)\rangle &= \sqrt{m_B m_{D^*}}\,\big[h_{A_1}(w)(w+1)\varepsilon^*_\mu \\
&\quad - (\varepsilon^*\cdot v)(h_{A_2}(w)v_\mu + h_{A_3}(w)v'_\mu)\big]\,,
\end{aligned} \tag{1.28b}$$

where $v = p_B/m_B$, $v' = k/m_{D^{(*)}}$ and $w(q^2) = v \cdot v' = (m_B^2 + m_{D^{(*)}}^2 - q^2)/2m_B m_{D^{(*)}}$. Here, $h_i(w)$s are the HQET formfactors, and they are related by heavy quark symmetry. In the heavy quark limit, these are either vanish or are proportional to the Isgur-Wise function $\xi(w)$. A direct comparison of the matrix elements in Eq.(1.25) and (1.28) gives us the relations

$$\begin{aligned}
f_+(q^2) &= \frac{1}{2\sqrt{m_B m_D}}\Big[(m_B+m_D)h_+(w(q^2)) - (m_B-m_D)h_-(w(q^2))\Big] \\
f_0(q^2) &= \frac{1}{2\sqrt{m_B m_D}}\Big[\frac{(m_B+m_D)^2-q^2}{m_B+m_D}h_+(w(q^2)) - \frac{(m_B-m_D)^2-q^2}{m_B-m_D}h_-(w(q^2))\Big]\,.
\end{aligned} \tag{1.29}$$

The proper parameterization of these different form factors has been the subject of intense inspection, motivated specifically by the need to extrapolate the information obtained in a restricted q^2 region to the whole q^2 range. There are different ways of parameterising the form factors. For the $B \to D^{(*)}$ decays two different approaches are there in the literature which are commonly known as CLN (Caprini-Lellouch-Neubert) and BGL (Boyd-Grinstein-Lebed) parameterisation. In the CLN parameterisations of the form factors, HQET plays an important role. In the limit $m_{b/c} >> \Lambda_{QCD}(=$ hadronic scale) the HQET form factors are either zero or equal to the Isgur-Wise function $\xi(w)$, corrections to this limit at order α_s and $1/m_b^2$ are fully known, for recent updates see [69]. The form factors and few ratios of them are evaluated at $w = 1$, the extrapolations to other values of w are done by using an expansion around $w = 1$. In the BGL parameterisations, the form factors are defined as an Taylor series expansion about $z = 0$, where z is defined as $z(w) = (\sqrt{w+1} - \sqrt{2})/(\sqrt{w+1} + \sqrt{2})$. The key ingredient in this approach is the transformation that maps the complex q^2 plane onto the unit disc $|z| \leq 1$, for more details see [70].

In our analysis, we have followed the CLN parametrization given in [68] where the HQET form-factors can be expressed as

$$\begin{aligned} h_+(w) &= \frac{1}{2(1+r_D^2-2r_Dw)}\Big[-(1+r_D)^2(w-1)V_1(w) \\ &\quad +(1-r_D)^2(w+1)S_1(w)\Big] \\ h_-(w) &= \frac{(1-r_D^2)(w+1)}{2(1+r_D^2-2r_Dw)}\left[S_1(w)-V_1(w)\right], \end{aligned} \tag{1.30}$$

where $r_D = m_D/m_B$. As mentioned earlier, the hadronic form-factors $V_1(w)$ and $S_1(w)$ coincide with the Isgur-Wise function $\xi(w)$ in the infinite mass limit of the heavy quark m_Q ($= m_b$ or m_c). Here, the form factors $V_1(w)$ and $S_1(w)$ are related to $f_+(w)$ and $f_0(w)$ by the following relations

$$f_+(w) = \frac{1+r_D}{2\sqrt{r_D}}V_1(w), \quad f_0(w) = (1+w)\frac{\sqrt{r_D}}{1+r_D}S_1(w) \tag{1.31}$$

This function is normalized to unity at zero recoil, i.e at $w = 1$. In the Ref. [68], the w dependence is parameterized as given in the below equation:

$$V_1(w) = V_1(1) \times \left(1 - 8\rho_D^2 z(w) + (51\rho_D^2 - 10)z(w)^2 - (252\rho_D^2 - 84)z(w)^3\right). \tag{1.32}$$

Here, the idea is to expand $V_1(w)$ around zero recoil point $w = 1$. $V_1(1)$ includes corrections at order $\alpha_s(m_Q)$ and Λ_{QCD}/m_Q in HQET. Latest lattice calculation predict the value of $V_1(w)$ at zero recoil i.e $V_1(1) = 1.053 \pm 0.008$ [71]. On the other hand, ρ_D^2 can be fitted directly from the data on $\Gamma(B \to D\ell\nu_\ell)$, where $\ell = e,\ \mu$[1], and the fitted value is given by $\rho_D^2 = 1.186 \pm 0.054$, for details see [72].

In principle, lattice calculations can provide useful informations about the form factors at $w = 1$ as well as at non-zero recoils (i.e $w \neq 1$), which are allowed by the kinematically

---

[1] From hereon, ℓ will mean light leptons, i.e. e and μ, unless specified otherwise.

$h_{A_1}(w)$ $R_1(w)$ & $R_2(w)$	Value from LCSR						
$h_{A_1}(w_{max})$	0.65(18)						
$R_1(w_{max})$	1.32 (4)						
$R_2(w_{max})$	0.91 (17)						
$f_+(w)$ & $f_0(w)$	Value from HPQCD	Correlation					
$f_+(1)$	1.178(46)	1.	0.994	0.975	0.507	0.515	0.522
$f_+(1.06)$	1.105(42)		1.	0.993	0.563	0.576	0.587
$f_+(1.12)$	1.037(39)			1.	0.617	0.634	0.649
$f_0(1)$	0.902(41)				1.	0.997	0.988
$f_0(1.06)$	0.870(39)					1.	0.997
$f_0(1.12)$	0.840(37)						1.
	Value from MILC						
$f_+(1)$	1.1994(95)	1.	0.967	0.881	0.829	0.853	0.803
$f_+(1.08)$	1.0941(104)		1.	0.952	0.824	0.899	0.886
$f_+(1.16)$	1.0047(123)			1.	0.789	0.890	0.953
$f_0(1)$	0.9026(72)				1.	0.965	0.868
$f_0(1.08)$	0.8609(77)					1.	0.952
$f_0(1.16)$	0.8254(94)						1.

TABLE 1.3: Lattice QCD results of f_+ and f_0 for different values of w. The upper half of the table have been obtained using the fit results from the HPQCD collaboration [73], and the lower half are the results obtained by the Fermilab MILC collaboration [71].

accessible regions of the decay. At the moment, lattice groups like HPQCD and Fermilab MILC have predicted $f_+(w)$ and $f_0(w)$ at $w = 1$ as well as for few other values of w ($\neq 1$), for detail see the table 1.3.

Following [63], the w dependence of $S_1(w)$ can be parameterized as

$$S_1(w) = V_1(w) \times \left\{1 + \Delta[-0.019 + 0.041(w-1) - 0.015(w-1)^2]\right\}, \tag{1.33}$$

Here, Δ parameterizes the unknown higher order corrections in HQET. In a couple of analysis, for the prediction of the $R(D)$, Δ is assumed to have 100% error [63]. The decay rate $\Gamma(B \to D\ell\nu_\ell)$ is not useful to fit the parameters of $S_1(w)$, as it is not sensitive to the decay rates because of the negligible lepton masses. In this context, it is important to note that the Δ dependence of the hadronic form factor $S_1(w)$ makes this formalism very imprecise. With the implementation of NLO HQET calculation we can express the ratio f_0/f_+ a follows [74]:

$$\begin{aligned} f_+(z) &\approx f_+(0)\Big[1 - 8\rho^2 z + (51\rho^2 - 10)z^2 - (252\rho^2 - 84)^3\Big] \\ \frac{f_0(z)}{f_+(z)} &\approx \left(\frac{2\sqrt{r_D}}{1+r_D}\right)^2 \frac{1+w}{2} 1.0036\Big[1 - 0.0068(w-1) + 0.0017(w-1)^2 - 0.0013(w-1)^3\Big], \end{aligned} \tag{1.34}$$

here, $f_+(0) = \mathcal{G}(1)\left(\frac{1+r_D}{2r_D}\right)$ and $\mathcal{G}(1)$ is the zero-recoil form factor.

In case of $B \to D^*\tau\nu$ decay, as shown in Eq. (1.26), there are four independent hadronic form-factors: V, A_0, A_1 and A_2, which are related to HQET form-factors (Eq. (1.28) by the following relations [75]:

$$\begin{aligned} V(w) &= \frac{R_1(w)}{r_{D^*}} h_{A_1}(w)\,, \\ A_1(w) &= \frac{1}{2} r_{D^*}(w+1) h_{A_1}(w)\,, \\ A_2(w) &= \frac{R_2(w)}{r_{D^*}} h_{A_1}(w)\,, \\ A_0(w) &= \frac{R_0(w)}{r_{D^*}} h_{A_1}(w) \end{aligned} \tag{1.35}$$

where $r_{D^*} = 2\sqrt{m_B m_{D^*}}/(m_B + m_{D^*})$. The w dependencies of the HQET form-factors are parameterized following the ref. [68],

$$\begin{aligned} h_{A_1}(w) =& h_{A_1}(1)\left[1 - 8\rho^2_{D^*} z(w) + (53\rho^2_{D^*} - 15) z(w)^2 - (231\rho^2_{D^*} - 91) z(w)^3\right]\,, \\ R_1(w) =& R_1(1) - 0.12(w-1) + 0.05(w-1)^2\,, \\ R_2(w) =& R_2(1) + 0.11(w-1) - 0.06(w-1)^2\,, \\ R_0(w) =& R_0(1) - 0.11(w-1) + 0.01(w-1)^2\,. \end{aligned} \tag{1.36}$$

Here, the current lattice prediction is $h_{A_1}(1) = 0.906 \pm 0.013$ [76], the rest of the three parameters like ρ_{D^*}, $R_1(1)$, $R_2(1)$ are fitted directly from the decay rate $\Gamma(B \to D^*\ell\nu_\ell)$

[72],

$$\begin{aligned} \rho^2_{D^*} &= 1.207 \pm 0.026, & C\left(\rho^2_{D^*},\ R_1(1)\right) &= 0.568, \\ R_1(1) &= 1.406 \pm 0.033, & C\left(\rho^2_{D^*},\ R_2(1)\right) &= -0.809, \\ R_2(1) &= 0.853 \pm 0.020, & C\left(R_1(1),\ R_2(1)\right) &= -0.758, \end{aligned} \tag{1.37}$$

where the second column lists the correlations between the parameters. As $B \to D^*\ell\nu$ decays are not sensitive to $R_0(w)$, there is only theoretical estimate available on $R_0(1) = 1.14 \pm 0.07$, based on HQET [75].

In a very recent analysis [26], the above mentioned parameters are fitted using the updated inputs from lattice and light cone sum rule (LCSR) (table 1.3) along with the complete sets of available data on the angular and q^2-distributions of the $B \to D^{(*)}\ell\nu_\ell$ decays. The fitted values are given as:

$$\begin{aligned} \rho^2_{D^*} &= 1.251 \pm 0.113, & C\left(\rho^2_{D^*},\ R_1(1)\right) &= 0.858, \\ R_1(1) &= 1.371 \pm 0.036, & C\left(\rho^2_{D^*},\ R_2(1)\right) &= -0.796, \\ R_2(1) &= 0.888 \pm 0.065, & C\left(R_1(1),\ R_2(1)\right) &= -0.077. \end{aligned} \tag{1.38}$$

In order to test the lepton flavour universality with less theoretical uncertainty, we here introduce two observables, $\mathcal{R}_{D^{(*)}}$ defined as :

$$\mathcal{R}_{D^{(*)}} = \left[\int_{m_\tau^2}^{q^2_{max}} \frac{d\Gamma\left(\overline{B} \to D^{(*)}\tau\overline{\nu}\right)}{dq^2} dq^2\right] \times \left[\int_{m_\ell^2}^{q^2_{max}} \frac{d\Gamma\left(\overline{B} \to D^{(*)}\ell\overline{\nu}\right)}{dq^2} dq^2\right]^{-1}, \tag{1.39}$$

with $q^2_{max} = (m_B - m_{D^{(*)}})^2$, and $\ell = e$ or μ. Here m_B, $m_{D^{(*)}}$ and $m_\tau$are the mass of B, $D^{(*)}$ and τ respectively. The complete expressions for the q^2-distributions of the differential decay rates $d\Gamma/dq^2$ in $B \to D^{(*)}\tau\nu_\tau$ decays, obtained using the effective Hamiltonian in Eq.(1.19).

Along with these ratios, there are a number of other observables, that can be constructed in these channels, which are sensitive to NP. The definitions of these observables are given below.

- τ-polarization asymmetry is defined by :

$$P_\tau(D^{(*)}) = \frac{\Gamma^{(*)\lambda_\tau=1/2} - \Gamma^{(*)\lambda_\tau=-1/2}}{\Gamma^{(*)\lambda_\tau=1/2} + \Gamma^{(*)\lambda_\tau=-1/2}}\,, \tag{1.40}$$

where $\Gamma^{(*)\lambda_\tau=\pm\frac{1}{2}} = \int_{m_\tau^2}^{q^2_{max}} \frac{d\Gamma^{\lambda_\tau=\pm 1/2}(\bar{B}\to D^{(*)}\tau\bar{\nu})}{dq^2}$, λ_τ is the τ helicity, and $q^2_{max} = (m_B - m_{D^{(*)}})^2$.

- From the angular distribution in $D^* \to D\pi$ decays, D^* longitudinal polarization can be extracted as :

$$F_L^{D^*} = \frac{\Gamma^{\lambda_{D^*}=0}}{\Gamma^{\lambda_{D^*}=0} + \Gamma^{\lambda_{D^*}=1} + \Gamma^{\lambda_{D^*}=-1}}\,, \tag{1.41}$$

where $\Gamma^{\lambda_{D^*}=0,\pm1} = \int_{m_\tau^2}^{q^2_{max}} \frac{d\Gamma^{\lambda_{D^*}=0,\pm1}(\bar{B}\to D^*\tau\bar{\nu})}{dq^2}$.

- If we write the double-differential decay distribution as

$$\frac{d^2\Gamma\left(\overline{B}\to D^{(*)}\tau\overline{\nu}\right)}{dq^2 d\cos\theta} = a_\theta^{(*)}(q^2) + b_\theta^{(*)}(q^2)\cos\theta + c_\theta^{(*)}(q^2)\cos^2\theta\,, \tag{1.42}$$

where θ is the angle between the three-momenta of τ and $\bar{B}$ in the $\tau\bar{\nu}$ rest frame, then $b_\theta^{(*)}(q^2)$ determines the lepton forward-backward asymmetry in the following way:

$$\mathcal{A}_{\rm FB}^{(*)} = \frac{\int_0^1 \frac{d\Gamma^{(*)}}{d\cos\theta} d\cos\theta - \int_{-1}^0 \frac{d\Gamma^{(*)}}{d\cos\theta} d\cos\theta}{\int_{-1}^1 \frac{d\Gamma^{(*)}}{d\cos\theta} d\cos\theta} = \frac{\int b_\theta^{(*)}(q^2) dq^2}{\Gamma^{(*)}}\,, \tag{1.43}$$

The q^2 distributions for various τ and D^* polarization states together with $b_\theta^{(*)}(q^2)$ can be found in Appendix A.

In addition to these observables there are several other channels that will be affected by the same set of NP operators.

1.2.2.2 $B_c \to J/\psi\ \ell\ \nu_\ell$

Ratios similar to those defined in Eq. 1.39 can be defined for the decay channel $\bar{B}_c \to J/\psi \ell \bar{\nu}_\ell$ by replacing the respective meson as follows:

$$\mathcal{R}_{J/\psi} = \frac{\mathcal{B}\left(B_c \to J/\psi\tau\bar{\nu}_\tau\right)}{\mathcal{B}\left(B_c \to J/\psi\ell\bar{\nu}_\ell\right)}. \tag{1.44}$$

Here, $\mathcal{B}\left(B_c \to J/\psi\tau\bar{\nu}_\tau\right)$ denotes the branching fraction of $B_c \to J/\psi\tau\bar{\nu}_\tau$ decay. So far, we do not have lattice predictions for the form factors in the $B_c \to J/\psi$ decays. Therefore, for a precise calculation of form factors, we have to rely on different non-perturbative QCD approaches, for the detail see [77–83]. Choosing different parametrisations results in varying the central value of $\mathcal{R}_{J/\psi}$ within the range 0.25 to 0.29. Taking the uncertainties from different parametrisations into consideration, we see that the allowed theoretical range of $\mathcal{R}_{J/\psi}$ is actually larger than that. We consider two different parametrisations residing at two far ends of this range, namely perturbative QCD (PQCD [77]), and light-front covariant quark model (LFCQ [83]) in this work. A preliminary result on the form factor $A_1(q^2_{max})$ (this is the only form factor contributing to the decay at zero recoil) is available from the HPQCD collaboration [84].

1.2.2.3 $\Lambda_b \to \Lambda_c\ell\nu_\ell$

The q^2 distribution for the decay process $(\Lambda_b \to \Lambda_c\tau^-\nu_\tau)$ can be written as [85]

$$\frac{d\Gamma(\Lambda_b \to \Lambda_c\tau^-\nu_\tau)}{dq^2} = \frac{{G_F}^2|V_{cb}|^2q^2|\mathbf{p}_{\Lambda_c}|}{192\pi^3{M_1}^2}\left(1-\frac{{m_\tau}^2}{q^2}\right)^2 \times$$
$$\left[A_1^{VA} + \frac{{m_\tau}^2}{2q^2}A_2^{VA} + \frac{3}{2}A_3^{SP} + 2(1+\frac{2m_\tau^2}{q^2})A_4^T + \frac{3m_\tau}{\sqrt{q^2}}A_5^{VA-SP} + \frac{6m_\tau}{\sqrt{q^2}}A_6^{VA-T}\right] \tag{1.45}$$

where

$$
\begin{aligned}
A_1^{VA} &= |H^{VA}_{1/2,1}|^2 + |H^{VA}_{1/2,0}|^2 + |H^{VA}_{-1/2,0}|^2 + |H^{VA}_{-1/2,-1}|^2, \\
A_2^{VA} &= |H^{VA}_{1/2,1}|^2 + |H^{VA}_{1/2,0}|^2 + |H^{VA}_{-1/2,0}|^2 + |H^{VA}_{-1/2,-1}|^2 + 3|H^{VA}_{1/2,t}|^2 + 3|H^{VA}_{-1/2,t}|^2, \\
A_3^{SP} &= |H^{SP}_{1/2,0}|^2 + |H^{SP}_{-1/2,0}|^2, \\
A_4^{T} &= |H^{(T)1/2}_{1/2,t,0} + H^{(T)1/2}_{1/2,-1,1}|^2 + |H^{(T)1/2}_{-1/2,t,-1} + H^{(T)1/2}_{-1/2,-1,0}|^2 + |H^{(T)-1/2}_{1/2,0,1} + H^{(T)-1/2}_{1/2,t,1}|^2 \\
&\quad + |H^{(T)-1/2}_{-1/2,-1,1} + H^{(T)-1/2}_{-1/2,t,0}|^2, \\
A_5^{VA-SP} &= Re(H^{SP*}_{1/2,0}\, H^{VA}_{1/2,t} + H^{SP*}_{-1/2,0}\, H^{VA}_{-1/2,t}), \\
A_6^{VA-T} &= Re[H^{VA*}_{1/2,0}(H^{(T)1/2}_{1/2,-1,1} + H^{(T)1/2}_{1/2,t,0})] + Re[H^{VA*}_{1/2,1}(H^{(T)-1/2}_{1/2,0,1} + H^{(T)-1/2}_{1/2,t,1})] + \\
&\quad Re[H^{VA*}_{-1/2,0}(H^{(T)-1/2}_{-1/2,-1,1} + H^{(T)-1/2}_{-1/2,t,0})] + \\
&\quad Re[H^{VA*}_{-1/2,-1}(H^{(T)1/2}_{-1/2,-1,0} + H^{(T)1/2}_{-1/2,t,-1})].
\end{aligned}
\tag{1.46}
$$

where A_1^{VA} and A_2^{VA} represent the contributions from the vector and axial vector currents respectively. Their origin could be either the SM or any NP model. A_3^{SP} and A_4^{T} represent the contributions from the scalar-pseudoscalar and tensor currents, which will appear only in the NP models. A_5^{VA-SP} and A_6^{VA-T} are the interference terms which will have contributions from various operators in the SM, as well as an NP model. These are functions of combinations of the helicity amplitudes $H_{\lambda_{\Lambda_c},\lambda_w}$, which in turn can be expressed in terms of form factors and NP couplings. Explicit expressions of these helicity amplitudes are given in Appendix B. Several instances, where these form factors have been studied using sum rules and quark models, can be found in the literature [86–97]. For our purpose, helicity form factors have been calculated using the formula from lattice QCD in the relativistic heavy quark limit [98].

For the $\Lambda_b \to \Lambda_c \ell \nu_\ell$, motivated by the lepton flavor university violation, two observables can be defined here as:

$$\mathcal{R}_{\Lambda}^{\mu} = \frac{\mathcal{B}\left(\Lambda_b \to \Lambda_c \tau \bar{\nu}_\tau\right)}{\mathcal{B}\left(\Lambda_b \to \Lambda_c \mu \bar{\nu}_\mu\right)} \tag{1.47}$$

$$\mathcal{R}_{\Lambda}^{e} = \frac{\mathcal{B}\left(\Lambda_b \to \Lambda_c \tau \bar{\nu}_\tau\right)}{\mathcal{B}\left(\Lambda_b \to \Lambda_c e \bar{\nu}_e\right)} \tag{1.48}$$

Along with these ratios, we have also considered the forward-backward asymmetry in $\Lambda_b \to \Lambda_c \tau^- \nu_\tau$, defined as

$$\begin{aligned} \mathcal{A}_{FB}(q^2) \;\; &= \;\; \left(\frac{d\Gamma}{dq^2}\right)^{-1} \frac{G_F^2 V_{cb}^2}{512\pi^3} \frac{q^2\sqrt{Q_+Q_-}}{m_{\Lambda_b}^3} \left(1 - \frac{m_\tau^2}{q^2}\right)^2 \Bigg[B_1^{VA} + \frac{2m_\tau^2}{q^2} B_2^{VA} + \frac{4m_\tau^2}{q^2} B_3^{T} + \\ &\quad \frac{2m_\tau}{\sqrt{q^2}} B_4^{VA-SP} + \frac{4m_\tau}{\sqrt{q^2}} B_5^{VA-T} + 4B_6^{SP-T} \Bigg], \end{aligned} \tag{1.49}$$

where $Q_\pm = (m_{\Lambda_b} \pm m_{\Lambda_c})^2 - q^2$ and

$$\begin{aligned} B_1^{VA} &= |H_{1/2,1}^{VA}|^2 - |H_{-1/2,-1}^{VA}|^2, \\ B_2^{VA} &= Re[H_{1/2,t}^{VA*} H_{1/2,0}^{VA} + H_{-1/2,t}^{VA*} H_{-1/2,0}^{VA}], \\ B_3^{T} &= |H_{1/2,0,1}^{(T)-1/2} + H_{1/2,t,1}^{(T)-1/2}|^2 - |H_{-1/2,-1,0}^{(T)1/2} + H_{-1/2,t,-1}^{(T)1/2}|^2, \\ B_4^{VA-SP} &= Re[H_{1/2,0}^{SP*} H_{1/2,0}^{VA} + H_{-1/2,0}^{SP*} H_{-1/2,0}^{VA}], \\ B_5^{VA-T} &= Re[H_{1/2,t}^{VA*}(H_{1/2,-1,1}^{(T)1/2} + H_{1/2,t,0}^{(T)1/2})] + Re[H_{1/2,1}^{VA*}(H_{1/2,0,1}^{(T)-1/2} + H_{1/2,t,1}^{(T)-1/2})] \\ &\quad + Re[H_{-1/2,t}^{VA*}(H_{-1/2,-1,1}^{(T)-1/2} + H_{-1/2,t,0}^{(T)-1/2})] - Re[H_{-1/2,-1}^{VA*}(H_{-1/2,-1,0}^{(T)1/2} + H_{-1/2,t,-1}^{(T)1/2})], \\ B_6^{SP-T} &= Re[H_{1/2,0}^{SP*}(H_{1/2,-1,1}^{(T)1/2} + H_{1/2,t,0}^{(T)1/2})] + Re[H_{-1/2,0}^{SP*}(H_{-1/2,-1,1}^{(T)-1/2} + H_{-1/2,t,0}^{(T)-1/2})]. \end{aligned} \tag{1.50}$$

There is no contribution from pure (pseudo-)scalar operators to the forward-backward asymmetry, but all possible interference terms are present.

1.2.2.4 $B \to X_c \tau \bar{\nu}_\tau$

Similar to the ratios $\mathcal{R}_{D^{(*)}}$, we can define the following ratio for the inclusive decay $B \to X_c \tau \nu_\tau$:

$$\mathcal{R}_{X_c} = \frac{\mathcal{B}\left(B \to X_c \tau \bar{\nu}_\tau\right)}{\mathcal{B}\left(B \to X_c \ell \bar{\nu}_\ell\right)}, \tag{1.51}$$

with $\ell = \mu, e$. For $B \to X_c \ell \nu_\ell$ decay, the expansion of total decay width is given by [99]

$$\begin{aligned} \Gamma_{sl} \;\; &= \;\; \Gamma_0 \Bigg[1 + a^{(1)} \frac{\alpha_s(m_b)}{\pi} + a^{(2,\beta_0)} \beta_0 \left(\frac{\alpha_s}{\pi}\right)^2 + a^{(2)} \left(\frac{\alpha_s}{\pi}\right)^2 \\ &\quad + \left(-\frac{1}{2} + p^{(1)} \frac{\alpha_s}{\pi}\right) \frac{\mu_\pi^2}{m_b^2} + \left(g^{(0)} + g^{(1)} \frac{\alpha_s}{\pi}\right) \frac{\mu_G^2(m_b)}{m_b^2} \\ &\quad + d^{(0)} \frac{\rho_D^3}{m_b^3} - g^{(0)} \frac{\rho_{LS}^3}{m_b^3} + \text{higher orders} \Bigg], \end{aligned} \tag{1.52}$$

where $\Gamma_0 = A_{ew} |V_{cb}^2| G_F^2 m_b^5 (1 - 8\rho + 8\rho^3 - \rho^4 - 12\rho^2 \ln \rho)/192\pi^3$ is the tree level free quark decay width, $\rho = m_c^2/m_b^2$, and $A_{ew} = 1.014$ the leading electroweak correction. The parameters $\mu_\pi^2, \mu_g^2, \rho_D^3, \rho_{ls}^3$ are the B meson expectation values of the relevant dimension 5 and 6 local operators. The coefficients $a^{(i)}, g^{(i)}, p^{(1)}, d^{(0)}$ are functions of ρ and of various unphysical scales, such as the one of α_s. The complete one and two-loop perturbative corrections [100–105], along with the $1/m_b^{2,3}$ power corrections [106–109] have been included in Eq. (1.52).

The simplified expression for the decay width of the inclusive semitaunic decay of B meson in SM are given in [110]:

$$\begin{aligned} &\Gamma^{SM}(\bar{B} \to X_c \tau \bar{\nu}) = \\ &\Gamma_0 \left[C_0^{(0)} + \frac{\alpha_s}{\pi} C_0^{(1)} + \left(\frac{\alpha_s}{\pi}\right)^2 C_0^{(2)} + C_{\mu_\pi^2} \frac{\mu_\pi^2}{m_b^2} + C_{\mu_G^2} \frac{\mu_G^2}{m_b^2} + C_{\rho_D^3} \frac{\rho_D^3}{m_b^3} + C_{\rho_{LS}^3} \frac{\rho_{LS}^3}{m_b^3} \right] \end{aligned} \tag{1.53}$$

where

$$\Gamma_0 = \frac{G_F^2 |V_{cb}|^2 \, m_b^5 A_{ew}}{192\pi^3}.$$

Here, the terms involving $C_0^{(0)}$, $C_0^{(1)}$, and $C_0^{(2)}$ represent the contributions from the leading order(LO), next-to-leading order (NLO) [111], and next-to-next-to-leading order (NNLO) [104] corrections in α_s respectively, whereas $C_{\mu_\pi^2}$, $C_{\mu_G^2}$, and $C_{\rho_D^3}$, $C_{\rho_{LS}^3}$ are the contributions at order $1/{m_b}^2$ [112] and $1/{m_b}^3$ [110], respectively. These coefficients depend on the quark and lepton masses.

To calculate the effects of new physics in the inclusive decay $B \to X_c \tau \bar{\nu}_\tau$, we decompose the decay width as

$$\Gamma(\bar{B} \to X_c \tau \bar{\nu}) = \Gamma^{SM} + \Gamma^{NP}_{(1)} + \Gamma^{NP}_{(2)} \,. \tag{1.54}$$

Here, the first piece is arising solely from SM, while the second and third terms are the contributions from NP with different powers of the new couplings. The expressions of $\Gamma^{NP}_{(1)}$ and $\Gamma^{NP}_{(2)}$ are given in Appendix B [113]. Some other recent works, discussing NP effects in the inclusive mode, are given in ref.s [114, 115].

1.2.2.5 $B_c \to \tau \nu_\tau$

In terms of the general hamiltonian defined in Eq. 1.19, the branching fraction of $B_c \to \tau \nu_\tau$ can be expressed as [116, 117],

$$\begin{aligned}&\mathcal{B}(B_c \to \tau \nu_\tau) = \\ &\tau_{B_c} \frac{m_{B_c} m_\tau^2 f_{B_c}^2 G_F^2 \left|V_{cb}\right|}{8\pi} \left(1 - \frac{m_\tau^2}{m_{B_c}^2}\right)^2 \left|1 + (C_{V_1} - C_{V_2}) + \frac{m_{B_c}^2}{m_\tau (m_b + m_c)} (C_{S_1} - C_{S_2})\right|^2 ,\end{aligned} \tag{1.55}$$

where $f_{B_c} = 0.434(15)$GeV and $\tau_{B_c} = 0.507(9)$ps are the B_c decay constant and lifetime, respectively.

Barring $\mathcal{R}_{D^{(*)}}$, $P_\tau(D^*)$ and $\mathcal{R}_{J/\Psi}$, the other observables which are mentioned above are not yet measured experimentally. The present experimental status of all the measured observables in $b \to c \tau \nu_\tau$ decays are presented in the next section.

1.3 Experimental status

All the experimental results used in this thesis is tabulated in table 1.4. There have been quite a few measurements of the ratios $\mathcal{R}_{D^{(*)}}$ in recent years. Current experimental status of $\mathcal{R}_{D^{(*)}}$ is given in fig. 1.3. Apart from the most recent ones measuring $\mathcal{R}_{D^*}$, they are

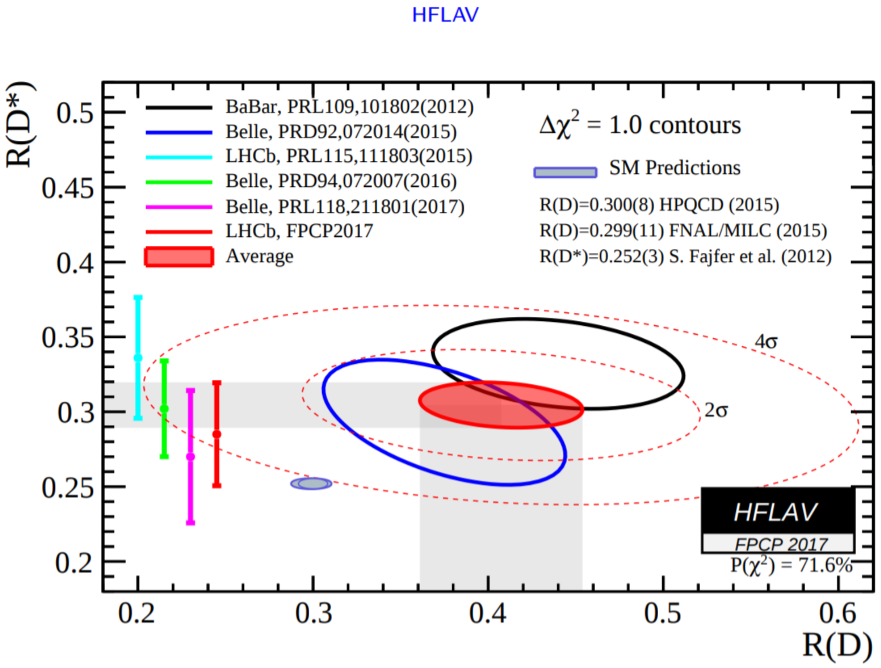

Fig. 1.3 Current Experimental Status of $\mathcal{R}(D^*)$ by HFLAV.

	$\mathcal{R}_D$	$\mathcal{R}_{D^*}$	$\rightarrow$ Correlation	$P_\tau(D^*)$	$\mathcal{R}_{J/\Psi}$
BABAR [118]	0.440(58)(42)	0.332(24)(18)	−0.27	-	-
Belle (2015) [119]	0.375(64)(26)	0.293(38)(15)	−0.49	-	-
Belle (2016) [120]	-	0.302(30)(11)	-	-	-
Belle (2016) [121]	-	$0.270(35)(^{+0.028}_{-0.025})$	0.33	$-0.38(51)(^{+0.21}_{-0.16})$	-
LHCb (2015) [122]	-	0.336(27)(30)	-	-	-
LHCb (2017) [123]	-	0.286(19)(25)(21)	-	-	-
LHCb (2017) [124]	-	-	-	-	0.71(17)(18)

TABLE 1.4: Present experimental status of the observables used in this analysis. First uncertainty is statistical and the second one is systematic.

consistent with a sizable deviation from the SM. The experimental result most deviated from the SM predictions is still the first one reported by *BABAR*. Though it is apparent from the recent measurements that $\mathcal{R}_{D^*}$ values are coming down towards the SM, it is still too early to consider it as a trend because The actual deviation depends heavily on the correlation between $\mathcal{R}_D$ & $\mathcal{R}_{D^*}$, and any analysis bears the risk of being inconclusive without the simultaneous measurement of both of them. As an example, one can check the Belle (2015) result [119], where the $\mathcal{R}_{D^*}$ is consistent with the SM result within 1σ, but the combined result is at tension with the SM due to $\mathcal{R}_D$ and its correlation with $\mathcal{R}_{D^*}$.

The first, although quite imprecise, measurement of τ polarization asymmetry is done by Belle in 2015 [119]. Table 1.4 also contains the recent measurement of $\mathcal{R}_{J/\psi}$ by LHCb [124]. Not only is this result in tension with the theoretical predictions, the central measured-value is almost double of that predicted by SM. As the experimental uncertainty is large, they are still consistent with 90% C.L. range. LHCb has used a z-expansion parametrization [125] for the shared form factors for the signal and normalization modes and has determined them directly from the data. The decay $B_c \to \tau\nu$, despite being out of the experimental reach for now [126], can be used as an effective constraint on any NP effects that could potentially explain the $\mathcal{R}_{D^{(*)}}$ and $\mathcal{R}_{J/\psi}$ excesses. A conservative upper limit quoted for $\mathcal{B}(B_c \to \tau\nu)$, even after adding NP effects, is $\lesssim 30\%$ [117]. A stronger upper bound of $\lesssim 10\%$ is obtained from LEP data taken at Z-peak [127] with a prospect of an even tighter bound from the full L3 data [128].

From the discussion presented in the previous section, it is now clear to us that there are several strong evidences and hints which motivates us to consider BSM scenarios in $b \to c\tau\nu_\tau$ decays to explain observed deviations of the SM predictions of several observables from their experimental outcomes. In the proceeding chapters we present our attempts to explore such possibilities one by one, as Enrico Fermi once said, "It is no good to try to stop knowledge from going forward. Ignorance never is better than knowledge".

Chapter 2

Methodology

2.1 Introduction

In this chapter, we present a brief overview of statistical methods used in our study. Theoretical physics is validated by active experimentation; that is, observation and measurement. Over the last decade, flavour physics has entered into the precision era which demands a very clear knowledge of the experimental uncertainties (both statistical and systematic) and thus confidence intervals for the measurements of different observables. Our constant endeavor is to go even further to achieve more and more accuracy in future experiments. But with the increasing cost of these experiments it has become important to extract as much of the information as possible from the hard-won data, and to quantify as accurately as possible the inferences one draws when confronting the data with model predictions.

As discussed in the previous chapter, there are several low energy observables which can be measured with very good accuracy in different experiments. The interesting scenarios are the ones where the SM predictions for one or more observables significantly deviate from their respective measured values. If we understand very well the SM calculations along with their respective errors, then we can suspect that the observed discrepancies are due to some BSM physics. There could be various NP explanations of an observed excess, although it is not necessary for an observable to show equal sensitivity to all the different types of NP. In these contexts the questions that inevitably arise are following :

- How an observable can be optimised to get maximal sensitivity to a specific NP coupling ?
- Which type of new physics can best explain present experimental data ?

In search of the answer of first one, we have used Optimal Observable technique. With this technique one can systematically estimate the statistical uncertainty of the measurable parameters while extracting them from some observable. This in turn will help us to check the sensitivity of that observable to a particular type of NP structure.

To address the second question, we have used information theoretic approach, more specifically Akaike Information Criteria to obtain a data-based selection of a best NP scenario and ranking and weighting of the remaining models. In the rest of this chapter, we will provide a detailed discussion on the methodology of these two analysis.

2.2 Optimal Observable Technique

In this section we give a resume of the definition and properties of optimal observables method. Elaborate discussions on this technique can be found in references [129–132]. Following the notation of Ref. [130, 131], let us consider an observable $O(\phi)$ defined as,

$$O(\phi) = \sum_i c_i f_i(\phi)\,. \tag{2.1}$$

Here c_is are model-dependent coefficients, and $f_i(\phi)$s are known functions of ϕ. It is very important to know how sensitive the observable is to a given set of c_is, independent of the method that will be used in the future analysis of the data. These c_is can be extracted by using convenient weighting functions $w_i(\phi)$ such that $\int w_i(\phi)O(\phi)\,d\phi = c_i$. In general different choices of $w_i(\phi)$ are possible. However there is a unique choice for which the statistical error in determining c_i is minimised so that

$$\int w_i(\phi)f_j(\phi)d\phi = \delta_{ij} \tag{2.2}$$

Hence,

$$\int \delta w_i(\phi)f_j(\phi)d\phi = 0 \tag{2.3}$$

and thus, the infinitesimal change in the covariance volume V_{ij} is zero; i.e.

$$\delta V_{ij} \sim \int \delta[w_i(\phi)w_j(\phi)]O(\phi)d\phi = 0 \tag{2.4}$$

The weighting function that satisfies above relation can be written as

$$w_i(\phi) = \frac{\sum_j X_{ij} f_j(\phi)}{O(\phi)} \tag{2.5}$$

where $X_{ij} = M_{ij}^{-1}$ and

$$M_{ij}(\phi) = \int \frac{f_i(\phi)f_j(\phi)}{O(\phi)}d\phi \tag{2.6}$$

We can accordingly compute the corresponding coefficients c_i by

$$c_i = \sum_k X_{ik} I_k = \sum_k M_{ik}^{-1} I_k \tag{2.7}$$

where I_k is defined through

$$I_k = \int f_k(\phi)d\phi \tag{2.8}$$

For only this choice of weighting functions, the covariance matrix is

$$V_{ij} \equiv= \langle \Delta c_i \Delta c_j \rangle = \frac{M_{ij}^{-1}\sigma_T}{N} \tag{2.9}$$

where $\sigma_T = \int O(\phi)d\phi$ is the integrated observable and $N = L_{eff}\sigma_T$ is the total number of events, with L_{eff} being the luminosity times efficiency. This result remains unchanged even if there are applied cuts. The minimum of statistical uncertainties in the extraction of parameters gives the maximum significance of that parameter over the others. Thus, with this technique we can check the significance of a specific NP model over the other models, including the SM. In other words, given the data, one can say with what significance some observable may differentiate a particular type of NP from the SM. This significance, as one should point out here, depends on the observable chosen, on the parameters of the NP model, and on the integrated luminosity, all of which are intuitively obvious.

2.3 χ^2 Analysis

In high energy physics, one of the most popular methods for error estimation and model assessment is Reduced χ^2-squared analysis. To fit the parameters of the theory we need to perform a test of significance (goodness of fit) by defining a χ^2 statistic, a function of the parameters parameterizing the theory. In this section, we try to brief the basics of this method of parameter estimation.

Consider a set of N independent measurements y_i at known points x_i. Here we consider that the measurement y_i is Gaussian with mean $\mu(x_i;\theta)$ and variance σ_i^2. To construct the estimators for the unknown fit parameters θ, the log-likelihood function contains the sum of the squares

$$\chi^2(\boldsymbol{\theta}) = -2lnL(\boldsymbol{\theta}) + constant = \sum_i^N \frac{(y_i - \mu(x_i;\boldsymbol{\theta}))^2}{\sigma_i^2} \tag{2.10}$$

The value of the parameters $\hat{\boldsymbol{\theta}}$ which maximize L (maximum likelihood (ML) estimators) are the same as those which minimize χ^2.

If the y_is are not independent but have a covariance matrix $V_{ij} = cov[y_i, y_j]$, then we have to redefine the χ^2 as

$$\chi^2(\boldsymbol{\theta}) = (\boldsymbol{y} - \boldsymbol{\mu}(\boldsymbol{\theta}))^T V^{-1}(\boldsymbol{y} - \boldsymbol{\mu}(\boldsymbol{\theta})), \tag{2.11}$$

where $\boldsymbol{y} = (y_1, ..., y_N)$ is the (column) vector of measurements, $\boldsymbol{\mu}(\boldsymbol{\theta})$ is the corresponding vector of predicted values.

Expanding $\chi^2(\boldsymbol{\theta})$ about $\hat{\boldsymbol{\theta}}$, we find the contour in parameter space defined by

$$\chi^2(\boldsymbol{\theta}) = \chi^2(\hat{\boldsymbol{\theta}}) + 1 = \chi^2_{min} + 1 \tag{2.12}$$

has tangent planes located at approximately plus or minus one standard deviation $\sigma_{\hat{\theta}}$ from the $\hat{\boldsymbol{\theta}}$.

As the minimum value of the χ^2 gives some idea about the level of agreement between the measurements and the fitted function, it can be used for assessing the goodness-of-fit.

2.4 Goodness-of-Fit

To quantify the level of agreement between the data and a hypothesis without explicit reference to alternative hypothesis, we define the p-value, corresponding to the χ^2_{min} and the degrees of freedom (DoF) for that fit. Assuming the goodness-of-fit statistic follows a χ^2 probability distribution function (p.d.f.), the p- value for the hypothesis is then

$$p = \int_{\chi^2}^{\infty} f(z; n_d) dz \tag{2.13}$$

where $f(z; n_d)$ is the χ^2 p.d.f. and n_d is the appropriate number of degrees of freedom. In general, the mean of the χ^2 distribution is equal to n_d. Hence the quantity χ^2/n_d, reduced χ^2 (χ^2_{red}) is reported in the literature. This is essentially used for the following purposes :

- Single-model assessment : If a model fitted to data and the resulting χ^2_{red} is greater than one, it is treated as a “bad” fit.
- Convergence diagnostic : As the fit procedure is iterative, the convergence is necessary. One can estimate this convergence by monitoring the values of χ^2_{red} evolves during the iteration. This iterative algorithm should be stopped as soon as χ^2_{red} attains a value adequately close to one.
- Model comparison : Considering a data with a set of different models, qualitatively we try to estimate which model fits the data best. Generally, each model is fit to the data and their χ^2_{red} values are compared. The leading model is that one whose value of χ^2_{red} is closest to one.

In all these scenarios, χ^2_{red} excels in simplicity, since the only thing we need to do is divide the value of χ^2_{min} by degrees of freedom and compare the value of χ^2_{red} to one.

Keeping in mind all these advantages of χ^2_{red}, we need to consider carefully the pitfalls that may severely limit the credibility of these applications. One of the major problems that typically arise in using χ^2_{red} in practice, stems from the fact that the χ^2 value is subject to the random noise present in the data. For a given set of data, we can always compute the value of χ^2. However, if we consider a second set of data , drawn from the same physical process such that only noise realization is different, the value of χ^2 will different from the first set. Consequently, there is an "uncertainty" on the value of χ^2_{red}. This uncertainty is typically ignored in practice.

Thus from the above discussion, we can realize that the value of χ^2_{red} is not sufficient information to assess the convergence or compare different models. The obligatory step to assess the goodness-of-fit of an analysis after optimization is then to inspect the distribution of the residuals. For the true model, with a priori known measurement errors, the distribution of normalized residual

$$R_i = \frac{(y_i - \mu(x_i; \boldsymbol{\theta}))}{\sigma_i} \tag{2.14}$$

is by definition a Gaussian with mean $\mu = 0$ and variance $\sigma^2 = 1$ [133]. This fact is utilized to test the significance of the fit by plotting the distribution of normalized residuals in a histogram and compare it to a Gaussian of $\mu = 0$ and $\sigma^2 = 1$. If the histogram shows a significant deviation from the Gaussian, we can rule out that model. If there is no significant difference, we can conclude that either this is a compatible model with the data or the number of data points are not enough to discover the deviation. The comparison of the residuals to this Gaussian can be objectively quantified by Shapiro-Wilks (S-W) test [134] for normality. The reasons for choosing S-W over other competing tests for normality are following: *a*) Though we have used the algorithm *AS R*94 by Royston [135], which was developed for any sample size (n) $3-5000$, the original S-W test was specifically designed for $n < 50$. *b*) This is the first test which detected departures from normality using skewness and/or kurtosis and since then have been regularly corrected and developed. *c*) It has repeatedly been shown [136] that from low to medium sample sizes, where degenerate values occur less, S-W is the 'most powerful' parametric test for normality among other popular contenders like 'Kolmogorov-Smirnov', 'Anderson-Darling', 'Cramér-von Mises', 'Jarque-Bera' etc. In all such tests, the validity of a hypothesis depends on whether the probability of the goodness of fit test is above or below the significance, which in our case is set at 5%. Across all the fitted models, the ones with the p-value of the residual-distribution above 5% will be considered to fit the data well; all of the rest can be thrown out. Therefore, if a particular model fitting analysis passes our normality test, we consider that model as the plausible explanation of the data.

2.5 Model Selection

One of the main motivations of this thesis is to do a multi-scenario analysis on the experimentally available binned data, to obtain a data-based selection of a best case and ranking and weighting of the remaining cases. For this purpose, different models can be compared with regard to their model fit by computing a $\Delta\chi^2$ test. This test allows to decide whether a given model fits significantly better or worse than a competing model.

2.5.1 $\Delta\chi^2$ test

A $\Delta\chi^2$ test is useful when the competing models are nested. Two models are considered "nested" if one is a subset or extension of the other, i.e. one of the models could be obtained by fixing or eliminating parameters in the other model. When the model with the fewer free parameters (null, in many cases) is true, and when certain conditions are satisfied, Wilks' Theorem [137] says that this difference ($\Delta\chi^2$) should have a χ^2 distribution with the number of degrees of freedom equal to the difference in the number of free parameters in the two models. This lets one compute a p-value and then compare it to a critical value to decide whether to reject the null model in favor of the alternative model.

Considering the simplicity of this technique, we need to remember that unlike the Akaike information criterion (AIC_c) or the Schwarz-Bayesian Criterion (BIC) [138], which incorporate the concept of parsimony and can be applied to nested as well as non-nested models,$\Delta\chi^2$ test, can only be applied to nested models.

One of the most powerful and reliable methods for model comparison is cross validation. The most straightforward (and also most expensive) flavor of cross validation is leave-one-out cross validation (LOOCV). It simultaneously tests the predictive power of the model as well as minimizes the bias and variance together. In LOOCV, one of the data points is left out and the rest of the sample (training set) is optimized. Then that result is used to find the predicted residual for the left-out data point. This process is repeated for all data points and a mean-squared error (MSE) is obtained. For model selection, this MSE is minimized. Unfortunately, it is computationally very expensive. Hence we have to find out some other reasonable method for model selection.

For that goal, we have made use of information-theoretic approaches, especially of the second order Akaike information criterion (AIC_c) in the analysis of empirical data. It has been shown that LOOCV is asymptotically equivalent to minimizing AIC [139]

2.5.2 Introduction to AIC$_c$

The 'concept of parsimony' [140] dictates that a model representing the truth should be obtained with "... the smallest possible number of parameters for adequate representation of the data." In general, bias decreases and variance increases as the dimension of the model increases. Often, the number of parameters in a model is used as a measure of the degree of structure inferred from the data. The fit of any model can be improved by increasing the number of parameters. Parsimonious models achieve a proper trade-off between bias and variance. All model selection methods are based to some extent on the principle of parsimony [141].

In information theory, the Kullback-Leibler (K-L) Information or measure $I(f, g)$ denotes the information lost when g is used to approximate f. Here f is a notation for full reality or truth and g denotes an approximating model in terms of probability distribution. $I(f, g)$ can also be defined between the 'best' approximating model and a competing one. Akaike, in his seminal paper [142] proposed the use of the K-L information as a fundamental basis for model selection. However, K-L distance cannot be computed without full knowledge of both f (full reality) and the parameters (Θ) in each of the candidate models $g_i(x|\Theta)$ (a model g_i with parameter-set Θ explaining data x). Akaike found a rigorous way to estimate K-L information, based on the empirical log-likelihood function at its maximum point.

'Akaike's information criterion'(AIC) with respect to our analysis can be defined as,

$$\mathrm{AIC} = \chi^2_{min} + 2K \tag{2.15}$$

where K is the number of estimable parameters. In application, one computes AIC for each of the candidate models and selects the model with the smallest value of AIC. It is this model that is estimated to be "closest" to the unknown reality that generated the data, from among the candidate models considered.

While Akaike derived an estimator of K-L information, AIC may perform poorly if there are too many parameters in relation to the size of the sample. Sugiura [143] derived a second-order variant of AIC,

$$\mathrm{AIC}_c = \chi^2_{min} + 2K + \frac{2K(K+1)}{n-K-1} \tag{2.16}$$

where n is the sample size. As a rule of thumb, Use of AIC$_c$ is preferred in literature when $n/K < 40$. There are various other such information criteria defined later on, e.g. QAIC, QAIC$_c$, TIC etc. In this analysis, we consistently use AIC$_c$.

Whereas AIC$_c$ are all on a relative (or interval) scale and are strongly dependent on sample size, simple differences of AIC$_c$ values ($\Delta_i^{AIC} = \mathrm{AIC}_c^i - \mathrm{AIC}_c^{min}$) allow estimates of the relative expected K-L differences between f and $g_i(x|\Theta)$. This allows a quick comparison and ranking of candidate models. The model estimated to be best has $\Delta_i^{AIC} \equiv \Delta_{min}^{AIC} = 0$. The larger Δ_i^{AIC} is, the less plausible it is that the fitted model $g_i(x|\Theta)$ is the K-L best model, given the data x. Table 2.1 lists rough rule-of-thumb values of Δ_i^{AIC} for analysis of nested models.

Δ_i^{AIC}	Level of Empirical Support for Model i
$0-2$	Substantial
$4-7$	Considerably Less
>10	Essentially None

Table 2.1: Rough rule-of-thumb values of Δ_i^{AIC} for analysis of nested models.

While the Δ_i^{AIC} are useful in ranking the models, it is possible to quantify the plausibility of each model as being the actual K-L best model. This can be done by extending the concept of the likelihood of the parameters given both the data and model, i.e. $\mathcal{L}(\Theta|x, g_i)$, to the concept of the likelihood of the model given the data, hence $\mathcal{L}(g_i|x)$;

$$\mathcal{L}(g_i|x) \propto e^{(-\Delta_i^{AIC}/2)}\,. \tag{2.17}$$

Such likelihoods represent the relative strength of evidence for each model [144].

To better interpret the relative likelihood of a model, given the data and the set of R models, we normalize the $\mathcal{L}(g_i|x)$ to be a set of positive Akaike weights, w_i , adding up to 1:

$$w_i = \frac{e^{(-\Delta_i^{AIC}/2)}}{\sum_{r=1}^{R} e^{(-\Delta_r^{AIC}/2)}} \tag{2.18}$$

A given w_i is considered as the weight of evidence in favor of model i being the actual K-L best model for the situation at hand, given that one of the R models must be the K-L best model of that set. The w_i depend on the entire set; therefore, if a model is added or dropped during a post hoc analysis, the w_i must be recomputed for all the models in the newly defined set.

Chapter 3

Test of new physics sensitivity of the observables in $B \to D^{(*)}\tau\nu_\tau$ decay using Optimal-observable technique

3.1 Introduction

In this chapter, we have discussed the new physics sensitivities of the various observables in $B \to D^{(*)}\tau\nu_\tau$ decays. In particular, we have chosen the operator basis defined in Eq. (1.20) in chapter 1 which includes the new vector, scalar and tensor type of interactions. To achieve this goal, we use the Optimal Observable technique. This technique, discussed in section 2.2, has been widely used in collider phenomenology [129–132, 145, 146]. But for the first time in our study, we are using this in heavy flavour physics. In the absence of any data, this type of analysis are very useful and provide information about the sensitivity of an observable to a particular type of NP operator in a future experiment. Also, this technique helps one to identify the observables where the NP can be differentiated from the SM with highest confidence level [147, 148].

From the discussion in section 1.3, we observed that the discrepancy among the SM predicted values of different observables with there experimental results in these decay indicate a possible signature of NP in $B \to D^{(*)}\tau\nu_\tau$ transitions. There are several model dependent NP analysis of this observation, as for example see [67, 149, 150], at the same time there are couple of model-independent analysis [66, 151, 152]. In a model dependent analysis, the characteristics of the models could be very different in terms of the types of new interactios. It is possible that in all these analysis, multiple NP interactions may contribute together. Hence, it will be an impossible task to extract all the couplings from a single measurement. If one can reduce the number of coupling parameters by imposing certain constraints on the full set of parameters, only then it is possible to extract meaningful errors on the couplings, although the information lost due to various assumptions cannot be retrieved. Therefore, it will be useful to have independent couplings, parametrised in such a way that the measured errors on different parameters are uncorrelated. On the other hand, a particular observable is not equally sensitive to different types of NP operators. Hence from a phenomenological point of view, with the optimal observable analysis, we try to find out how an observable can be optimised to guarantee the maximal sensitivity to a particular type of NP interaction. This in turn will help us to select observables that are suitable for the extraction of a particular type of NP coupling.

In section 3.2 we first discuss the formalism of the optimal observable technique in the context of several observables in $B \to D^{(*)}\tau\nu_\tau$ decay channels. A numerical analysis is presented in section 3.3 that tests the new physics sensitivity of each of the integrated observables considered in this study. In the next part of section 3.3, we have performed the bin-by-bin analysis of q^2 distribution of the differential branching fraction for $B \to D^{(*)}\tau\nu_\tau$ decays to zoom in the regions of q^2 where a particular type of NP interaction shows maximal sensitivity to the considered observable. In section 3.4 we summarize the significant results obtained in this chapter.

3.2 Formalism

The optimal-observable analysis is a technique to methodically evaluate the statistical uncertainties of the measurable parameters while extracting them from some observable. The methodology of this analysis is given in section 2.2. In order to apply this technique to $B \to D^{(*)}\tau\nu_\tau$, it is necessary to express the q^2 distribution of the differential decay rate as

$$\frac{d\Gamma(B \to D^{(*)}\tau\nu_\tau)}{dq^2} = \sum_i C_i f_i(q^2), \tag{3.1}$$

where C_is are functions of the wilson coefficient C_Ws. The theoretical expressions for C_is, along with the $f_i(q^2)$s, can be extracted from a direct comparison between the similar terms on right sides of Eq.(3.1) and Eq.(1.21) (for $B \to D$ channel) or eq. (1.22) (for $B \to D^*$ channel). The coefficients C_i, relevant for the branching fractions in $B \to D^{(*)}\tau\nu_\tau$, are given in Table 3.1, and the corresponding $f_i(q^2)$s are given in the Appendix (Table C.1).

Obs C_i	$d\Gamma/dq^2$ in $B \to D\tau\nu_\tau$	$d\Gamma/dq^2$ in $B \to D^*\tau\nu_\tau$
C_1	$\|1 + C_{V_1} + C_{V_2}\|^2$	$\|1 + C_{V_1}\|^2 + \|C_{V_2}\|^2$
C_2	$\|C_{S_1} + C_{S_2}\|^2$	$Re[(1 + C_{V_1})C^*_{V_2}]$
C_3	$\|C_T\|^2$	$\|C_{S_1} - C_{S_2}\|^2$
C_4	$Re[(1 + C_{V_1} + C_{V_2})(C^*_{S_1} + C^*_{S_2})]$	$\|C_T\|^2$
C_5	$Re[(1 + C_{V_1} + C_{V_2})C^*_T]$	$Re[(1 + C_{V_1} - C_{V_2})(C^*_{S_1} - C^*_{S_2})]$
C_6	–	$Re[(1 + C_{V_1})C^*_T]$
C_7	–	$Re[C_{V_2}C^*_T]$

TABLE 3.1: C_is as defined in eq.(3.1). The observable $P^R_\tau(q^2)$ contains the same set of C_is.

The goal of this technique is to extract C_is, which can be done by defining suitable weighting functions $w_i(q^2)$ such as $C_i = \int w_i(q^2)(d\Gamma/dq^2)dq^2$. In general various choices of w_is are possible. However, there is a unique choice for which the resulting error in the extraction of C_i is minimized [1], and these functions are given by

$$w_i(q^2) = \sum_j \frac{X_{ij} f_j(q^2)}{d\Gamma/dq^2}, \tag{3.2}$$

where X_{ij} is the inverse of M_{ij} which is defined as

$$M_{ij} = \int dq^2 \frac{f_i(q^2) f_j(q^2)}{f_{SM}(q^2)}. \tag{3.3}$$

---

[1] C_is are minimised in a sense that the whole covariance matrix is at a stationary point in terms of varying the functional forms of $w_i(q^2)$ while maintaining $\int w_i(q^2) f_k(q^2) = \delta_{ik}$.

In the above expression, $f_{SM}(q^2)$ can be obtained from eq.(3.1) by setting $C_W = 0$, while $C_{SM} = 1$. Hence, using eqs. (3.2), and (3.3) the statistical uncertainties in C_i extracted from the branching fractions can be obtained as [130, 131]

$$|\delta C_i| = \sqrt{\frac{X_{ii}\mathcal{B}(B \to D^{(*)}\tau\nu_\tau)^{exp}}{N_{sig}}} = \sqrt{\frac{X_{ii}}{\sigma_P \mathcal{L}_{eff}}}, \tag{3.4}$$

where $\mathcal{B}^{exp} = (1/\Gamma)\int dq^2 d\Gamma/dq^2$ is the total branching fraction in the decay $B \to D^{(*)}\tau\nu_\tau$ with Γ as the total decay width. N_{sig} is the total number of events. As given in eq.(3.4), the errors are also related to the production cross section σ_P ($= \sigma_{B\to D^{(*)}\tau\nu_\tau}/\mathcal{B}(B \to D^{(*)}\tau\nu_\tau)$), and the effective luminosity $\mathcal{L}_{eff} = \mathcal{L}_{int}\epsilon_s$, where $\mathcal{L}_{int}$ and ϵ_s are the integrated luminosity and reconstruction efficiency respectively As we know that the cross section $\sigma_{a\to b} = \sigma_a\Gamma_b/\Gamma$, therefore, we can define $\sigma_{B\to D^{(*)}\tau\nu_\tau} = \sigma_P\mathcal{B}(B \to D^{(*)}\tau\nu_\tau)$, where σ_P is the $B\bar{B}$ production cross section. If we redefine our observable as $\sigma_{B\to D^{(*)}\tau\nu_\tau}$ than the errors in C_i can be written as

$$\begin{aligned} \delta C_i &= \sqrt{\frac{X'_{ii}\sigma_{B\to D^{(*)}\tau\nu_\tau}}{N_{sig}}} = \sqrt{\frac{X'_{ii}}{\mathcal{L}_{eff}}} = \sqrt{\frac{X_{ii}}{\sigma_P\mathcal{L}_{eff}}} \\ &= \sqrt{\frac{X_{ii}\mathcal{B}(B \to D^{(*)}\tau\nu_\tau)^{exp}}{N_{sig}}}, \end{aligned}$$

since $X'_{ii} = X_{ii}/\sigma_P$. The above-mentioned method, and the equations like (3.3) and (3.4), can be generalised for any other observables in $B \to D^{(*)}\tau\nu_\tau$ decay.

Since the data is consistent with the SM, if there is NP in $B \to D^{(*)}\tau\nu_\tau$ decays, the effect is expected to be small compared to their SM counterpart. The earlier model independent analysis [66], which is based on data by BABAR [118], shows that zero value of the new Wilson coefficients are consistent with the data. Therefore, we choose our starting point as $C_W = 0$ and find out errors in the extraction of those coefficients around that point. In addition to that, we assume that the error on C_i could be captured sufficiently well by just the leading-order terms.

In this analysis we have considered the following observables:

- The branching fractions, obtained by integrating the differential branching fractions over the full q^2 region, normalised by the full q^2 integrated branching fraction $\mathcal{B}_\ell =$

$\mathcal{B}(B \to D^{(*)}\ell\nu_\ell)$.

$$R(D^{(*)}) = \int dq^2 R_{D^{(*)}}(q^2), \tag{3.5}$$

with

$$R_{D^{(*)}}(q^2) = \frac{1}{\mathcal{B}_\ell}\frac{d\mathcal{B}(B \to D^{(*)}\tau\nu_\tau)}{dq^2}. \tag{3.6}$$

- τ polarisation asymmetry :

$$P_\tau^{R^{(*)}}(q^2) = P_\tau(q^2) R_{D^{(*)}}(q^2) \tag{3.7}$$

- τ forward-backward asymmetry :

$$\mathcal{A}_{FB}^{R^{(*)}}(q^2) = \mathcal{A}_{FB}(q^2) R_{D^{(*)}}(q^2) \tag{3.8}$$

,

- D^* longitudinal polarisation asymmetry :

$$P_{D^*}^{R}(q^2) = P_{D^*}(q^2) R_{D^*}(q^2) \tag{3.9}$$

In the above definitions, the detailed expression for $P_\tau(q^2)$, $\mathcal{A}_{FB}(q^2)$ and $P_{D^*}(q^2)$ are given in Sec.1.2.2. For forward backward asymmetries and the D^* polarisation, the C_is and the corresponding $f_i(q^2)$s are given in the Tables 3.2, and in the Appendix C.3.

Obs / C_i	$\mathcal{A}_{FB}^{R}(q^2)$	$\mathcal{A}_{FB}^{R^*}(q^2)$	$P_{D^*}(q^2)$
C_1	$\lvert 1 + C_{V_1} + C_{V_2}\rvert^2$	$\lvert 1 + C_{V_1}\rvert^2 - \lvert C_{V_2}\rvert^2$	$\lvert 1 + C_{V_1} - C_{V_2}\rvert^2$
C_2	$Re[(1 + C_{V_1} + C_{V_2})(C_{S_1}^* + C_{S_2}^*)]$	$\lvert 1 + C_{V_1} - C_{V_2}\rvert^2$	$\lvert C_{S_1} - C_{S_2}\rvert^2$
C_3	$Re[(1 + C_{V_1} + C_{V_2})C_T^*]$	$\lvert C_T\rvert^2$	$\lvert C_T\rvert^2$
C_4	$Re[(C_{S_1} + C_{S_2})C_T^*]$	$Re[(1 + C_{V_1} - C_{V_2})(C_{S_1}^* - C_{S_2}^*)]$	$Re[(1 + C_{V_1} - C_{V_2})(C_{S_1}^* - C_{S_2}^*)]$
C_5	–	$Re[(1 + C_{V_1})C_T^*]$	$Re[(1 + C_{V_1} - C_{V_2})C_T^*]$
C_6	–	$Re[C_{V_2} C_T^*]$	–
C_7	–	$Re[(C_{S_1} - C_{S_2})C_T^*]$	–

TABLE 3.2: Expressions of C_is for different observables.

All the above-mentioned observables are expected to be measured with good statistics in future experiments like Belle-II and LHCb. The corresponding errors on C_i can be obtained using the following relation

$$|\delta C_i| = \sqrt{\frac{X^{\ell}_{ii}}{\mathcal{B}_\ell \; \sigma_P \; \mathcal{L}_{eff}}}, \tag{3.10}$$

where $X^{\ell}_{ii} = X_{ii}\mathcal{B}_\ell$.

3.3 Analysis

In our analysis of the decay $B \to D\tau\nu_\tau$, it will be hard to estimate the uncertainties in the extractions of C_{V_1} and C_{V_2}, because they cannot be singled out from their SM counterpart (same f_is). The similar argument holds for the decay $B \to D^*\tau\nu_\tau$, however, in this decay we can estimate the error in the extraction of $Re(C_{V_2})$, see for instance Tables 3.1 and C.2 where f_2 associated with C_2 is different from f_1 associated with C_1. In Table 3.3, we list a few interesting cases of NP relevant for the observables in $B \to D\tau\nu_\tau$. In many cases, we assume $C_V = C_{V_1} + C_{V_2} = 0$, however, the assumption $C_V \neq 0$ will lead to the same set of parameters that has to be simultaneously extracted, if it is assumed that $C_V << 1$. Under such conditions C_1 can be treated as the Wilson coefficient of the vector operator. The different NP cases related to the observables in $B \to D^*\tau\nu_\tau$ are given in Tables 3.4, 3.5 and 3.6 respectively. In most cases, we assume $C_{V_1} = 0$, though the same set of parameters can be obtained without this assumption if $C_{V_1} << 1$. For τ forward-backward asymmetry in $B \to D^*\tau\nu_\tau$, we discuss mostly the cases with $C_{V_2} = 0$. In such cases, $C_1 = C_2$, and therefore we need to merge $f_1(q^2)$ and $f_2(q^2)$ into $f(q^2)(= f_1(q^2) + f_2(q^2))$ for the analysis. In all the other cases, when $C_{V_2} \neq 0$, the extracted uncertainties are large. We will discuss only one such interesting case.

Cases	Assumptions
a	$C_i \neq 0$, $i = 1, ..5$
b	$Re(C_T) = 0$
c	$Re(C_S) = 0$
d	$Re(C_S) = 0$ and $Re(C_T) = 0$
e	$C_T = 0$
f	$C_S = 0$

TABLE 3.3: Cases relevant for $R_D(q^2)$, $P^R_\tau(q^2)$ and $\mathcal{A}^R_{FB}(q^2)$. Here $C_S = C_{S_1} + C_{S_2}$, and in all the cases $C_{V_1} + C_{V_2} = 0$.

Cases	Assumptions
a^*	$C_S = 0$
b^*	$C_{V_2} = 0$
c^*	$C_T = 0$
d^*	$Re(C_S) = 0, \; C_{V_2} = 0$
e^*	$Re(C_S) = 0, \; C_T = 0, \; Im(C_{V_2}) = 0$
f^*	$C_S = 0, \; Re(C_T) = 0, \; Im(C_{V_2}) = 0$
g^*	$C_{V_2} = 0, \; Re(C_T) = 0, \; Re(C_S) = 0$
h^*	$C_{V_2} = 0, \; C_T = 0$
i^*	$C_{V_2} = 0, \; C_S = 0$
j^*	$Re(C_S) = 0, \; Re(C_T) = 0, \; Im(C_{V_2}) = 0$
k^*	$C_S = 0, \; C_T = 0$

TABLE 3.4: Different cases related to $R_{D^*}(q^2)$ and $P_\tau^{R^*}(q^2)$ in $B \to D^* \tau \nu_\tau$. Here $C_S = C_{S_1} - C_{S_2}$, and in all the cases $C_{V_1} = 0$.

Cases	Assumptions
1^*	$C_S = 0$
2^*	$C_{V_2} = 0, \; Re(C_T) = 0$
3^*	$C_{V_2} = 0, \; Re(C_S) = 0$
4^*	$C_{V_2} = 0, \; Re(C_T) = 0, Im(C_S) = 0$
5^*	$C_{V_2} = 0, \; C_S = 0$
6^*	$C_{V_2} = 0, \; Re(C_S) = 0, Re(C_T) = 0$
7^*	$C_{V_2} = 0, \; C_T = 0$

TABLE 3.5: Cases relevant in $\mathcal{A}_{FB}^{R^*}(q^2)$ with $C_{V_1} = 0$.

Cases	Assumptions
A	$C_i \neq 0, \; i = 1, .., 5$
B	$Re(C_T) = 0$
C	$Re(C_S) = 0$
D	$Re(C_S) = 0, \; Re(C_T) = 0$
E	$C_T = 0$
F	$C_S = 0$
G	$Re(C_S) = 0, \; C_T = 0$
H	$Re(C_T) = 0, \; C_S = 0$

TABLE 3.6: NP cases relevant in D^* polarisation asymmetry. Here, $C_V = C_{V_1} - C_{V_2} = 0$.

The numerical values of all the relevant parameters, like the form-factors, various masses and lifetimes are taken from ref. [154], and for the analysis we choose the central values of all the form-factors. The errors of the form-factors are considered while we estimate the additional errors on the extracted coefficients. We choose as benchmark values $\mathcal{B}(B \to D\ell\nu) = 2.32\%$, $\mathcal{B}(B \to D^*\ell\nu) = 5.31\%$, $\sigma_P = 1105.63\ pb$, and $\mathcal{L}_{eff} = 1fb^{-1}$.

Decay	$B \to D\tau\nu_\tau$			
Cases	b		c	
Obs. / $\lvert\delta C_i\rvert$	$R(D)$	P_τ^R	$R(D)$	P_τ^R
δC_1	0.60	0.37	0.60	0.37
$\delta\lvert C_S\rvert^2$	1.03	0.04	0.13	0.08
$\delta\lvert C_T\rvert^2$	0.62	0.70	1.12	0.72
$\delta(Re(C_S))$	1.31	0.06	-	-
$\delta(Re(C_T))$	-	-	1.15	0.12

Table 3.7: Numerical values of the 1σ error on C_is extracted from $R(D)$ and P_τ^R. For the cases $Re(C_i) = 0$, $\delta|C_i|^2 = \delta(Im^2(C_i))$.

In Table 3.7, we list our main results of the uncertainties in C_i extracted from the analysis of the $R(D)$ and P_τ^R corresponding to different cases listed in Table 3.3, while those for $R(D^*)$ and $P_\tau^{R^*}$, corresponding to the cases listed in Table 3.4, are given in Table 3.8. For a given case, we estimate the statistical significance of the simultaneous extraction of C_is. The numerical values are given only for parameters relevant to a particular case, while the rest are set to zero.

Decay Modes	$B \to D^*\tau\nu_\tau$									
Cases	a^*		b^*		c^*		d^*		e^*	
Obs. / Params.	$R(D^*)$	$P_\tau^{R^*}$	$R(D^*)$	$P_\tau^{R^*}$	$R(D^*)$	$P_\tau^{R^*}$	$R(D^*)$	$P_\tau^{R^*}$	$R(D^*)$	$P_\tau^{R^*}$
δC_1	7.22	13.70	289.17	116.82	28.44	14.08	2.01	0.65	1.28	1.25
$\delta\lvert C_S\rvert^2$	-	-	629.08	204.37	56.25	29.65	1.00	1.73	3.68	1.83
$\delta\lvert C_T\rvert^2$	4.30	1.96	11.86	4.62	-	-	0.03	0.04	-	-
$\delta(Re(C_S))$	-	-	529.3	191.49	6.81	2.20	-	-	-	-
$\delta(Re(C_T))$	28.27	36.92	36.71	45.37	-	-	0.35	0.24	-	-
$\delta(Re(C_{V_2}))$	47.10	18.51	-	-	14.21	7.03	-	-	0.63	0.63
$\delta Re[C_{V_2}C_T^*]$	15.70	17.19	-	-	-	-	-	-	-	-

Table 3.8: Numerical values of the 1σ error on C_is extracted from $R(D^*)$ and $P_\tau^{R^*}$. For the cases $Re(C_i) = 0$, $\delta|C_i|^2 = \delta(Im^2(C_i))$.

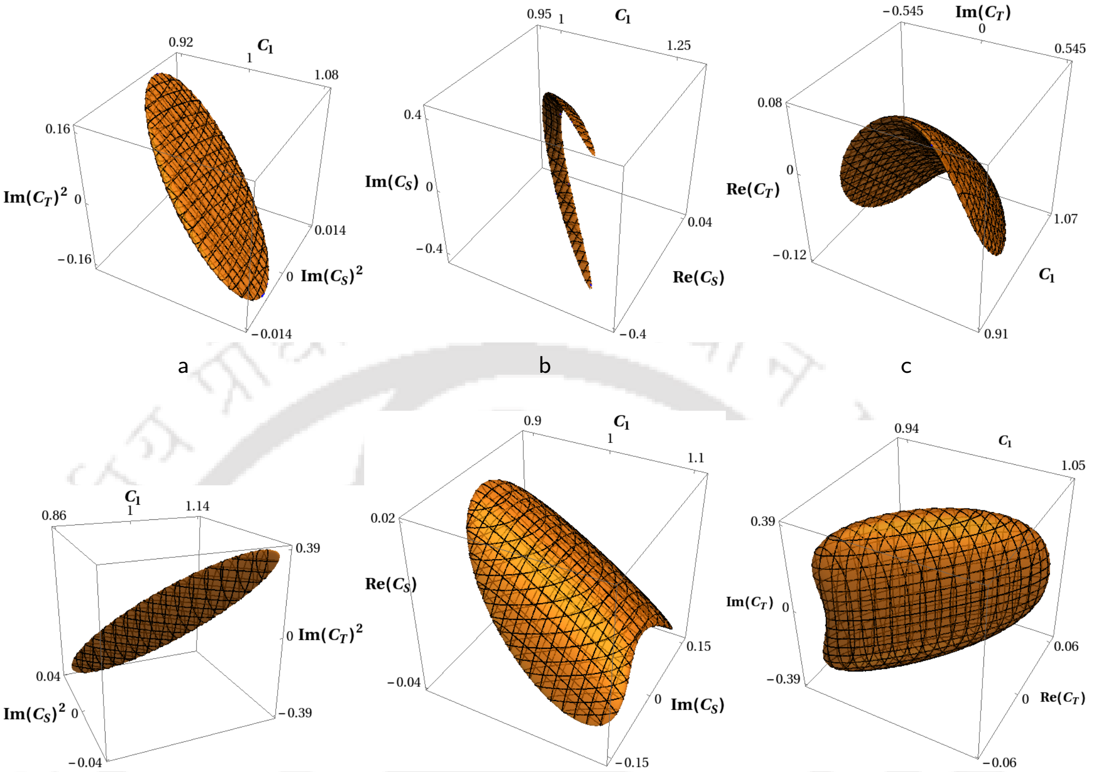

a b c

d e f

Fig. 3.1 Surfaces of constant $\chi^2 = 1$ for a few selected cases of different observables in $B \to D\tau\nu_\tau$.

In some more simplified cases, where the number of non-zero NP parameters are less, we compute the χ^2, which is defined as

$$\chi^2 = \sum_{i,j}(C_i - C_i^0)(C_j - C_j^0)V_{ij}^{-1},$$
$$\text{where,} \quad V_{ij} = \frac{X_{ij}}{\mathcal{B}_\ell \; \sigma_P \; \mathcal{L}_{eff}}. \tag{3.11}$$

The C_i^0s are the seed values, which can be considered as model inputs; as discussed earlier, we choose $C_i^0 = 0$, for $i \neq 1$, and $C_1^0 = 1$. The $\chi^2 = 1$ surfaces are perfect ellipsoids in C_i basis, and they indicate the $\pm 1\sigma$ errors in the determination of C_is. The constant $\chi^2 = 1$ surfaces are shown in Figs. 3.1, and 3.2. The largest and the smallest values in the figures represent $\pm 1\sigma$ errors of corresponding parameters.

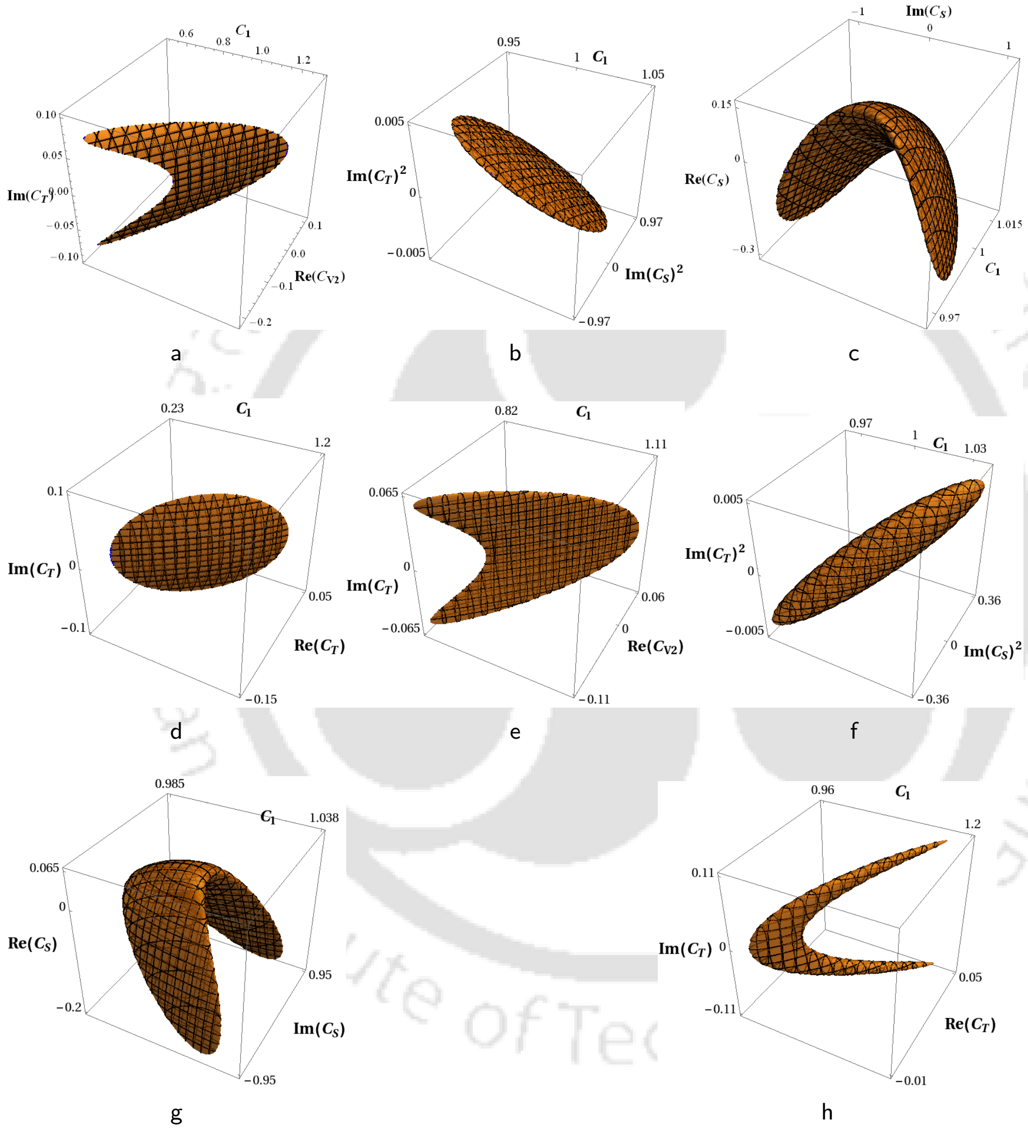

a b c

d e f

g h

Fig. 3.2 Surfaces of constant $\chi^2 = 1$ for a few selected cases of different observables shown in $B \to D^*\tau\nu_\tau$.

Cases / $\lvert\delta C_i\rvert$	b	c	d	e	f
$\lvert\delta C_1\rvert$	0.27	0.27	0.04	0.07	0.07
$\lvert\delta Re(C_S)\rvert$	0.40	-	-	0.05	-
$\lvert\delta Re(C_T)\rvert$	-	0.30	-	-	0.04
$\lvert\delta(Im(C_S)Im(C_T))\rvert$	0.11	0.11	0.01	-	-

TABLE 3.9: Numerical values of $|\delta C_i|$ extracted from the τ forward-backward asymmetry in $B \to D\tau\nu_\tau$.

3.3.1 Discussions

For case a, the uncertainties obtained from the simultaneous extraction of all the Wilson coefficients from the observable $R(D)$ shows that [2]

$$\frac{|\delta C_4|}{|\delta C_5|} \approx \frac{|\delta Re(C_S)|}{|\delta Re(C_T)|} \sim 1, \quad \frac{\delta |C_S|^2}{\delta |C_T|^2} \sim 2, \tag{3.12}$$

which shows that $R(D)$ is equally sensitive to the real part of C_S and C_T. The above result does not allow a direct comparison between the sensitivities to the imaginary part of the coefficients. The results obtained for all the other cases are shown in Tab. 3.7, and in Figs.3.1a, 3.1b and 3.1c. We note that if the Wilson coefficients are purely imaginary then $R(D)$ is more sensitive to $Im(C_S)$ compared to $Im(C_T)$. Also, it is important to note that this observable is more sensitive to the real part of the coefficients than the imaginary part. Comparing all the different cases considered for $R(D)$, it would be difficult to comment on the overall sensitivity of this observable to a particular type of NP interaction. However, in the next section we will see that there are distinct regions of q^2 which are sensitive to either scalar or tensor type interactions.

On the other hand, the analysis of $P_\tau^R(q^2)$ for case a gives

$$\frac{|\delta C_4|}{|\delta C_5|} \approx \frac{|\delta Re(C_S)|}{|\delta Re(C_T)|} \sim 0.5, \quad \frac{\delta |C_S|^2}{\delta |C_T|^2} \sim 2, \tag{3.13}$$

which shows an improvement in sensitivity to $Re(C_S)$ compared to $Re(C_T)$. The results obtained from all the other relevant cases are shown in Table 3.7, and in Figs. 3.1d, 3.1e, and 3.1f, which allow a case by case comparison between the results obtained from $R(D)$

---

[2] The results corresponding to the case a are not shown in the table, because the extracted uncertainties are very large ($>> 1$).

and P_τ^R. Interestingly, the extracted uncertainties are less compared to that extracted in $R(D)$. The sensitivity of this observable to tensor interaction is a little less, compared to scalar interaction, but it can be extracted with uncertainties less than 1.

As shown in Table 3.8, and in Fig. 3.2, the observables like $R(D^*)$ and $P_\tau^{R^*}$ are more sensitive to $|C_T|^2$ compared to any other new Wilson coefficients, almost in all the cases $|C_T|^2$ and $Re(C_T)$ can be extracted with small uncertainties. A case by case comparison shows that the above observables are more sensitive to C_T than C_S, and $\delta Re(C_T) < \delta Re(C_{V_2})$ but they are of same order. Also, when C_T is purely imaginary, we find $\delta Im(C_T) \approx \delta Re(C_{V_2})$, though $P_\tau^{R^*}$ have little better sensitivity to $Im(C_T)$. Therefore, these observables alone won't allow us to distinguish the contributions from right handed vector current to that of a tensor current. However, in the next section we will see that a bin by bin analysis of the q^2 distribution of the differential decay rate allows to discriminate the effects of these interactions.

However, when $C_T = 0$, both the observables are almost equally sensitive, though $\delta Re(C_S) < \delta Re(C_{V_2})$, to the real part of the vector and scalar Wilson coefficients. In case C_S is purely imaginary, $\delta Re(C_{V_2}) << \delta Im(C_S)$ i.e the observables are less sensitive to the imaginary part of C_S compared to the real parts of C_{V_2} and C_S. Again, we note that the extracted errors on C_is from $P_\tau^{R^*}$ are smaller than those in $R(D^*)$.

Cases $\lvert\delta C_i\rvert$	2^*	3^*	4^*	5^*	6^*	7^*
$\lvert\delta C_1\rvert$	1.30	2.41	0.40	0.27	0.52	0.04
$\delta\lvert C_T\rvert^2$	0.12	0.08	0.04	0.04	0.03	-
$\lvert\delta Re(C_S)\rvert$	16.30	-	1.72	-	-	0.02
$\lvert\delta Re(C_T)\rvert$	-	1.06	-	0.12	-	-
$\lvert\delta(Im(C_S)Im(C_T{}^*))\rvert$	2.48	2.41	-	-	0.26	-

TABLE 3.10: Numerical values of $|\delta C_i|$ extracted from τ forward backward asymmetry in $B \to D^*\tau\nu_\tau$.

The results of the analysis of forward-backward asymmetries and D^* polarisation are given in Tables 3.9, 3.10, and 3.11 respectively. The forward-backward asymmetry in $B \to D\tau\nu_\tau$ is equally sensitive to the scalar and tensor type interactions.

For case 1^* in $A_{FB}^{R^*}$, we find

$$\frac{\delta C_1}{\delta |C_T|^2} \approx 1, \quad \frac{\delta C_2}{\delta |C_T|^2} \approx 24, \tag{3.14}$$

and

$$\frac{\delta C_2}{\delta Re(C_T)} \approx 12, \tag{3.15}$$

where C_1 and C_2 are the functions of the Wilson coefficients of the vector operators. The approximate forms are given by

$$C_1 \approx 1 + 2Re(C_{V_1}), \; C_2 \approx 1 + 2Re(C_{V_1}) - 2Re(C_{V_2}). \tag{3.16}$$

It indicates that the τ forward-backward asymmetry in $B \to D^*\tau\nu_\tau$ is more sensitive to tensor Wilson coefficients than to a vector, in particular to C_{V_2}. In order to understand it better, we define

$$C_{12} = C_1 - C_2 \approx 2Re(C_{V_2}). \tag{3.17}$$

Therefore, a simple calculation shows that

$$\frac{\delta Re(C_{V_2})}{\delta Re(C_T)} = \frac{1}{2}\frac{\delta C_{12}}{\delta Re(C_T)} \approx 6. \tag{3.18}$$

In all the other cases with $C_{V_2} = 0$, the A_{FB} in $B \to D^*\tau\nu_\tau$ is more sensitive to the tensor interaction compared to the scalar. On the other hand the D^* polarisation is equally sensitive to the scalar and tensor interactions. Therefore, if future data shows large deviations from the SM predictions in all the observables like $R(D^*)$, A_{FB}^*, and D^* polarisation, that can be thought of as an indication of the presence of a new tensor type interaction. On other hand, if a deviation is only in $R(D^*)$ and not in the others, that could be an indication of a new vector interaction.

3.3.2 Bin-by-bin analysis

In general, the sensitivity to various NP interactions may also be q^2 dependent. Hence, we analyse the bin-by-bin q^2 distribution of the differential decay rate of $B \to D^{(*)}\tau\nu_\tau$ to look for more possibilities, and zoom in to the regions of q^2, within which the sensitivity to a specific type of new interaction is much larger than most other regions. In general

$\lvert\delta C_i\rvert$ \ Cases	A	B	C	D	E	F	G	H
$\lvert\delta C_1\rvert$	3.58	0.74	1.41	0.12	0.05	1.41	0.05	0.1
$\delta\lvert C_S\rvert^2$	16.63	3.39	0.55	0.55	0.77	-	0.54	-
$\delta\lvert C_T\rvert^2$	2.53	0.09	0.41	0.01	-	0.41	-	0.01
$\lvert\delta Re(C_S)\rvert$	7.05	1.40	-	-	0.20	-	-	-
$\lvert\delta Re(C_T)\rvert$	5.07	-	1.00	-	-	1.00	-	-

TABLE 3.11: The results obtained from the analysis of the D^* polarisation asymmetry in the decay $B \to D^*\tau\nu_\tau$.

the δC_is extracted from individual bins are very large, therefore in the figs. 3.3, 3.4 we plot $\delta\bar{C}_i = \delta C_i/N_{norm}$, where N_{norm} is some number used to normalised δC_i.

The results obtained from the analysis of the q^2 distribution of differential decay rate in $B \to D\tau\nu_\tau$ are presented in fig. 3.3, where the variations of the δC_is with q^2 are shown. The normalised uncertainties in the simultaneous extraction of $|C_S|^2$, $|C_T|^2$, $Re(C_T)$ and $Re(C_S)$, and their variations with q^2 are shown in figs. 3.3a and 3.3b respectively. On the other hand the variations of $\delta|C_S|^2$, and $\delta Re(C_S)$ with q^2 when $C_T = 0$ are shown in fig. 3.3d, while that for $\delta|C_T|^2$, and $\delta Re(C_T)$ when $C_S = 0$ are shown in fig. 3.3e. We note that in the low q^2 region ($\lesssim 7GeV^2/c^4$) the differential decay rate is sensitive to the scalar interaction [3], the sensitivity to tensor interaction in this region is very weak, whereas in the high q^2 region ($\gtrsim 7GeV^2/c^4$) it is rather sensitive to the tensor interaction. In case the Wilson coefficients are purely imaginary, in all the q^2 regions, the decay rate distribution is sensitive more to the scalar interaction (fig. 3.3c) than the others.

As we noted earlier, $R(D^*)$ is equally sensitive to C_{V_2} and C_T (case a^*), however, the analysis of the differential decay rate distributions show that (figs. 3.4e and 3.4d) it is sensitive to tensor interaction only in the very high and low q^2 regions, and it is sensitive to C_{V_2} in all the q^2 regions except the very low q^2 region. In fig. 3.4a the variations of $\delta Re(C_{V_2})$, $\delta Re(C_S)$, and $\delta|C_S|^2$ with the q^2 in the case $C_T = 0$ are shown, we note that in all the q^2 regions the decay rate is equally sensitive to vector and scalar interactions except in the very low q^2 region, where the sensitivity to $Re(C_S)$ is better than that to $Re(C_{V_2})$. We also study the cases when the NP interaction is scalar type. The q^2 distribution of the extracted errors on the respective parameters is shown in fig. 3.4c, which indicates that the decay rate is sensitive to scalar interactions only in the low q^2 region. If C_S and C_T

---

[3] In very low q^2 regions the q^2 distribution is also sensitive to C_1.

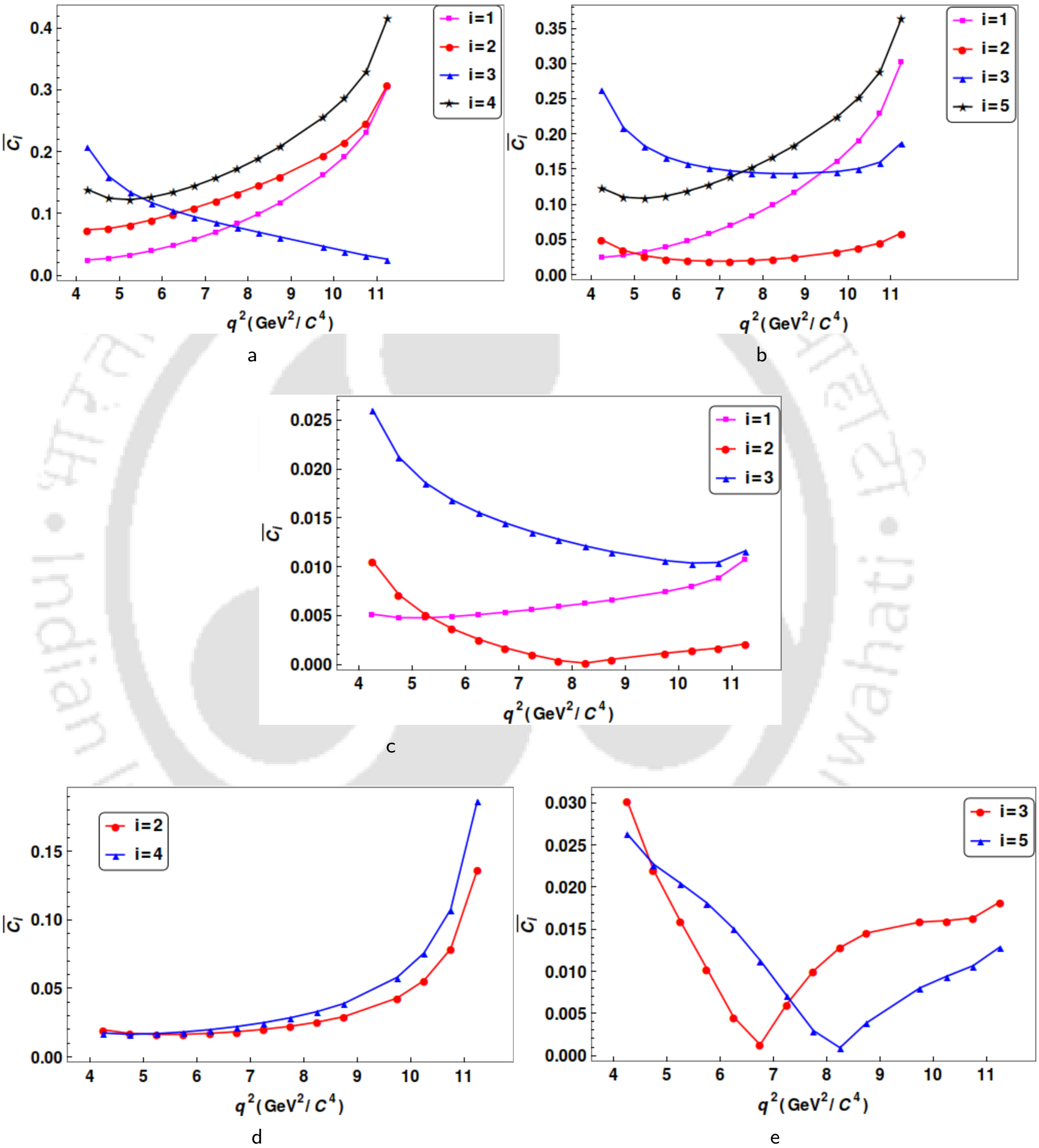

Fig. 3.3 Selected cases in $B \to D\tau\nu_\tau$, here, $\overline{C_i} = |\delta C_i|/N_{norm}$.

are purely imaginary than the q^2 distribution of the decay rate is sensitive to the tensor interactions in all the q^2 regions (fig. 3.4b).

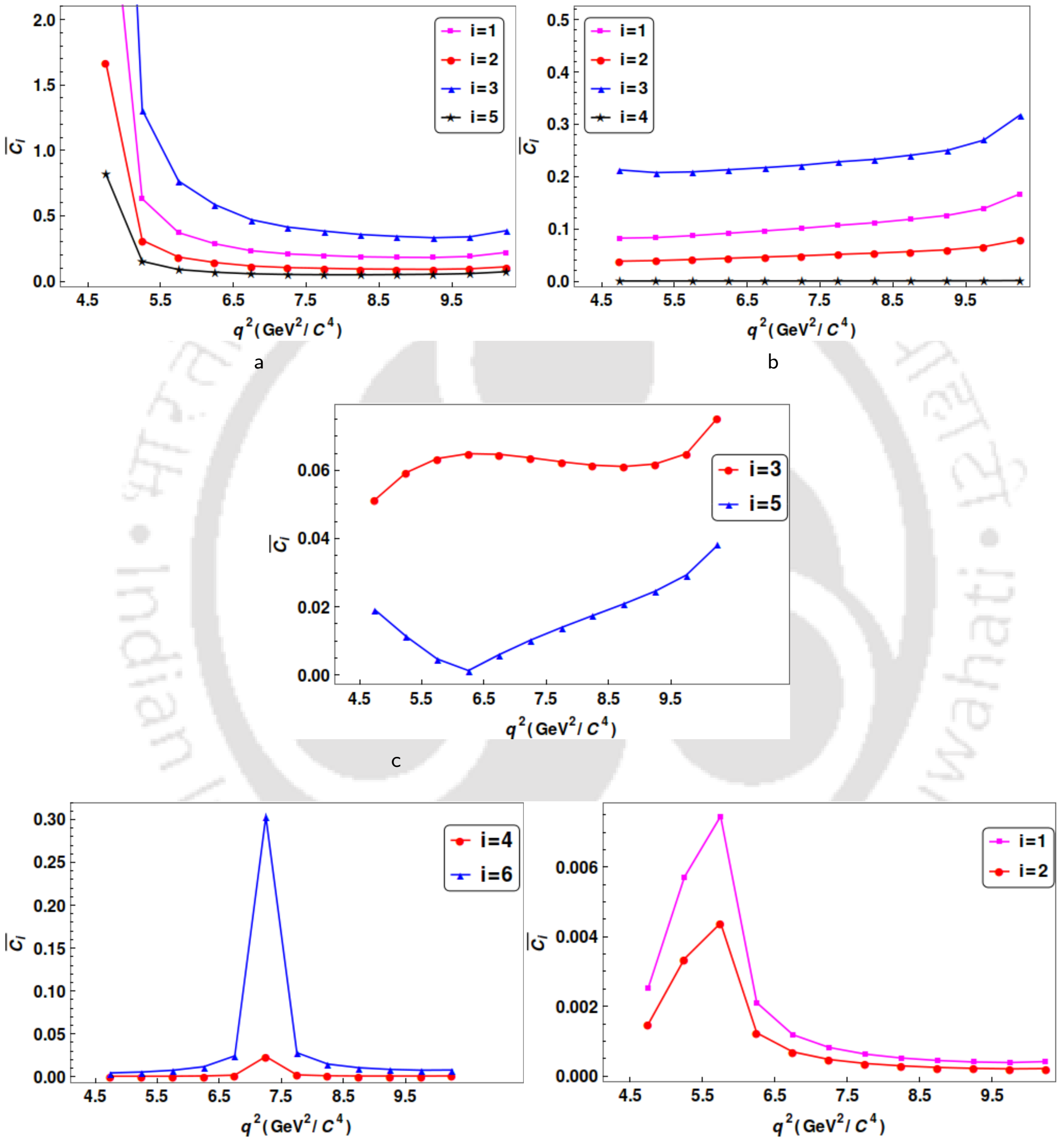

a b

c

d e

Fig. 3.4 Selected cases in $B \to D^*\tau\nu_\tau$, here, $\overline{C_i} = |\delta C_i|/N_{norm}$.

All these studies suggest that we could gain in NP sensitivity if we focus on specific

q^2 regions, which we may lose in the full q^2-integrated observables. We note that the sensitivity to a particular type of interaction is limited to particular regions of q^2. Therefore, the experimental data in the specific regions of q^2 could help us a better interpretation of the type of NP interactions, which may not be obtainable from q^2 integrated observables. As for example, if we see large deviations in data only in the very high and very low q^2 regions, that can be interpreted as due to the presence of a tensor interaction (fig. 3.4d). On the other hand, if we see deviations only in the low q^2 (< 7) bins, that could be due to a new scalar interaction (fig. 3.4c). Finally, if data shows deviations in most of the q^2 bin except the very low q^2, this can be due to the presence of new vector interaction (fig. 3.4e).

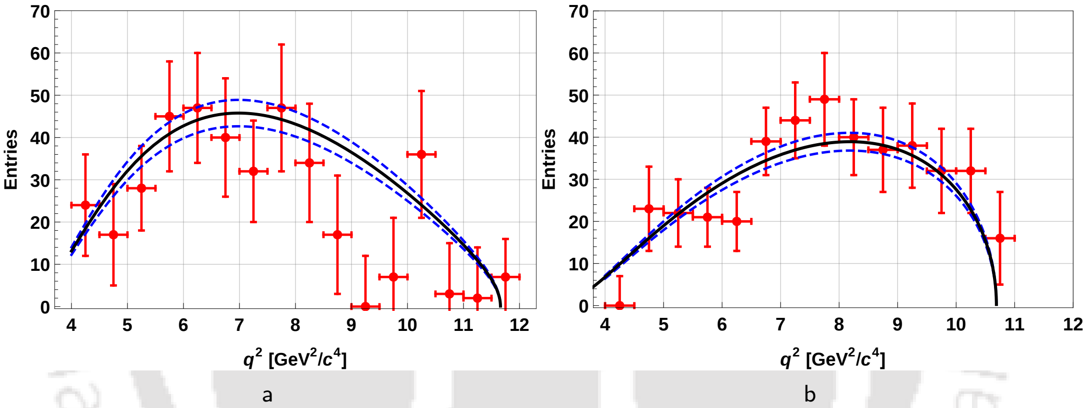

Fig. 3.5 Measured q^2 distribution of the events in $B \to D\tau\nu_\tau$ (left) and $B \to D^*\tau\nu_\tau$ (right) decays [118]. The black lines represent the q^2 distribution predicted in the SM, obtained from the respective differential branching fractions.

In order to explain our point we take the example of the q^2 distributions of the measured events in $B \to D^{(*)}\tau\nu_\tau$, which are shown in Fig.(3.5). The plots are generated using the data given in ref. [118, 155, 156]. The predicted q^2 distributions in SM with the central values of the form factors are shown by black lines, blue dotted lines represent the errors in SM. In Fig.(3.5a), we see that the data is not fully consistent with the SM in the region $8.0 < q^2 < 11$, which is the region where the decay rate distribution is sensitive to tensor interaction, as analysed above in the decay $B \to D\tau\nu_\tau$. At the moment it is hard to conclude anything, and we have to wait for better statistics. From Fig.(3.5b) we see distinct regions of q^2 where the data is not fully consistent with the SM prediction, and our analysis suggests that those regions could potentially be very sensitive to NP effects. Again, because of poor statistics it is premature to conclude anything. Therefore, the experimental effort should be in gathering more statistics in specific regions of q^2 potentially sensitive to NP, which may in turn help the clean extraction of NP couplings.

As mentioned above, the numerical estimates are done with central values of all the relevant parameters taken from [154]. Numerical instability of our results could be main source of uncertainty in our estimates. The numerical results of X_{ij}, which depend on the matrix inversion of M_{ij}, are often unstable; even a tiny variation of M_{ij} could change X_{ij} significantly. This is why, when we estimate the statistical uncertainties in simultaneous extractions of the Wilson coefficients, we allowed only stable solutions. We calculate the selected δC_i first to m^{th} and then to $(m-1)^{th}$ decimal places, and obtain $\delta C_i{}^{[m]}$ and $\delta C_i{}^{[(m-1)]}$ respectively. We consider the results as stable only when $(\delta C_i{}^{[m]} - \delta C_i{}^{[(m-1)]})/\delta C_i{}^{[m]} < 0.01$. We checked the stability up to $m = 10$, and in most of the cases presented above, our results are very much stable, and the error due to this is negligible. As we can see from the expressions of δC_i, the other sources of errors in our estimates are given by the errors in $f_i(q^2)$, σ_P , $\mathcal{L}_{eff}$, and $\mathcal{B}_\ell$. It is straight forward to estimate the errors due to σ_P , $\mathcal{L}_{eff}$, and $\mathcal{B}_\ell$.

Cases		δC_i	$\delta C_i{}^+$	$\delta C_i{}^-$	$\pm\%Err.$
d	C_1	0.082	0.079	0.087	5.032
	$Im(C_S)^2$	0.013	0.013	0.014	5.032
	$Im(C_T)^2$	0.168	0.160	0.177	5.032
e	C_1	0.240	0.229	0.253	5.031
	$\|C_S\|^2$	0.274	0.261	0.289	5.031
	$Re(C_S)$	0.354	0.337	0.373	5.031

TABLE 3.12: Numerical values of δC_is, and $\delta C_i{}^+$ ($\delta C_i{}^-$) considering +10% (-10%) errors in $f_i(q^2)$ for few cases of $R(D)$. The % error is given by $(\delta C_i - \delta C_i{}^\pm)/\delta C_i$.

However, the estimate due to $f_i(q^2)$s are not that straight forward since M_{ij}s depend solely upon them. The main sources of uncertainties in f_is, including the SM, are the form-factors. Errors due to other parameters, like CKM element etc, are canceled in the ratios. In the tables 3.12, and 3.13, we consider a few cases and give a rough estimate of the uncertainties due to the errors in $f_i(q^2)$. The overall error is about ± 5% in the extraction of δC_is, if we consider the errors in $f_i(q^2)$s are about ± 10%. We also estimate the errors in δC_i by considering the actual errors in all the form-factors given in ref. [154], and find that they are even smaller than whatever we have shown in the above mentioned tables. Finally, we would like to comment that the estimated errors due to form-factors, and the other experimental parameters will have almost equal impact on all the extracted δC_is, which is also small. Therefore, our conclusions about the relative sensitivities will not change.

Cases		δC_i	$\delta C_i{}^+$	$\delta C_i{}^-$	$\pm\% Err.$
f^*	C_1	0.448	0.427	0.472	5.032
	$Re(C_{V_2})$	0.211	0.201	0.222	5.032
	$Im(C_T)^2$	0.006	0.0058	0.0065	5.032
g^*	C_1	0.042	0.040	0.044	5.032
	$Im(C_S)^2$	0.961	0.916	1.013	5.032
	$Im(C_T)^2$	0.0048	0.0046	0.0051	5.032

TABLE 3.13: Numerical values of δC_is, and $\delta C_i{}^+$ ($\delta C_i{}^-$) considering +10% (-10%) errors in $f_i(q^2)$ for few cases of $R(D^*)$. The % error is given by $(\delta C_i - \delta C_i{}^{\pm})/\delta C_i$.

3.4 Summary

We use the optimal observable technique to test the sensitivities of the various observables in $B \to D^{(*)}\tau\nu_\tau$ to the various NP interactions, like new vector, scalar and tensor interactions. Numerically, we find that the observables in $B \to D\tau\nu_\tau$ are more or less equally sensitive to scalar and tensor interactions, only exception is the τ polarisation asymmetry, where $\delta Re(C_S) < \delta Re(C_T)$ but they are of same order. Therefore, even if the measured values of the observables deviate from their SM expectations, a priori it would be hard to decide what type of new interaction will it be. However, the analysis of the q^2 distribution of the decay rate allows us to separate the regions of q^2 which are sensitive to scalar interaction (low q^2) and tensor interaction (high q^2).

The overall sensitivity of the observables in $B \to D^*\tau\nu_\tau$ is more towards tensor interactions, in particular to $|C_T|^2$. Also, we note that $\delta Re(C_T) < \delta Re(C_{V_2})$ but they are of same order, hence, we need better statistics to distinguish their effects. The decay $B \to D^*\tau\nu_\tau$ has very poor sensitivity to scalar interaction compared to the tensor interaction, the only exceptions being the D^* polarisation, $A_{FB}^{R^*}$. However, in the absence of tensor interactions, the decay $B \to D^*\tau\nu_\tau$ is equally sensitive to real part of both the vector and scalar Wilson coefficients, sensitivity to $|C_S|^2$ is much less compared to the real parts. However, the analysis of the q^2 distributions of the decay rate shows distinct regions of q^2, which are sensitive to vector, scalar, and tensor interactions respectively.

These sensitivities are lost in the full q^2 integrated observables. Present data on different bins do not have sufficient statistics to conclude anything, more precise data could help us to pinpoint the type of NP interaction. Therefore, in an experiment, the priority should be given to gaining statistics at those regions of q^2.

We note that both the decay modes are more sensitive to the real part of the coefficients compared to imaginary part. Among the various observables, τ polarisation asymmetries have better sensitivity to the relevant new coefficients (C_i); the uncertainties on the extracted C_is are either less or comparable to that obtained in others. Therefore, future data on τ polarisation asymmetries could put tighter constraints on the NP parameter space.

Chapter 4

Looking for new physics in $B \to D^{(*)}\tau\nu_\tau$ decay from the available data

4.1 Introduction

This chapter focuses on the NP analysis of $B \to D^{(*)}\tau\nu_\tau$ decays in view of the available binned data from different experimental collaborations like *BABAR* and Belle. Also, we have defined few scenarios where we have incorporated the data on q^2- integrated $R(D^{(*)})$ from *BABAR*, Belle and LHCb. The present experimental status of the observables $\mathcal{R}(D^{(*)})$ is summarized in Fig.1.3. From the figure, we note that the correlation contour obtained after averaging the Belle measurements [119, 157, 158], which is more than 3σ away from the SM prediction, lies in between the SM expectation and the *BABAR* measurement [118]. LHCb results on $\mathcal{R}(D^*)$ [122] are 2.1σ larger than the value expected in SM. Although the Belle average is slightly smaller than the LHCb and *BABAR* results, it is still considerably larger than the SM prediction.

According to the bin-by-bin analysis, discussed in section 3.3.2, we realise that the sensitivity to a particular type of interaction is more apparent in the binned data, compared to that from the integrated observables like $R(D^{(*)})$ [153]. On the other hand, as the measured values of $R(D^{(*)})$ are highly model sensitive due to the model dependence of the kinetic distribution, one may get different signal yields per bin from fits using different models. Consequently, the values obtained from fits assuming only the SM background should not be used to fit the NP parameters. Although we use the background-subtracted and normalized binned data for most of our analysis, we compensate for any systematic errors coming from such assumption by doing a separate study with overestimated errors and their correlations.

As discussed in chapter 1, the $B \to D^{(*)}\ell\nu_\ell$ ($\ell = \mu$ or e) decays are less sensitive to any kind of NP effects. Hence, these decays are appropriate for the extractions of $|V_{cb}|$ and the various form-factors associated with it. The same form-factors are also relevant to describe $B \to D^{(*)}\tau\nu_\tau$ decays, though there are two additional form-factors which are extracted using HQET inputs. The output of the fit are used to predict the various observables associated with $B \to D^{(*)}\tau\nu_\tau$ decays in the SM. Since there are large number of parameters involved with the form-factors, to fit them one needs large number of data set. In this analysis, we have used the available bin data on the decay distributions of $B \to D^{(*)}\tau\nu_\tau$ to fit the form-factors and compared them with those obtained from $B \to D^{(*)}\ell\nu_\ell$ decays. In this part of the analysis, we have not added any new physics contributions in $b \to c\tau\nu_\tau$ decays. Therefore, any discrepancies between the two fit results will indicate a possible new effect in $B \to D^{(*)}\tau\nu_\tau$ decays. Since the form-factors are defined as matrix elements of hadronic currents of different Lorentz structures, the probable missmatch will help to identify the helicity structure(s) of the new contributions.

In an another part of the analysis (section 4.3), we have considered the contributions from different NP interactions in $B \to D^{(*)}\tau\nu_\tau$, but not in $B \to D^{(*)}\ell\nu_\ell$. Our goal will be the search for new interactions most compatible with and best elucidates the present data. Throughout our analysis we will use the q^2-binned data on the decay rate as well the data on $R(D^{(*)})$. In section 4.4 we have summerized the interisting outcomes of this analysis. The analysis presented here is based on [159].

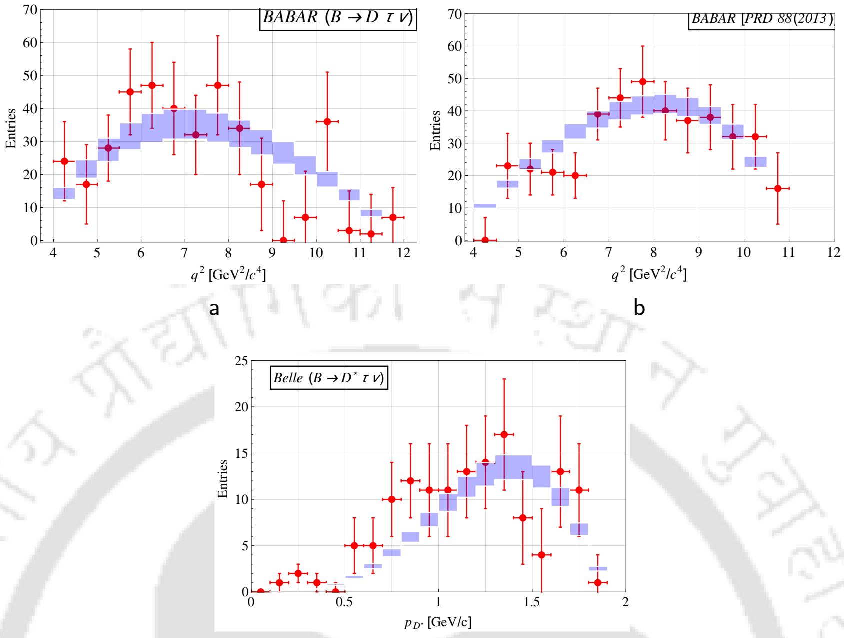

a

b

c

Fig. 4.1 Fig.s 4.1a and 4.1b are the measured background subtracted q^2-distributions for $\overline{B} \to D\tau\overline{\nu}_\tau$ and $\overline{B} \to D^*\tau\overline{\nu}_\tau$ events, extracted from the BABAR data [118]. Fig. 4.1c is the background subtracted and normalized momentum distribution of D^* extracted from the Belle data [157]

4.2 Form-factors from $B \to D^{(*)}\tau\nu_\tau$

4.2.1 Formalism

Several parameters parameterissing the form-factors, otherwise not accessible in $\bar{B} \to D^{(*)}\ell^-\bar{\nu}_\ell$ decays, appear in $\bar{B} \to D^{(*)}\tau^-\bar{\nu_\tau}$ decays. Detailed discussion on the definitions of these form-factors in $B \to D^{(*)}\tau\nu_\tau$ decay channels are given in section 1.2.2. By taking the binned data from the q^2-distribution of the decay rates in $\bar{B} \to D^{(*)}\tau^-\bar{\nu_\tau}$ normalized by $d\Gamma(B \to D^{(*)}\ell\nu_\ell)/dq^2$, we fit all of these form-factor parameters. The only exceptions are $V_1(1)$ and $h_{A_1}(1)$ which will cancel in the ratios.

Fig.s 4.1a and 4.1b show efficiency-corrected q^2-distributions for $\overline{B} \to D\tau^-\overline{\nu}_\tau$ and $\overline{B} \to D^*\tau^-\overline{\nu}_\tau$ events with $m^2_{miss} > 1.5$ GeV^2, scaled to results of isospin-constrained fit extracted from the $BABAR$ [118] data. The B^0 and B^+ samples are combined and the normalization and background events are subtracted. The uncertainty on the data

Experiment	Channel	Input	Value
BABAR [118]	$\overline{B} \to D\tau^-\overline{\nu}_\tau$	N_{sig} N_{norm} $\epsilon_{sig}/\epsilon_{norm}$	489 ± 63 2981 ± 65 0.372 ± 0.010
	$\overline{B} \to D^*\tau^-\overline{\nu}_\tau$	N^*_{sig} N^*_{norm} $\epsilon^*_{sig}/\epsilon^*_{norm}$	888 ± 63 11953 ± 122 0.224 ± 0.004
Belle(2016) [157]	$\overline{B} \to D^*\tau^-\overline{\nu}_\tau$	N^*_{sig} N^*_{norm} $\epsilon^*_{norm}/\epsilon^*_{sig}$	231 ± 23 2800 ± 57 1.289 ± 0.015
LHCb [122]	$\overline{B} \to D^*\tau^-\overline{\nu}_\tau$	$R(D^*)$	0.336 ± 0.027 ± 0.030
Belle(2015) [119]	$\overline{B} \to D\tau^-\overline{\nu}_\tau$	$R(D)$	0.375 ± 0.064 ± 0.026
	$\overline{B} \to D^*\tau^-\overline{\nu}_\tau$	$R(D^*)$	0.293 ± 0.038 ± 0.015
Belle(Latest) [158]	$\overline{B} \to D^*\tau^-\overline{\nu}_\tau$	$R(D^*)$	0.276 ± 0.034 $^{+0.029}_{-0.026}$

TABLE 4.1: Experimental inputs for fits. Only statistical uncertainties are supplied for $N^{(*)}_{norm(sig)}$. Whenever two uncertainties are quoted, they are the statistical and systematic ones respectively.

points includes the statistical uncertainties of data and simulation. Fig. 4.1c is the background subtracted and normalized momentum distribution of D^* for $\overline{B} \to D^*\tau^-\overline{\nu}_\tau$ events extracted from the Belle [157] data. Here also, the B^0 and B^+ samples are combined and the normalization and background events are subtracted. The light blue histogram represent the SM prediction for the same in each individual bin. We note that both Belle and *BABAR* binned data show deviations from SM predictions.

4.2.2 χ^2 analysis

To fit the parameters of the form-factors, we have performed a test of significance (goodness of fit) by defining a χ^2 statistic. Detailed discussion on this fitting procedure is given in section 2.3. In this analysis, the χ^2 is a function of the parameters parameterizing the form-factors, which is defined as

$$\chi^2_{Lat} = \sum_{i,j=1}^{\text{bins}} \left(R(D^{(*)})_i^{exp} - R(D^{(*)})_i^{th} \right) V_{ij}^{-1} \left(R(D^{(*)})_j^{exp} - R(D^{(*)})_j^{th} \right), \tag{4.1}$$

where

$$R(D^{(*)})_{bin}^{th} = \frac{\int_{q^2_{\min}}^{q^2_{\max}} \left(d\Gamma\left(\overline{B} \to D^{(*)}\tau^- \overline{\nu}_\tau\right)/dq^2 \right) dq^2}{\int_{\text{full } q^2} \left(d\Gamma\left(\overline{B} \to D^{(*)}\ell\overline{\nu}_\ell\right)/dq^2 \right) dq^2}, \tag{4.2}$$

$$R(D^{(*)})_{bin}^{exp} = \begin{cases} \dfrac{N_{bin}^{(*)}}{N_{norm}^{(*)}} \times \dfrac{\epsilon_{norm}^{(*)}}{\epsilon_{sig}^{(*)}} & \text{BABAR} \\ \dfrac{1}{2\mathcal{B}(\tau^- \to \ell^- \bar{\nu}_\ell \nu_\tau)} \dfrac{N_{bin}^{(*)}}{N_{norm}^{(*)}} \times \dfrac{\epsilon_{norm}^{(*)}}{\epsilon_{sig}^{(*)}} & \text{Belle.} \end{cases} \tag{4.3}$$

Here V_{ij} is the covariance matrix. It comprises of $\sigma^2_{exp,\ bin}$, the experimental uncertainties obtained by propagating the uncertainties of individual parts in the r.h.s of eq.(4.3). As input, we consider the central values of number of events $N_{bin}^{(*)}$, along with their errors, for each q^2 or p_{D^*}-bin depending on whether we are analyzing the $BABAR$ or the Belle data. The total signal yield $N_{sig}^{(*)}$, along with the errors are given in table 4.1. For simplicity and due to lack of knowledge of q^2-distribution of the efficiencies, we have taken the ratio of efficiencies $\epsilon_{sig}^{(*)}/\epsilon_{norm}^{(*)}$ to be constant over all the q^2-regions and equal to the value shown in table 4.1. In eqs. (4.2) and (4.3), $q^2_{max(min)}$ are the end points of a particular bin. For the denominator in eq.(4.2), we integrate over the whole allowed phase space (from $q^2 = m_\ell^2$ to $q^2 = (m_B - m_{D^{(*)}})^2$).

In defining V_{ij}, we follow these procedures:

1. Our V comprises of two parts - the statistical covariance matrix V^{stat} and the systematic one, V^{syst}. So, $V^{exp} = V^{stat} + V^{syst}$. As there is no information available to us about the systematic uncertainties and their correlations on the binned data, we do two separate analyses.

2. The first analysis is done using only the data available to us, i.e. V^{syst} is set to be zero and $V_{ij}^{stat} = \delta_{ij}\ \delta R_i^{exp}\ \delta R_j^{exp}$ (here δ_{ij} is the Kronecker delta). We will call this "Fit-1" from hereon.

3. The second analysis is done assuming the systematic uncertainties to be the same as the statistical ones and 100% systematic correlation, i.e. $V_{ij}^{syst} = \delta R_i^{exp}\ \delta R_j^{exp}$ and V_{ij}^{stat} defined as earlier. We will call this "Fit-2" from hereon.

The utility of considering the systematic uncertainties to be the same as statistical ones and considering 100% systematic correlations in the second analysis are multi-pronged. First of all, as the statistical uncertainties on the binned data are quite large, this makes the systematic errors similarly large and that in turn can conservatively account for the possible systematic errors coming from *a*) the 'model-dependence' of the 'background-subtracted' binned data as mentioned in section 4.3.1 and *b*) the dependence of the shape of the q^2-distribution on the experimental cuts on the leptons and hadrons. Secondly, separately analyzing the data in both under-correlated and over-correlated ways and comparing them, gives us an idea of the dependence of the analysis on these unknown systematic bin-bin correlations.

The Belle results [157] used here is the first measurement of $R(D^*)$ using semileptonic tagging method for the "other B", referred to as B_{tag} and instead of a q^2-distribution, the momentum distribution of D^* and ℓ are given. For our analysis, we note that $p_{D^*}^2 = \left(\frac{m_B^2+m_{D^*}^2-q^2}{2m_B}\right)^2 - m_{D^*}^2$, and using this, eq.(4.2) can be calculated for each bin in the p_{D^*}-distribution by converting the limits of integration appropriately. For $R(D^*)_{bin}^{exp}$, we use eq.(4.3). We do not use those bins for which central values of $N_{bin}^{(*)} \leq 0$.

To utilize the fact that $V_1(1)$ and $h_{A_1}(1)$ get canceled respectively in $R(D)$ and $R(D^*)$, $R(D^{(*)})_{bin}$ is used instead of $N_{bin}^{(*)}$. So, the χ^2_{Lat} is a function of ρ_D^2 and Δ for $R(D)_{bin}$ and a function of $\rho_{D^*}^2$, $R_1(1)$, $R_2(1)$ and $R_0(1)$ for $R(D^*)_{bin}$.

4.2.3 Fit Results

The fit results for the parameters of the form-factors are listed in tables 4.2 and 4.4 for 'Fit-1' and 'Fit-2' respectively. We find the distribution of the residuals for all those fits and check whether that distribution is accordant with a normal distribution with mean 0 and variance 1 (with the null hypothesis H_0 that this is true). p-values obtained in our chosen normality test (S-W) quantify the probability of H_0 being true.

After the minimization, we find the uncertainties of and correlations between the parameters around their best fit points. A general approach to find these is to construct

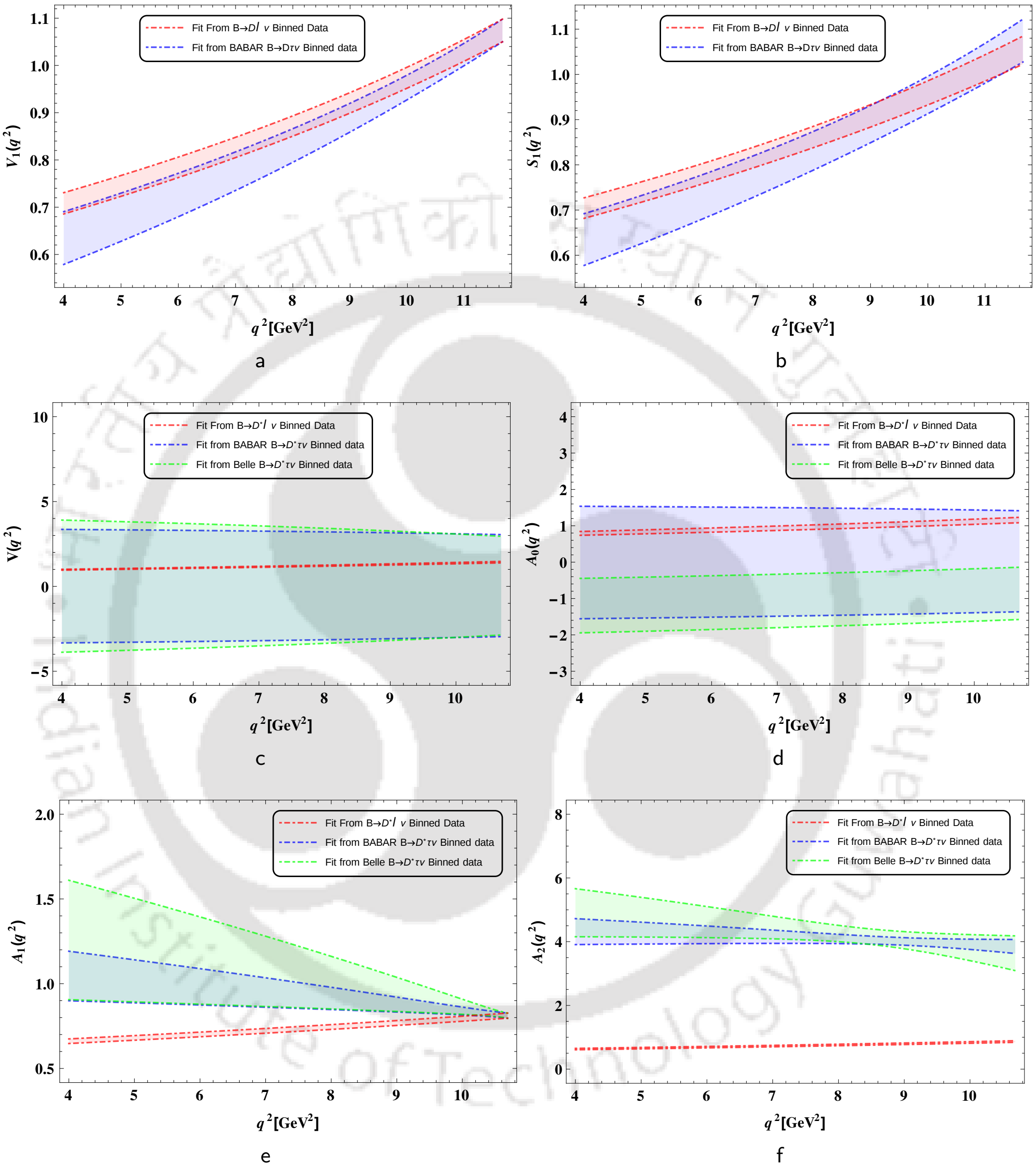

a b c d e f

Fig. 4.2 Results obtained from ‘Fit-1’. Fig.s 4.2a and 4.2b are the q^2 dependence of form-factors for semileptonic $b \to c$ transitions. Red (dotted) and blue (dot-dashed) lines enclose $\pm 1\sigma$ regions for the form-factors with parameters fitted from $\overline{B} \to D\ell\overline{\nu}_\ell$ (world average) and $\overline{B} \to D\tau\overline{\nu}_\tau$ decays (BABAR) respectively. The rest of the figures are for form-factors for $\overline{B} \to D^*\ell\overline{\nu}_\ell$ and $\overline{B} \to D^*\tau\overline{\nu}_\tau$ decays. Here green (solid) lines enclose the region for $\overline{B} \to D^*\tau\overline{\nu}_\tau$ decays (Belle).

Obs.	Par.s	Value	χ^2_{min}	$d.o.f$	Normality (S-W)
BABAR $R(D)_{bin}$	Δ	-0.04 ± 2.00	9.6	12	0.20
	ρ^2_D	1.43 ± 0.18			
$R(D^*)_{bin}$	$\rho^2_{D^*}$	-0.55 ± 0.66	5.4	8	0.25
	$R_1(1)$	0.04 ± 2.96			
	$R_2(1)$	3.79 ± 0.20			
	$R_0(1)$	0.02 ± 1.37			
Belle $R(D^*)_{bin}$	$\rho^2_{D^*}$	-1.52 ± 1.61	8.7	13	0.91
	$R_1(1)$	0.04 ± 2.86			
	$R_2(1)$	3.58 ± 0.53			
	$R_0(1)$	-0.84 ± 0.71			

TABLE 4.2: Fit-I Results of parameters parameterizing the form-factors in HQET. The last column lists the results of the hypothesis test (Shapiro-Wilk) for assessment of goodness-of-fit.

Channel	Correlation	BABAR	Belle (2016)
$\overline{B} \to D^*\tau\overline{\nu}_\tau$	$C\left(\rho^2_{D^*},\ R_1(1)\right)$	0.057	0.023
	$C\left(\rho^2_{D^*},\ R_2(1)\right)$	0.907	0.928
	$C\left(\rho^2_{D^*},\ R_0(1)\right)$	-0.004	-0.741
	$C\left(R_1(1),\ R_2(1)\right)$	0.082	0.024
	$C\left(R_1(1),\ R_0(1)\right)$	0.000	-0.008
	$C\left(R_2(1),\ R_0(1)\right)$	0.007	-0.861
$\overline{B} \to D\tau\overline{\nu}_\tau$	$C\left(\Delta,\ \rho^2_D\right)$	0.146	-

TABLE 4.3: Correlations between the fitted form-factor parameters from Fit-I.

the ‘Hessian Matrix’ H, which is the matrix of second order partial-derivatives of the test-statistic with respect to the parameters; this describes the local curvature of a function of many variables, and find its inverse. This constitutes the ‘error matrix’, square roots of whose diagonal elements give us the ‘standard error’ of the parameters and the normalized matrix (w.r.t the errors) makes the ‘correlation matrix’. We list such errors in tables 4.2 and 4.4 and relevant correlations in tables 4.3 and 4.5.

In the following we will discuss the outcome of our analysis, and compare our fit results with that determined by HFAG [72] (also given in eq. (1.37)):

- We fit ρ^2_D only using the $BABAR$ data, the obtained values are consistent with that

Obs.	Par.s	Value	χ^2_{min}	$d.o.f$	Normality (S-W)
BABAR $R(D)_{bin}$	Δ	-0.03 ± 2.25	8.71	12	0.14
	ρ^2_D	0.92 ± 0.60			
$R(D^*)_{bin}$	$\rho^2_{D^*}$	-0.54 ± 0.73	5.13	8	0.55
	$R_1(1)$	0.04 ± 1.99			
	$R_2(1)$	3.93 ± 0.31			
	$R_0(1)$	0.03 ± 0.76			
Belle $R(D^*)_{bin}$	$\rho^2_{D^*}$	-3.03 ± 2.24	6.62	13	0.68
	$R_1(1)$	0.04 ± 2.31			
	$R_2(1)$	3.78 ± 0.45			
	$R_0(1)$	0.03 ± 0.93			

TABLE 4.4: Fit-II Results of parameters parameterizing the form-factors in HQET.

Channel	Correlation	BABAR	Belle (2016)
$\overline{B} \to D^*\tau\overline{\nu}_\tau$	$C\left(\rho^2_{D^*},\ R_1(1)\right)$	0.031	0.015
	$C\left(\rho^2_{D^*},\ R_2(1)\right)$	0.698	0.563
	$C\left(\rho^2_{D^*},\ R_0(1)\right)$	0.011	0.004
	$C\left(R_1(1),\ R_2(1)\right)$	0.035	0.021
	$C\left(R_1(1),\ R_0(1)\right)$	0.000	0.000
	$C\left(R_2(1),\ R_0(1)\right)$	0.018	0.012
$\overline{B} \to D\tau\overline{\nu}_\tau$	$C\left(\Delta,\ \rho^2_D\right)$	0.07	-

TABLE 4.5: Correlations between the fitted form-factor parameters from Fit-II.

determined by the HFAG at 1σ. Our fitted values of Δ include $\Delta = 1 \pm 1$, so far, which is used in the prediction of $R(D)$ by *BABAR* [118].

- The analysis of the *BABAR* bin data on $R(D^*)$ from both 'Fit-1' and 'Fit-2' shows that the fitted parameters like $\rho^2_{D^*}$ and $R_1(1)$ are consistent within 2σ, with HFAG. However, $R_2(1)$ shows a large deviation (more than 10σ away). It is important to note that we can extract $R_2(1)$ with relatively small error.

- After analyzing the data by Belle on $R(D^*)$ from 'Fit-1', we obtain large errors on $\rho^2_{D^*}$ and $R_1(1)$, and they are consistent with the fitted value by HFAG at 1σ. 'Fit-2' increases both the best-fit value and errors of $\rho^2_{D^*}$ even more. Also in this case, $R_2(1)$ fits with a small error, and shows a large deviation from that determined by HFAG.

- Whereas the analysis of $R(D^*)$ from 'Fit-1' results obtained using *BABAR* and Belle binned data (table 4.2) are roughly consistent with each other, including the best-fit values of $R_0(1)$, the same analysis from 'Fit-2' (table 4.4) actually makes the results compatible. So much so, that the $R_0(1)$ best-fit value becomes almost identical. This makes one inclined to think that Belle binned data is more correlated than is assumed.

We note that across all the cases listed in tables 4.2 and 4.4, $R_2(1)$ can be fitted with a small error and has large deviations from the value obtained from the analysis of $B \to D^*\ell\nu_\ell$ (eq. (1.37)). As the treatment of uncertainties in 'Fit-1' and 'Fit-2' are vastly different, we can conclude that this large deviation is not dependent on the fitting procedure, rather a consequence of the data-distribution. All other parameters are extracted with relatively larger errors and are consistent with the fit results obtained by HFAG within 68% or 90% confidence levels (C.L.).

The consequence of these results are reflected in the q^2 dependences of the various form-factors, as shown in figures 4.2 and 4.3. In these figures we have compared the q^2-distribution of the form-factors obtained from our fit results with those obtained using the values given in and around Eq.(1.37). As there is some agreement between the ρ_D^2 fitted from $B \to D\tau\nu_\tau$ and $B \to D\ell\nu_\ell$, the q^2-distributions of $V_1(q^2)$ and $S_1(q^2)$, shown in figs. 4.2a and 4.2b respectively, do not show any considerable deviation. In the analysis of $R(D^*)$, $V(q^2)$ depends on $R_1(1)$ and $\rho_{D^*}^2$, its q^2-distribution has large error and is consistent with those fitted from $B \to D^*\ell\nu_\ell$. $A_1(q^2)$ depends on $\rho_{D^*}^2$ and its q^2-distribution does not show any considerable deviation from that obtained from $B \to D^*\ell\nu_\ell$ fit. As q^2-distributions of both these form-factors obtained from our analysis have large errors, at the moment it is hard to conclude anything and we have to wait for more precise data. On the other hand, among the form-factors associated with $B \to D^*\tau\nu_\tau$, $A_2(q^2)$ depend on $R_2(1)$ and hence it shows large deviation (in all the q^2 regions) from the analysis of $B \to D^*\ell\nu_\ell$ decay. If we assume that the $B \to D^{(*)}\ell\nu_\ell$ decays are free from any kind of NP effects, which may be a natural assumption, then our results allow the possibility of a new contribution beyond the SM in $B \to D^*\tau\nu_\tau$ decay. In particular, it could be a beyond-the-SM (BSM) contribution from a pseudo-vector or a pseudo-tensor [1] current.

---

[1] The pseudo-scalar and pseudo-tensor currents are related to the pseudo-vector currents following the equation of motions, $i\partial_\mu(\bar{c}\gamma^\mu\gamma^5 b) = -(m_b + m_c)\bar{c}\gamma^5 b$ and $\partial_\mu(\bar{c}\sigma^{\mu\nu}\gamma^5 b) = (m_b - m_c)\bar{c}\gamma^\nu\gamma^5 b - (i\partial^\nu\bar{c})\gamma^5 b + \bar{c}\gamma^5(i\partial^\nu b)$, respectively. Hence, the form-factors associated with the pseudo-scalar and pseudo-tensor are

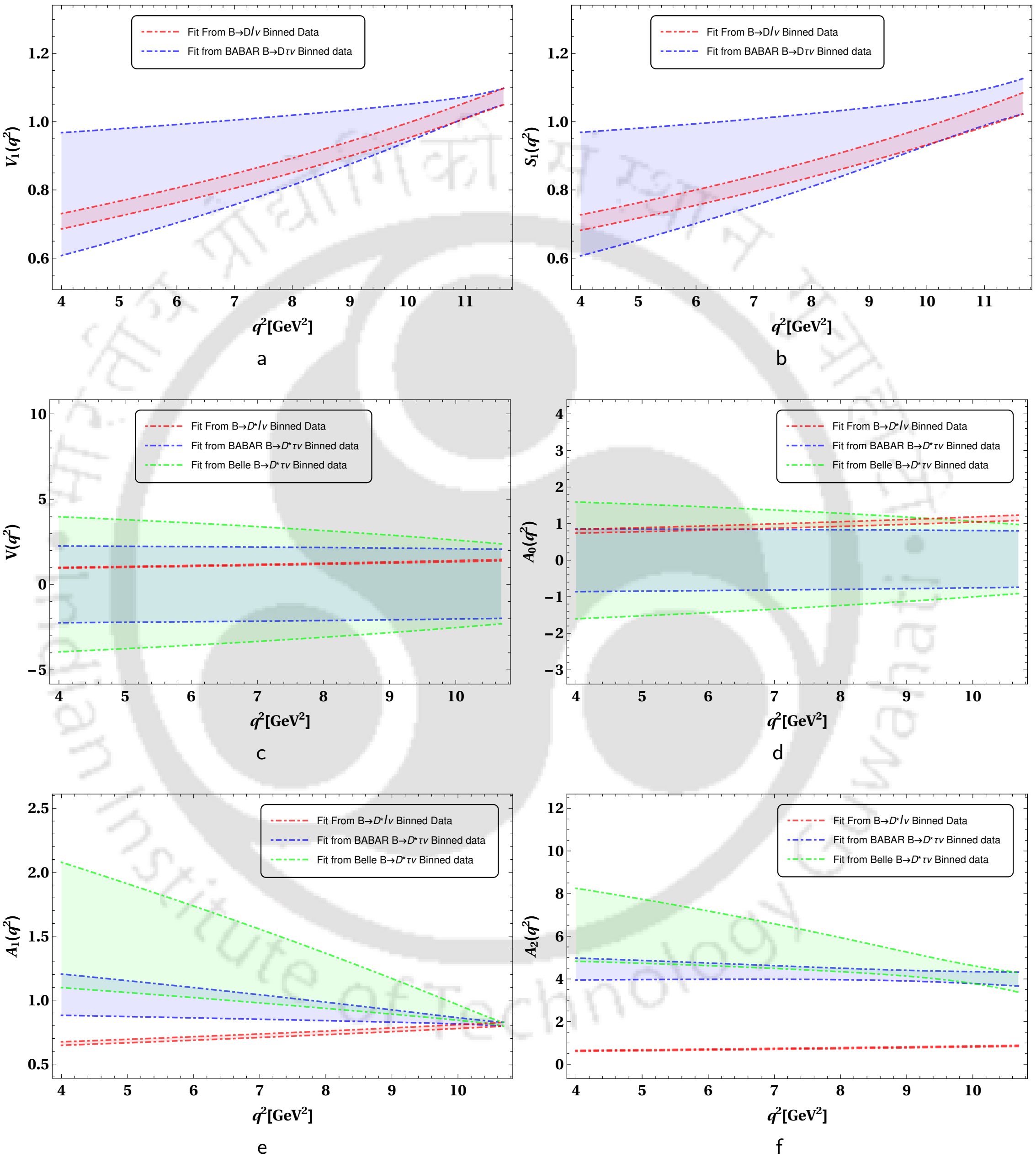

a b

c d

e f

Fig. 4.3 Similar figures of q^2 dependence of form-factors as figure 4.2. These are obtained from ‘Fit-2’.

On a similar note, we can comment that the SM contributions in $B \to D\tau\nu_\tau$ can explain the observed data.

4.3 New Physics Analysis

We follow a model independent approach in search of the type of NP interactions that can best explain the present data on $B \to D^{(*)}\tau\nu_\tau$. Using the q^2 distribution of the differential decay rate of these channels (Eq.(1.21) and Eq.(1.22)) derived from the most general effective hamiltonian with all possible four-fermion operators in the lowest dimension (eq.1.19), we perform the model-selection analysis following the methodology described in Sec. 2.5.2

4.3.1 Methodology

We know that the yield in each bin depends on the probability density functions (PDFs) of different (56 in case of BABAR) signal and background sources. Considering any NP contribution changes these PDFs and they in turn change the two dimensional $m^2_{miss} - |\mathbf{p}^*_l|$ distributions. This change is reflected in the q^2-distribution as well, because of the following relation: $m^2_{miss} = (q - p_l)^2$. A complete and simultaneous fit to all PDFs can only be done for each specific NP model separately and the dependence of the shape and normalization of the PDFs on the NP parameters should be extracted rigorously using raw experimental data. Without the aid of simulation, we do not attempt to do such an analysis. Instead, we use the background subtracted and normalized binned data for q^2 and p_{D^*}-distributions as depicted in Fig.s 4.1a, 4.1b and 4.1c to perform a phenomenological analysis in a model independent way. Such an assumption can become a source of systematic errors in our analysis and the way we have dealt with that is discussed in section 4.3.1.1.

In addition to the binned data from BABAR and Belle, we also have the total $R(D^{(*)})$ data from various experiments (see table 4.1). Keeping in mind that the binned data is going to dominate the fit results, we take different combinations of these separate data points and do the whole analysis separately for them.

---

related to $A_0(q^2)$ and/or $A_2(q^2)$. Therefore, a large deviation in $A_2(q^2)$ can also be compensated by adding pseudo-tensor current contributions, proportional to these form-factors, in the decay width.

Input	Value
Δ	1 ± 1 [63]
ρ_D^2	1.186 ± 0.054 [72]
$\rho_{D^*}^2$	1.207 ± 0.026 [72]
$R_1(1)$	1.406 ± 0.033 [72]
$R_2(1)$	0.853 ± 0.020 [72]
$R_0(1)$	1.14 ± 0.07 [160]
$V_1(1)$	1.053 ± 0.008 [71]
$h_{A_1}(1)$	0.906 ± 0.013 [76]
m_{B_0}	5.280 ± 0.0003
m_{D_0}	1.86484 ± 0.00005 [161]
m_b	4.18 ± 0.03 [161]
m_c	1.275 ± 0.025 [161]
m_τ	1.77682 ± 0.00012 [161]

TABLE 4.6: Inputs used in the fitting of new Wilson coefficients. All Masses are in GeV. Correlations between a few form-factor parameters are listed in Eq. (1.37).

At the beginning of our analysis, we have defined the most general scenario with contributions from all possible dimension 6 effective operators present simultaneously (with 10 parameters i.e. real and imaginary parts of all C_W^ls) as the global scenario. We have defined various sub-scenarios as different possible combinations of those operators. Including the global scenario, there are in total 31 such scenarios, which we are going to call "cases" from here onwards.

One of the main motivations of this study is to do a multi-scenario analysis on the experimentally available binned data, to obtain a data-based selection of a 'best' case and ranking and weighting of the remaining cases in the predefined set of 31. To that goal, we have made use of information-theoretic approaches, especially of AIC$_c$ in the analysis of empirical data. Such procedures lead to more robust inferences in simultaneous comparative analysis of multiple competing scenarios. Traditional statistical inference(e.g. confidence levels, errors on fit parameters, bias etc.) can then be obtained based on the selected best models.

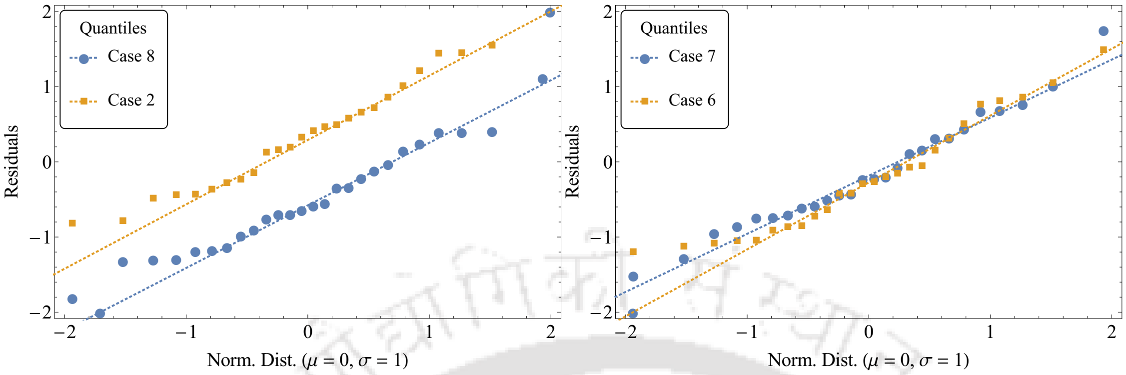

Fig. 4.4 Q-Q Plot of the residuals of the best fits. Each plot compares the quantiles of the distribution of the residuals with a Gaussian with $\mu = 0$ and $\sigma^2 = 1$. The closer the distribution o the points are to the corresponding dotted lines, the better they fit to the Gaussian. Here we show the best NP cases for data-set '3' from table 4.7

4.3.1.1 Numerical Multi-parameter Optimization

To compare the latest BABAR and Belle binned data with a specific model, we devise a χ^2 defined as:

$$\chi^2_{NP} = \sum_{i,j=1}^{n_b} \left(R_i^{exp} - R_i^{th}\right) \left(V^{exp} + V^{th}\right)^{-1}_{ij} \left(R_j^{exp} - R_j^{th}\right) , \tag{4.4}$$

where R^{th}_{bin} and R^{exp}_{bin} are defined in eq.s (1.39) and (4.3). i and j vary over the number of bins (n_b) taken into account in the analysis. For the calculation of R^{th}_{bin}, central values of HQET hadronic form-factors and the quark masses are used (listed in table 4.6). The standard bin-width for the BABAR analysis is 0.5(GeV$^2/c^4$) and due to this the last bin exceeds the allowed phase space($q^2_{max} = (m_B - m_{D^{(*)}})^2$) in both channels. Instead of changing the bin width for those last bins, we drop these bins from our analysis. We follow this same philosophy for Belle bins too. V^{th}_{ij} and V^{exp}_{ij} are the theoretical and experimental covariance matrices respectively. For the analysis of any specific NP model, the uncertainties of the HQET hadronic form-factors and the quark masses(table 4.6) are taken into account in the calculation of V^{th}_{ij}.

To calculate the errors δR^{exp}_{bin}, we use eq.(4.3) according to the case and propagate the errors listed in table 4.1. Following the reasoning stated in section 4.2.2, we break the

Experiment	Dataset Index.	Observables	Cases	χ^2_{min}	$d.o.f$	Parameters	Akaike Wgt.s (w_i)	Normality (S-W)	χ^2 (SM)
BABAR	1	$R(D)_{bin}$	5	7.41	12	C_T	0.26	0.38	10.31
			1	7.79	12	C_{V_1}	0.22	0.29	
			2	7.79	12	C_{V_2}	0.22	0.29	
			3	9.17	12	C_{S_1}	0.11	0.18	
			4	9.17	12	C_{S_2}	0.11	0.18	
	2	$R(D^*)_{bin}$	1	6.3	10	C_{V_1}	0.56	0.11	79.85
			2	7.18	10	C_{V_2}	0.36	0.12	
	3	Combined	8	13.01	22	C_{V_2}, C_{S_2}	0.32	0.86	90.16
			2	19.12	24	C_{V_2}	0.22	0.59	
			7	14.23	22	C_{V_2}, C_{S_1}	0.17	0.79	
			6	14.61	22	C_{V_1}, C_{V_2}	0.14	0.19	
Belle(2016)	4	$R(D^*)_{bin}$	2	9.07	15	C_{V_2}	0.47	0.95	26.20
			1	9.43	15	C_{V_1}	0.39	1.00	
BABAR+ Belle(2016)	5	Combined	8	22.59	39	C_{V_2}, C_{S_2}	0.31	0.95	116.36
			2	28.33	41	C_{V_2}	0.19	0.94	
			7	23.69	39	C_{V_2}, C_{S_1}	0.18	0.89	
			6	24.16	39	C_{V_1}, C_{V_2}	0.14	0.69	
BABAR+ Belle(2015)+ LHCb+ Belle(Latest)	6	Combined	2	48.54	28	C_{V_2}	0.52	0.02	96.68
			8	45.71	26	C_{V_2}, C_{S_2}	0.16	0.01	
			7	46.87	26	C_{V_2}, C_{S_1}	0.09	0.02	
			6	47.24	26	C_{V_1}, C_{V_2}	0.08	0.04	
Belle(2016)+ Belle(2015)+ LHCb+ Belle New	7	Combined	2	28.81	19	C_{V_2}	0.34	0.64	32.72
			1	30.81	19	C_{V_1}	0.13	0.77	
			4	31.29	19	C_{S_2}	0.1	0.83	
			3	31.48	19	C_{S_1}	0.09	0.91	
			5	31.52	19	C_T	0.09	0.82	

TABLE 4.7: The best selected scearios for "Fit-1" (section 4.3.2.1). The cases listed in order in the fourth column for each dataset have passed through the selection criteria $0 \leq \Delta_i^{AIC} \leq 4$, where $\Delta_1^{AIC} = 0$ in each dataset. Note that the case-index values represent a specific set of parameters and each parameter listed here is considered to be complex, so the number of parameters is actually double. w_i in the eighth column is defined in eq.(2.18). The next column lists the results of the S-W normality test for the assessment of goodness-of-fit. The last column lists the χ^2 value corresponding to the SM for each dataset. Note that AIC$_c$ value for SM is same as the χ^2 as no. of fit parameters $K = 0$ for SM.

NP analysis in two parts: 'Fit-1' and 'Fit-2'. In addition to V_{ij}^{th}, here we treat the V_{ij}^{exp} exactly as the V_{ij} in section 4.2.2.

We define the χ^2 statistic for each of the 31 cases, a function of the NP Wilson coefficients. The definition and usage of the observables closely follow the fitting process in section 4.2.2. Here, we take the existing world-averages of the parameters of the form-factors [72]. If we include all the NP interactions, we have total 10 unknown NP parameters and 26 observables for BABAR (14 bins for $B \to D\tau\nu$ and 12 bins for $B \to D^*\tau\nu$) and 17 observables for Belle. We then minimize the χ^2 for different cases and different set of observables. Though we have varied the process for various global optimization methods to optimize the minimization, due to the presence of large uncertainties, this is not important for the present analysis. To glean any information of goodness-of-fit from χ^2_{min}, we need to know the degrees of freedom ($d.o.f = N_{Obs} - N_{Params}$). A reduced statistic $\chi^2_{red} = \chi^2_{min}/d.o.f$ can thus be defined.

In many cases in our optimization problem, the minimum is not an isolated single point, rather a contour in the parametric dimensions. For these cases, Hessian in not positive definite and the errors thus obtained are meaningless. In those cases, the 1σ uncertainties have to found from the contours in the parameter space and we have done that for all cases with $2-3$ parameters. As contours are impossible to draw when number of parameters > 3, we have devised a numerical method to obtain the range of a parameter. In this method, we sequentially minimize or maximize each parameter by scanning along the enclosing 1σ χ^2_{NP} hyper-contour-surface (the method can be extended to any number of $n\sigma$ contours). These values give us the range of each parameter while taking their correlation into account all along. These errors, for obvious reasons, are asymmetric. We have also systematically found these uncertainties for all cases. We will in general quote them in our results.

In our present analysis, after optimizing the χ^2_{NP} for all 31 cases, we make use of Δ_i^{AIC} and w_i to find the 'best' set of cases, which are more favorable compared to others, and do further analysis on them. After selecting a class of models describing the data with optimum bias and variance with AIC$_c$, we check the significance of them to find most suited model to describe the data.

4.3.2 Results

4.3.2.1 Fit-1

In this fit, as mentioned in the previous section, we do not consider the systematic errors or their correlations. The best probable NP cases (scenarios), which are obtained after minimizing the χ^2_{NP} and using w_i (eq. (2.18)), are listed in table 4.7. Then using the formalism defined in section 2.4, we find the distribution of the residuals for all those fits and we check whether that distribution is accordant with a normal distribution with mean 0 and variance 1. As was mentioned and justified in section 2.4, we use Shapiro-Wilk's normality-test for this. Also, in order to check the normality of the residuals,

DataSet Ind.	Cases	Param.s	B.F. Val	± Err.
1	5	$Re(C_T)$	0.27	0.10
		$Im(C_T)$	0.00	1.06
	3	$Re(C_{S_1})$	0.09	0.06
		$Im(C_{S_1})$	0.00	0.30
	4	$Re(C_{S_2})$	0.09	0.06
		$Im(C_{S_2})$	0.00	0.30
2	2	$Re(C_{V_2})$	0.27	0.03
		$Im(C_{V_2})$	0.00	0.40
3	8	$Re(C_{V_2})$	0.34	0.12
		$Im(C_{V_2})$	-0.33	0.20
		$Re(C_{S_2})$	-0.52	0.43
		$Im(C_{S_2})$	-0.16	0.21
	2	$Re(C_{V_2})$	0.23	0.02
		$Im(C_{V_2})$	0.00	0.09
	7	$Re(C_{V_2})$	0.29	0.03
		$Im(C_{V_2})$	0.00	0.54
		$Re(C_{S_1})$	-0.23	0.09
		$Im(C_{S_1})$	0.00	0.48
4	2	$Re(C_{V_2})$	0.58	0.69
		$Im(C_{V_2})$	-0.59	0.37
5	8	$Re(C_{V_2})$	0.34	0.12
		$Im(C_{V_2})$	-0.35	0.21
		$Re(C_{S_2})$	-0.51	0.46
		$Im(C_{S_2})$	-0.14	0.22
	2	$Re(C_{V_2})$	0.23	0.02
		$Im(C_{V_2})$	0.00	0.09
	7	$Re(C_{V_2})$	0.28	0.03
		$Im(C_{V_2})$	0.00	0.70
		$Re(C_{S_1})$	-0.22	0.08
		$Im(C_{S_1})$	0.00	0.55
7	2	$Re(C_{V_2})$	0.10	0.05
		$Im(C_{V_2})$	-0.23	0.17
	4	$Re(C_{S_2})$	-0.93	0.73
		$Im(C_{S_2})$	-0.69	0.32
	3	$Re(C_{S_1})$	0.14	0.08
		$Im(C_{S_1})$	0.00	0.43
	5	$Re(C_T)$	0.04	0.03
		$Im(C_T)$	0.00	0.03

TABLE 4.8: Best-fit values and Gaussian errors of all parameters for the selected 'best' cases for 'Fit-1', listed in table 4.7. Some cases are omitted due to the reason explained in section 2.4 and corresponding plots are tabulated in fig. 4.5.

Dataset Index.	Cases with $0 < \Delta\mathrm{AIC}_c < 4$	Cases with $0 < \Delta\mathrm{BIC} < 4$
1	C_T C_{V_1} C_{V_2} C_{S_1} C_{S_2}	C_T C_{V_1} C_{V_2} C_{S_1} C_{S_2}
2	C_{V_1} C_{V_2}	C_{V_1} C_{V_2}
3	C_{V_2} C_{V_2}, C_{S_2} C_{V_1} C_{V_2}, C_{S_1}	C_{V_2} C_{V_2}, C_{S_2} C_{V_1} –
4	C_{V_2} C_{V_1}	C_{V_2} C_{V_1}
5	C_{V_2}, C_{S_2} C_{V_2}, C_{S_1} C_{V_1}, C_{V_2} C_{V_2} C_{V_1}	C_{V_2}, C_{S_2} C_{V_2} C_{V_1} C_{V_2}, C_{S_1} C_{V_1}, C_{V_2}
6	C_{V_2} C_{V_2}, C_{S_2} C_{V_2}, C_{S_1}	C_{V_2} C_{V_2}, C_{S_2} –
7	C_{S_1} C_T C_{S_2} C_{V_2} C_{V_1}	C_{S_1} C_T C_{S_2} C_{V_2} C_{V_1}

TABLE 4.9: The best selected scenarios for "Fit-2" (section 4.3.2.2). Here we compare the performance of AIC_c with BIC in model selection.

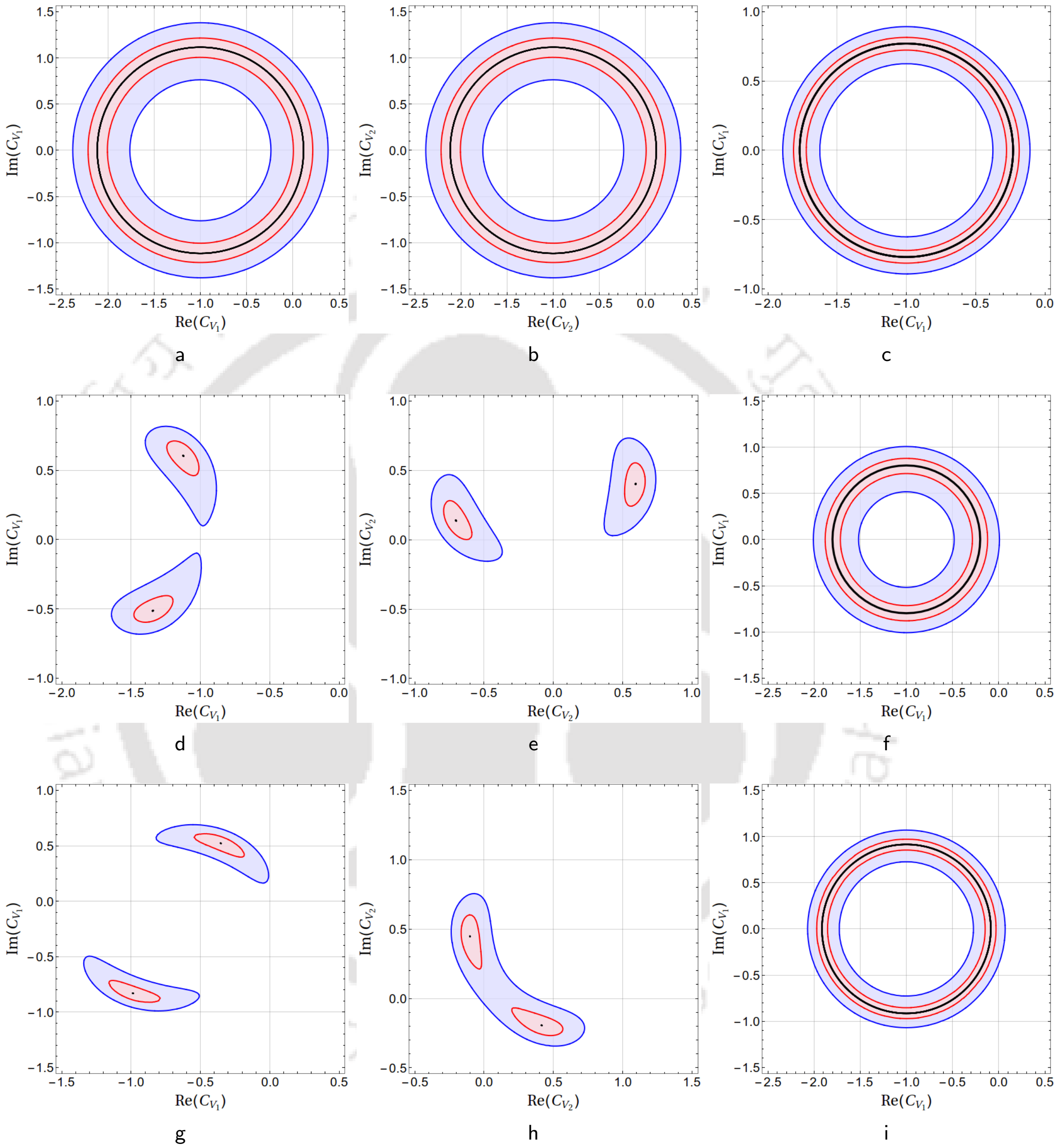

Fig. 4.5 The ‘cases’ for different datasets listed in table 4.7, which pass the goodness-of-fit hypothesis tests but could not be listed in table 4.8 as for these cases, the minimum, instead of being an isolated point, is actually a contour in the parameter-space. Though this is true for all plots listed here, some cases have four parameters and we are only able to show the two-parameter cross-sections of these.(e.g. plots 4.5d and 4.5e are actually cross-sections of a single four-dimensional plot. Same is true for 4.5g and 4.5h).

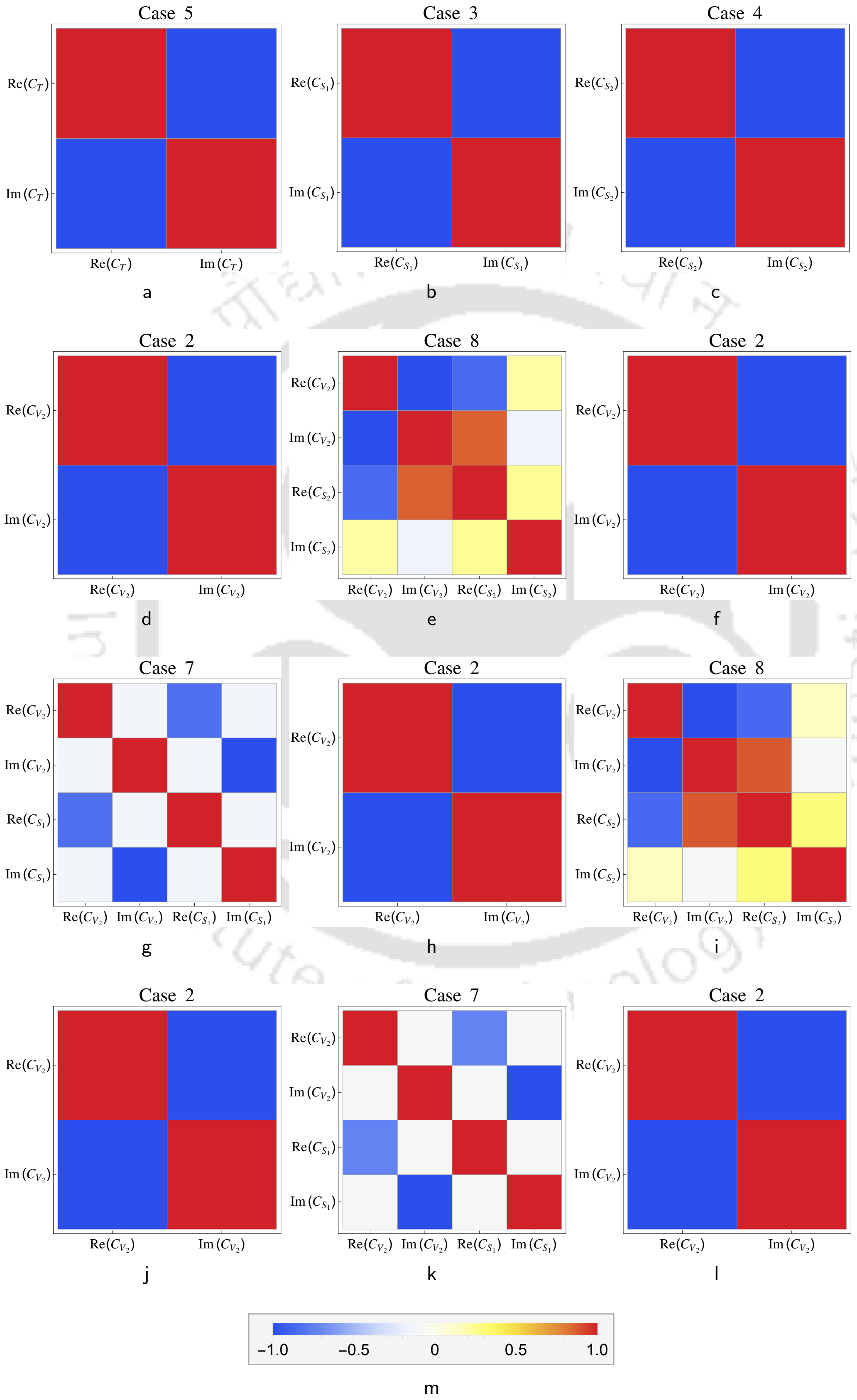

Fig. 4.6 Array-plots showcasing the correlations between the fitted parameters of separate ‘cases’ for different datasets listed in table 4.8. The color-coding is explained in the horizontal legend. As can be seen, for the cases with only two independent parameters, the parameters are strongly (negatively) correlated, compared to other cases, as expected.

Experiment	Dataset Index.	Observables	Cases	χ^2_{min}	*d.o.f*	Parameters	Akaike Wgt.s (w_i)	Normality (S-W)	χ^2 (SM)
BABAR	1	$R(D)_{bin}$	5	7.28	12	C_T	0.25	0.54	8.63
			1	7.65	12	C_{V_1}	0.20	0.38	
			2	7.65	12	C_{V_2}	0.20	0.38	
			3	8.56	12	C_{S_1}	0.13	0.15	
			4	8.56	12	C_{S_2}	0.13	0.15	
	2	$R(D^*)_{bin}$	1	5.71	10	C_{V_1}	0.57	0.17	20.20
			2	6.75	10	C_{V_2}	0.34	0.09	
	3	Combined	2	15.68	24	C_{V_2}	0.48	0.53	70.44
			8	12.32	22	C_{V_2}, C_{S_2}	0.18	0.73	
			1	19.03	24	C_{V_1}	0.09	0.3	
			7	14.13	22	C_{V_2}, C_{S_1}	0.07	0.81	
Belle(2016)	4	$R(D^*)_{bin}$	2	6.44	15	C_{V_2}	0.47	0.74	17.76
			1	6.92	15	C_{V_1}	0.37	0.86	
BABAR+ Belle(2016)	5	Combined	8	19.11	39	C_{V_2}, C_{S_2}	0.41	0.72	87.91
			7	21.54	39	C_{V_2}, C_{S_1}	0.12	0.72	
			6	21.75	39	C_{V_1}, C_{V_2}	0.11	0.12	
			2	27.35	41	C_{V_2}	0.07	0.96	
			1	27.42	41	C_{V_1}	0.07	0.65	
BABAR+ Belle(2015)+ LHCb+ Belle(Latest)	6	Combined	2	47.88	28	C_{V_2}	0.49	0.03	85.47
			8	44.97	26	C_{V_2}, C_{S_2}	0.16	0.01	
			7	46.47	26	C_{V_2}, C_{S_1}	0.08	0.01	
Belle(2016)+ Belle(2015)+ LHCb+ Belle(Latest)	7	Combined	3	27.68	19	C_{S_1}	0.21	0.56	29.85
			5	27.83	19	C_T	0.19	0.44	
			4	27.93	19	C_{S_2}	0.18	0.84	
			2	28.00	19	C_{V_2}	0.18	0.86	
			1	29.82	19	C_{V_1}	0.07	0.75	

TABLE 4.10: The best selected scearios for "Fit-2" (section 4.3.2.2). For clarification of columns, please see the caption of table 4.7

we use the graphical method known as quantile-quantile ($Q-Q$) plot. In general, the $Q-Q$ plots are used to compare two probability ditributions. In fig. 4.4, we show the residual-distributions while comparing them with the reference Gaussian ($\mu = 0$, $\sigma = 1$). The p-value obtained in the normality-test quantifies the probability of H_0 being true. In table 4.7, the last column lists the p-values for the performed S-W test.

Only those NP scenarios, which pass the normality test, are listed in table 4.8 with the best-fit values and 1σ uncertainties of their parameters. Other than that, some cases are not shown in the Table, where the minimum, instead of being an isolated point, is actually a contour in the parameter-space. For such cases, we have plotted the best-fit contours in the parameter-space. These are shown in fig. 4.5. We have prepared these plots in terms of the goodness-of-fit contours for joint estimation of multiple NP parameters at a time. 1σ and 4σ contours that are equivalent to p-values of 0.3173 and 0.0001, correspond to confidence levels of 68.27% and 99.99%, respectively.

DataSet Ind.	Cases	Param.s	B.F. Val	± Err.
1	5	$Re(C_T)$	0.36	0.19
		$Im(C_T)$	0.00	1.14
	3	$Re(C_{S_1})$	-0.05	0.16
		$Im(C_{S_1})$	0.00	0.28
	4	$Re(C_{S_2})$	-0.05	0.16
		$Im(C_{S_2})$	0.00	0.28
2	2	$Re(C_{V_2})$	0.34	0.08
		$Im(C_{V_2})$	0.00	0.38
3	2	$Re(C_{V_2})$	0.22	0.02
		$Im(C_{V_2})$	0.00	0.20
	8	$Re(C_{V_2})$	0.31	0.11
		$Im(C_{V_2})$	0.04	2.16
		$Re(C_{S_2})$	-0.52	0.37
		$Im(C_{S_2})$	0.004	0.46
	7	$Re(C_{V_2})$	0.31	0.06
		$Im(C_{V_2})$	0.00	0.36
		$Re(C_{S_1})$	-0.31	0.21
		$Im(C_{S_1})$	0.00	0.40
4	2	$Re(C_{V_2})$	0.67	0.69
		$Im(C_{V_2})$	-0.36	0.47
5	8	$Re(C_{V_2})$	0.34	0.04
		$Im(C_{V_2})$	0.00	0.62
		$Re(C_{S_2})$	-0.61	0.22
		$Im(C_{S_2})$	0.00	0.34
	7	$Re(C_{V_2})$	0.37	0.06
		$Im(C_{V_2})$	0.00	0.23
		$Re(C_{S_1})$	-0.51	0.20
		$Im(C_{S_1})$	0.00	0.30
	2	$Re(C_{V_2})$	0.22	0.02
		$Im(C_{V_2})$	0.00	0.11
7	3	$Re(C_{S_1})$	-0.45	0.47
		$Im(C_{S_1})$	0.80	0.15
	5	$Re(C_T)$	0.09	0.03
		$Im(C_T)$	0.00	0.06
	4	$Re(C_{S_2})$	0.18	0.08
		$Im(C_{S_2})$	0.00	0.87
	2	$Re(C_{V_2})$	0.09	0.05
		$Im(C_{V_2})$	0.39	0.14

TABLE 4.11: Best-fit values and Gaussian errors of all parameters for the selected ‘best’ cases for ‘Fit-2’, listed in table 4.10. Some cases are omitted due to the reason explained in section 2.4

For our purpose, each confidence interval corresponds to a particular value of $X = \Delta\chi^2$ (i.e. $\chi^2 - \chi^2_{min}$) for a particular model with $d.o.f = N_{params}$, where the SM is considered to be the model with no free parameters. For cases up-to 3 parameters, errors on parameters can be estimated from the edges of the 2 or 3 dimensional contours as they properly reflect the correlation between the involved parameters.

From Table 4.7, we note that all types of new interactions considered in our analysis can individually explain the data on $R(D)_{bin}$ published by BABAR. However, when it comes to the q^2-distribution of decay rate of $B \to D^*\tau\nu_\tau$, both BABAR and Belle data independently allow a contribution from a new left or right-handed vector current effective operator (cases 1 and 2) as plausible explanation. Moreover, when the data (q^2-bins) from both the BABAR and Belle are combined, the most likely scenarios are the cases with new right handed vector current, either alone or along with other new right or left handed scalar current effective operators. In addition to binned data, we have done the analysis by taking into account the Belle and LHCb measurements of the q^2 integrated $R(D^{(*)})$ (see Table 4.1 for numerical values). The outcome of these analyses are shown for datasets 6 and 7 in the table 4.7. No scenario passes the normality test for dataset-6. In dataset-7, the most likely scenarios are the new left or right handed scalar or vector current operators, though, across all the cases the reduced χ^2s are > 1.

Accross all the datasets discussed above, we note that wherever measurements of $R(D)$s are included in our fit the effective operators associated with the scalar current become relevant, either alone (less preferable) or along with the right handed vector current operator. It could be considered as an indication that current data on $R(D)$ still allow a scalar current contribution as a possible explanation of the observed deviations. Also, across all the scenarios which qualify our predefined test criteria, a common NP explanation is case 2, i.e the presence of a new $(V + A)$ type interaction. Here, we can not distinguish whether the new contribution is a vector or a pseudo-vector or both. However, if we combine the information obtained from the parametric fit of the form factors, it won't be wrong to conclude that the most favorable solution of the present data on the decay $B \to D^*\tau\nu_\tau$ could be obtained from the presence of a pseudo-vector current.

4.3.2.2 Fit-2

In this fit, as mentioned earlier, we consider the systematic error-sizes to be same as the statistical ones and assume 100% correlation among them. The best cases according to their Akaike weights are listed in table 4.10. The results are obtained and analyzed in the same manner as for 'Fit-1'. Here too, no fit-result for data-set '6' passes the normality criteria. Hence we drop that set from further analysis. The outcome of the analyses of the rest of the datasets are similar to the ones obtained in 'Fit-1', i.e both the fits have almost identical conclusions. The only exception is that, here, the role of left handed vector current becoms equally important as the right handed vector current, i.e apart from a new $(V + A)$ type interaction, the presence of a new $(V - A)$ type interaction can also be considered as common NP explanation of the current data. The best fit values of the fitted parameters along with the corresponding errors are shown in table 4.11.

4.4 Summary

We look for possible new physics effects in the decays $B \to D^{(*)}\tau\nu_\tau$ in the light of the recently available data from Belle, BABAR and LHCb. At first, the form-factors, relevant in these decays, are fitted assuming the absence of any contribution coming from operators other than the SM. The fitted results are then compared with those obtained by HFAG from a fitting to the available data on $B \to D^{(*)}\ell\nu_\ell$. We note that the fit results of the parameter $R_2(1)$ largely disagree with each other, while the rest are more or less consistent with each other within errors. The effects are prominent in all the regions of the q^2 distribution of the form-factor $A_2(q^2)$, which is associated with a pseudo-vector current. Therefore, assuming the decays $B \to D^{(*)}\ell\nu_\ell$ are free from any new physics effects, such a difference in the q^2 distribution of A_2 (obtained from $B \to D^*\tau\nu_\tau$ and $B \to D^*\ell\nu_\ell$) can be compensated by adding a contribution from new pseudo vector and/or pseudo tensor currents.

In the next part of our analysis, we consider the new physics contributions in the decays $B \to D^{(*)}\tau\nu_\tau$ which come from new vector, scalar or tensor type operators. In this case, we take the relevant form-factors as obtained using the fit results by HFAG. We define different possible NP scenarios which are obtained after combining contributions from the new operators in many different ways. Our goal is to select the best possible

NP scenarios (new interactions) that can accommodate all the available data. In doing so, we use the AIC$_c$ in the analysis of the empirical data. Such procedures lead to more robust inferences in simultaneous comparative analysis of multiple competing scenarios. In order to check whether all the NP scenarios that are coming out of AIC$_c$ test can fit the data well or not, we have done Shapiro-Wilk's normality-test for each selected model. For a comparative study, we have also analyzed the data for selecting the best model using Schwarz-Bayesian Criterion (BIC). For our different datasets the best selected models are identical in both the selection criteria.

Our analysis of the available data on $R(D^*)$ from BABAR, Belle, and LHCb shows that the most plausible explanation of the data can be obtained from the presence of new effective oparators with left or right handed charged vector current. In addition, if we include $R(D)$ in our fit, apart from the vector currents the contributions from charged scalar currents might become relevant, either alone (though less preferable) or along with right handed vector current operators.

Overall, our analysis of $B \to D^*\tau\nu_\tau$ shows that it is the contribution from a left or right-handed charged vector current effective operator, that, as well as accommodating all the available data, passes all the selection criteria for being the best possible NP scenario.

Here, we would like to point out that we have made use of the available data on the q^2 (bins) distributions of the decays $B \to D^{(*)}\tau\nu_\tau$, which have large errors. This, in turn, gives our fitted results large errors. Once the more precise data on the q^2 bins are made available, one may and should repeat the analysis to check sustainability of the above conclusions.

Chapter 5

$b \to c\tau\nu_\tau$ Decays: A Catalogue to Compare, Constrain, and Correlate New Physics Effects

5.1 Introduction

In this chapter, we have done a model independent analysis of the NP affecting several $b \to c\tau\nu_\tau$ decay modes. In this analysis along with the available data on $R(D^{(*)})$, we have included the data on $P_\tau(D^*)$ and $R_{J/\psi}$ which are defined in Eq.(1.40) and Eq.(1.44). Also, we have used the lifetime of B_c [116, 117] meson as constrain. In addition, we have focused on baryonic $\Lambda_b \to \Lambda_c\tau\nu_\tau$ decays and the inclusive $B \to X_c\tau\nu_\tau$ decay which are potentially sensitive to the new interactions and the NP affecting $\mathcal{R}_{D^{(*)}}$ and $\mathcal{R}_{J/\psi}$.

The operator basis is exactly the same as that given in Eq.(1.20), which consists of scalar, vector, and tensor type of operators. We have considered all possible combinations of these operators and categorised them as independent models. There are several of them capable of describing the observed data and one is thus confronted with the problem of model selection. We use the Akaike information criterion (AIC) to find out the best possible model(s) for the existing data. A model selection criterion is a formula that allows one to compare models; for details, see section 2.5.2. Alternative related approaches to the model selection are the bootstrap method and cross-validation. Cross-validation works poorly with small sample sizes, as it is in our case, and parametric bootstrap variants of AIC have recently been proposed [171], which we have not used in the present analysis. Using the AIC, we have first selected the models best suited for explaining the existing data. Also in the selected cases, we have found the best fitted values of the model parameters. With these best fitted values, we have predicted the values of various observables associated with the above mentioned decay modes. The correlation studies of the various observables associated with these channels are expected to be an important probe for an indirect detection of NP. On the other hand, the precise measurements of some of these observables will be useful to constrain the new physics parameters associated with a model. This motivates us to predict the values of all the relevant observables for some specific model, which can then be further checked for consistency with the future measurements. Furthermore, we have studied the graphical correlations among the observables, which are found to be useful in discriminating various new physics scenarios.

Before entering into the new physics analysis, we have also predicted the SM values of the asymmetric and angular observables in $B \to D^{(*)}\tau\nu_\tau$ decays, using the results of the new up-to-date analysis in $B \to D^{(*)}\ell\nu_\ell$. Previously, the prediction of $R(D)$ includes the up-to-date lattice inputs, whereas the prediction of $R(D^*)$ relies heavily on HQET. Also, the current lattice results suggest that the HQET values of form-factors at zero recoil are not in complete agreement with those from lattice [24, 74]. With the inclusion of lattice inputs[25, 26, 69] and using the Caprini-Lellouch-Neubert (CLN) [68] parametrisation of the form factors, the SM prediction of $R(D)$ and $R(D^*)$ is given by

$$R(D) = 0.299 \pm 0.003, \quad R(D^*) = 0.259 \pm 0.006. \tag{5.1}$$

On the experimental side, the current world averages are given by [163]

$$R(D) = 0.407 \pm 0.046, \quad R(D^*) = 0.304 \pm 0.015\,. \tag{5.2}$$

We note that in both observables, the deviations are a little less then 2.6σ. Though these deviations can be explained by a variety of new physics models, we will follow a model independent analysis, like the one done in ref. [159]. The other model independent analyses, which are relatively new, can be seen in refs. [117, 127, 164–170]. Furthermore, We have revisited the SM prediction of the inclusive ratio $\mathcal{R}_{X_c}$, and have given its values in two different schemes of the charm quark mass.

5.2 Observables in $b \to c\tau\nu_\tau$ decays : Standard Model revisited

In this section we have revisited the standard model predictions of different observables coming from the available decay channels in $b \to c\tau\nu_\tau$ transition. Detailed discussion on all the observables considered in this analysis is given in sec.1.2.2 of chapter 1.

5.2.1 Exclusive Decay Channels :

As far as the exclusive decay channels are concerned, we have considered several semileptonic ($B \to D^{(*)}\tau\nu_\tau$, $B_c \to J/\psi\tau\nu_\tau$ and $\Lambda_b \to \Lambda_c\tau\nu_\tau$) and leptonic decay modes ($B_c \to \tau\nu_\tau$) in this analysis. In case of $B \to D^{(*)}\tau\nu_\tau$ decays, we have followed the CLN [68] parametrisation of the $B \to D^{(*)}$ form-factors and have used both the fitted and predicted values of these parameters obtained in [26]. On the other hand, as the precise calculations of the form factors are unavailable in $B_c \to J/\psi\ell\nu_\ell$ decay, two different parametrisations namely perturbative QCD (PQCD [77]), and light-front covariant quark model (LFCQ [83]) are considered in this analyis. Choosing different parametrisations results in varying the central value of $\mathcal{R}_{J/\psi}$ within the range 0.25 - 0.29, which is considered theoretical range in recent experimental analyses. Taking the uncertainties from different parametrisations into consideration, we see that the allowed theoretical range of $\mathcal{R}_{J/\psi}$ is actually larger than that. For $\Lambda_b \to \Lambda_c\ell\nu_\ell$ channel, helicity form factors have been calculated using the formula from lattice QCD in the relativistic heavy quark limit [98]

The SM predictions of the observables from all of these exclusive decay modes are listed in table. 5.1.

5.2.2 Inclusive Decay :

The elaborate discussion on the inclusive semileptonic decay of B meson is given in sec.1.2.2.4 of chapter 1. This is the first analysis which includes all the known corrections in the SM for the inclusive observables. For the decay of $B \to X_c\ell\nu_\ell$ where $\ell = \mu, e$, the complete one and two-loop perturbative corrections, along with the $1/m_b^{2,3}$ power

Observable	SM Prediction		Correlation						
$\mathcal{R}_{D^*}$	0.260(6)	[26]	1.	0.118	0.617	0.118	0.604	0.628	-0.118
$\mathcal{R}_D$	0.305(3)			1.	-0.023	1.	0.021	0.007	-1.
$P_\tau(D^*)$	-0.491(25)	New*			1.	-0.023	0.803	0.895	0.023
$P_\tau(D)$	0.3355(4)					1.	0.021	0.007	-1.
$F_L^{D^*}$	0.457(10)						1.	0.921	-0.021
$\mathcal{A}_{FB}^*$	-0.058(14)							1.	-0.007
$\mathcal{A}_{FB}$	0.3586(3)								1.
$\mathcal{R}_{J/\Psi}$ (LFCQ)	0.249(42)	[90]							
$\mathcal{R}_{J/\Psi}$ (PQCD)	0.289(28)	[77]							
$\mathcal{R}_\Lambda^\mu$	0.329(13)	[98]							
$\mathcal{R}_\Lambda^e$	0.328(13)	[98]							
$\mathcal{B}(B_c \to \tau\nu)$	0.0208(18)	(this work)							

TABLE 5.1: SM values of observables obtained and/or used in this chapter, with correlations, wherever relevant. Due to considerable uncertainty and difference in central values, value of $\mathcal{R}_{J/\Psi}$ is quoted for both LFCQ and PQCD parametrizations. They are treated separately throughout the NP analysis as well.
* Based on [26]

corrections have been considered in Eq. (1.52). In case of $B \to X_c\tau\nu_\tau$ decay, upto next-to-next-to-leading order (NNLO) corrections in α_s are incorporated. In this analysis, we have also considered the well known electroweak correction $A_{ew}(= 1.014)$.

Parameters	Value	Correlation						
m_b^{Kin}	4.561(21)	1.	0.608	-0.096	0.132	0.554	-0.170	-0.062
m_c	1.092(20)		1.	-0.022	0.003	-0.032	0.011	0.023
μ_π^2	0.464(67)			1.	0.717	-0.045	0.060	0.158
ρ_D^3	0.175(40)				1.	-0.077	-0.134	0.076
μ_G^2	0.333(61)					1.	-0.042	-0.022
ρ_{LS}^3	-0.146(96)						1.	-0.020
$\mathcal{B}(B \to X_c\ell\nu_\ell)$	10.66(16)%							1.

TABLE 5.2: The correlations between various non-perturbative parameters and the masses. These were all obtained in the analysis of inclusive $B \to X_c\ell\nu_\ell$ decays in [99].

We have given the predictions for the ratio $\mathcal{R}_{X_c}$ instead of $\mathcal{B}(B \to X_c\tau\nu_\tau)$. From the definition of $\mathcal{R}_{X_c}$ (Eq. 1.51) it is clear that this ratio is theoretically very clean, since the errors due to $|V_{cb}|$ and the mass of the b-quark cancel in the ratio. Our predictions for $\mathcal{R}_{X_c}$ in the SM are given in table 5.3. These predictions differ from each other due to the difference in the mass of the charm quark in two different schemes. We note that the central values of the two predictions change by $\approx 4\%$ due to scheme dependence, albeit being consistent within 1σ uncertainties. Also, we have checked our prediction for the $1S$ scheme masses of the b and c quark, and we agree with that given in ref. [152] which is also different from the predictions given in table 5.3 (NLO and $\frac{1}{m_b^2}$). These results are clearly scheme dependent.

In the case of m_c^{kin} (1 GeV), the correlation matrix for the non-perturbative parameters and the masses are given in table 5.2, which are obtained from the analysis of [99]. This is the first analysis which includes all the known corrections in the prediction of R_{X_c}. In ref. [110], the analysis has been done with similar set of inputs, without considering the NNLO corrections. We have checked that our result agrees with them, within the error bar, at the same level of accuracy. The inputs for the analysis with $\overline{m_c}$(3GeV) are taken from table II of ref. [99]. In this scheme, the predictions have larger uncertainties compared to those in the kinetic scheme. This is due to the difference in the correlation matrix of parameters given in table 5.3.

SM predictions for $\mathcal{R}_{X_c}$		
Accuracy in $B \to X_c \tau \nu_\tau$ (at order α_s^n & $\frac{1}{m_b^n}$)	$\overline{m_c}(3\ GeV) = 0.987(13)$ (in GeV)	$m_c^{kin} = 1.091\ (20)$ (in GeV)
LO + NLO + NNLO + $\frac{1}{m_b^2}$	0.238(5)	0.232(4)
LO + NLO + NNLO + $\frac{1}{m_b^2}$ + $\frac{1}{m_b^3}$	0.214(4)	0.209(4)

TABLE 5.3: SM Predictions for $\mathcal{R}_{X_c}$. Other relevant inputs are taken from table 5.2 in the kinetic scheme, while those for the $\overline{MS}$ scheme are taken from table II of ref. [99].

5.3 New Physics Analysis

5.3.1 Numerical Optimization and Model Selection

As mentioned earlier, the goal of this analysis is to perform a model independent multi-scenario analysis with the experimentally available results on the charged current anomalies, in conjunction with other relevant results, to obtain a data-based selection of a ‘best’ scenario and ranking and weighting of the remaining scenarios from a predefined set. If we consider the NP Wilson coefficients occurring in eq. 1.19 to be complex, all possible combinations of the real and imaginary parts of the coefficients (10 parameters in total) should constitute such a predefined set, from which we can choose different scenarios. Scenarios containing only imaginary Wilson coefficients are neglected.

Index	Data Without $\mathcal{R}_{J/\Psi}$					All Data ($\mathcal{R}_{J/\Psi}$ with LFCQ)					All Data ($\mathcal{R}_{J/\Psi}$ with PQCD)				
	χ^2_{min} / DoF	p-val (%)	Param.s	w^{AIC_c}	$B_c \to \tau\nu$	χ^2_{min} / DoF	p-val (%)	Param.s	w^{AIC_c}	$B_c \to \tau\nu$	χ^2_{min} / DoF	p-val (%)	Param.s	w^{AIC_c}	$B_c \to \tau\nu$
1	4.05/8	85.3	$\mathcal{R}e(C_T)$	35.85	✓	7.24/9	61.22	$\mathcal{R}e(C_{V_1})$	25.44	✓	6.46/9	69.34	$\mathcal{R}e(C_{S_2})$	33.37	×
2	4.58/8	80.13	$\mathcal{R}e(C_{V_1})$	20.99	✓	7.28/9	60.78	$\mathcal{R}e(C_{S_2})$	24.39	×	6.68/9	67.01	$\mathcal{R}e(C_{V_1})$	26.64	✓
3	4.64/8	79.54	$\mathcal{R}e(C_{S_2})$	19.82	×	7.49/9	58.59	$\mathcal{R}e(C_T)$	19.74	✓	8.21/9	51.29	$\mathcal{R}e(C_T)$	5.77	✓
4	3.54/7	83.07	$\mathcal{I}m(C_{S_2})$,$\mathcal{R}e(C_{S_2})$	1.92	×	6.18/8	62.68	$\mathcal{R}e(C_T)$,$\mathcal{R}e(C_{V_2})$	2.94	✓	5.63/8	68.82	$\mathcal{R}e(C_{S_2})$,$\mathcal{R}e(C_{V_1})$	3.06	✓!
5	3.54/7	83.07	$\mathcal{R}e(C_{S_1})$,$\mathcal{R}e(C_{S_2})$	1.92	×	6.38/8	60.43	$\mathcal{R}e(C_{S_1})$,$\mathcal{R}e(C_T)$	2.41	✓!	5.65/8	68.6	$\mathcal{R}e(C_{S_1})$,$\mathcal{R}e(C_{S_2})$	3.	×
6	3.56/7	82.9	$\mathcal{R}e(C_{S_2})$,$\mathcal{R}e(C_{V_1})$	1.89	✓!	6.4/8	60.22	$\mathcal{R}e(C_{S_1})$,$\mathcal{R}e(C_{S_2})$	2.36	×	5.65/8	68.59	$\mathcal{R}e(C_{S_2})$,$\mathcal{R}e(C_{V_2})$	2.99	✓!
7	3.56/7	82.9	$\mathcal{R}e(C_{S_2})$,$\mathcal{R}e(C_T)$	1.89	✓!	6.4/8	60.21	$\mathcal{I}m(C_{S_2})$,$\mathcal{R}e(C_{S_2})$	2.36	×	5.65/8	68.59	$\mathcal{I}m(C_{S_2})$,$\mathcal{R}e(C_{S_2})$	2.99	×
8	3.56/7	82.88	$\mathcal{R}e(C_{S_2})$,$\mathcal{R}e(C_{V_2})$	1.89	✓!	6.42/8	60.02	$\mathcal{R}e(C_{S_2})$,$\mathcal{R}e(C_T)$	2.32	✓!	5.66/8	68.55	$\mathcal{R}e(C_T)$,$\mathcal{R}e(C_{V_2})$	2.98	✓
9	3.62/7	82.23	$\mathcal{R}e(C_T)$,$\mathcal{R}e(C_{V_2})$	1.78	✓	6.46/8	59.58	$\mathcal{R}e(C_{S_2})$,$\mathcal{R}e(C_{V_1})$	2.23	✓!	5.68/8	68.31	$\mathcal{R}e(C_{S_2})$,$\mathcal{R}e(C_T)$	2.92	✓!
10	3.69/7	81.45	$\mathcal{R}e(C_{S_1})$,$\mathcal{R}e(C_T)$	1.66	✓!	6.46/8	59.54	$\mathcal{R}e(C_{S_1})$,$\mathcal{R}e(C_{V_2})$	2.22	✓!	5.79/8	67.03	$\mathcal{R}e(C_{S_1})$,$\mathcal{R}e(C_T)$	2.6	✓!
11	3.7/7	81.31	$\mathcal{R}e(C_{S_1})$,$\mathcal{R}e(C_{V_2})$	1.64	✓!	6.47/8	59.45	$\mathcal{R}e(C_{S_2})$,$\mathcal{R}e(C_{V_2})$	2.2	✓!	5.85/8	66.42	$\mathcal{R}e(C_{S_1})$,$\mathcal{R}e(C_{V_2})$	2.47	✓!
12	3.76/7	80.71	$\mathcal{R}e(C_{S_1})$,$\mathcal{R}e(C_{V_1})$	1.55	✓!	6.52/8	58.91	$\mathcal{R}e(C_{S_1})$,$\mathcal{R}e(C_{V_1})$	2.1	✓!	5.96/8	65.22	$\mathcal{R}e(C_{S_1})$,$\mathcal{R}e(C_{V_1})$	2.21	✓!
13	3.79/7	80.37	$\mathcal{R}e(C_{V_1})$,$\mathcal{R}e(C_{V_2})$	1.5	✓	6.55/8	58.58	$\mathcal{I}m(C_{V_2})$,$\mathcal{R}e(C_{V_2})$	2.04	✓	6.01/8	64.62	$\mathcal{R}e(C_{V_1})$,$\mathcal{R}e(C_{V_2})$	2.1	✓
14	3.79/7	80.37	$\mathcal{I}m(C_{V_2})$,$\mathcal{R}e(C_{V_2})$	1.5	✓	6.55/8	58.58	$\mathcal{R}e(C_{V_1})$,$\mathcal{R}e(C_{V_2})$	2.04	✓	6.01/8	64.62	$\mathcal{I}m(C_{V_2})$,$\mathcal{R}e(C_{V_2})$	2.1	✓
15	3.82/7	80.08	$\mathcal{R}e(C_T)$,$\mathcal{R}e(C_{V_1})$	1.46	✓	6.63/8	57.68	$\mathcal{R}e(C_T)$,$\mathcal{R}e(C_{V_1})$	1.88	✓	6.1/8	63.63	$\mathcal{R}e(C_T)$,$\mathcal{R}e(C_{V_1})$	1.92	✓
16	3.87/7	79.49	$\mathcal{I}m(C_T)$,$\mathcal{R}e(C_T)$	1.39	✓	7.13/8	52.25	$\mathcal{I}m(C_T)$,$\mathcal{R}e(C_T)$	1.14	✓	6.68/8	57.12	$\mathcal{I}m(C_{V_1})$,$\mathcal{R}e(C_{V_1})$	1.07	✓
17	4.58/7	71.09	$\mathcal{I}m(C_{V_1})$,$\mathcal{R}e(C_{V_1})$	0.68	✓	7.24/8	51.1	$\mathcal{I}m(C_{V_1})$,$\mathcal{R}e(C_{V_1})$	1.02	✓	–	–	–	–	–

TABLE 5.4: Scenarios selected after passing the normality check and the criterion $\Delta\text{AIC}_c \leq 4$, for all data available (with or without $\mathcal{R}_{J/\Psi}$). First and second columns of each dataset represent the reduced χ^2 and corresponding p-value. Third, fourth and last columns represent the independent fit parameters, Akaike weights, and whether or not the fit results satisfy the constraint $\mathcal{B}(B_c \to \tau\nu_\tau) \leq 30\%$ respectively. '✓!' means that only some of the multiple minima satisfy this limit for the scenario in question.

Index	Data without $P_\tau(D^*)$ and $\mathcal{R}_{J/\Psi}$					Data without $P_\tau(D^*)$ ($\mathcal{R}_{J/\Psi}$ with LFCQ)					Data without $P_\tau(D^*)$ ($\mathcal{R}_{J/\Psi}$ with PQCD)				
	χ^2_{min} / DoF	p-val (%)	Param.s	w^{AIC_c}	$B_c \to \tau\nu$	χ^2_{min} / DoF	p-val (%)	Param.s	w^{AIC_c}	$B_c \to \tau\nu$	χ^2_{min} / DoF	p-val (%)	Param.s	w^{AIC_c}	$B_c \to \tau\nu$
1	3.55/7	82.95	$\mathcal{R}e(C_T)$	46.28	✓	6.92/8	54.53	$\mathcal{R}e(C_{V_1})$	28.87	✓	6.36/8	60.67	$\mathcal{R}e(C_{V_1})$	33.22	✓
2	4.27/7	74.81	$\mathcal{R}e(C_{V_1})$	22.6	✓	7.01/8	53.57	$\mathcal{R}e(C_T)$	26.42	✓	6.45/8	59.65	$\mathcal{R}e(C_{S_2})$	30.31	×
3	4.64/7	70.44	$\mathcal{R}e(C_{S_2})$	15.7	×	7.28/8	50.69	$\mathcal{R}e(C_{S_2})$	20.17	×	7.73/8	46.05	$\mathcal{R}e(C_T)$	8.48	✓
4	3.54/6	73.88	$\mathcal{R}e(C_{V_1})$,$\mathcal{R}e(C_{V_2})$	1.12	✓	6.09/7	52.87	$\mathcal{R}e(C_T)$,$\mathcal{R}e(C_{V_2})$	2.14	✓	5.57/7	59.08	$\mathcal{R}e(C_T)$,$\mathcal{R}e(C_{V_2})$	2.38	✓
5	3.54/6	73.88	$\mathcal{R}e(C_{S_1})$,$\mathcal{R}e(C_{V_1})$	1.12	✓!	6.11/7	52.66	$\mathcal{R}e(C_{S_1})$,$\mathcal{R}e(C_T)$	2.1	✓!	5.62/7	58.47	$\mathcal{R}e(C_{S_2})$,$\mathcal{R}e(C_{V_1})$	2.26	✓!
6	3.54/6	73.88	$\mathcal{R}e(C_{S_2})$,$\mathcal{R}e(C_{V_1})$	1.12	✓!	6.18/7	51.95	$\mathcal{R}e(C_{S_2})$,$\mathcal{R}e(C_T)$	1.97	✓!	5.63/7	58.36	$\mathcal{R}e(C_{S_2})$,$\mathcal{R}e(C_T)$	2.24	✓!
7	3.54/6	73.88	$\mathcal{R}e(C_T)$,$\mathcal{R}e(C_{V_1})$	1.12	✓	6.18/7	51.83	$\mathcal{R}e(C_{S_1})$,$\mathcal{R}e(C_{V_2})$	1.95	✓!	5.63/7	58.35	$\mathcal{R}e(C_{S_1})$,$\mathcal{R}e(C_T)$	2.24	✓!
8	3.54/6	73.88	$\mathcal{R}e(C_{S_1})$,$\mathcal{R}e(C_{V_2})$	1.12	✓!	6.22/7	51.47	$\mathcal{R}e(C_{S_1})$,$\mathcal{R}e(C_{V_1})$	1.89	✓!	5.64/7	58.23	$\mathcal{R}e(C_{S_2})$,$\mathcal{R}e(C_{V_2})$	2.22	✓!
9	3.54/6	73.88	$\mathcal{R}e(C_{S_2})$,$\mathcal{R}e(C_{V_2})$	1.12	✓!	6.24/7	51.25	$\mathcal{R}e(C_{S_2})$,$\mathcal{R}e(C_{V_2})$	1.86	✓!	5.65/7	58.12	$\mathcal{R}e(C_{S_1})$,$\mathcal{R}e(C_{S_2})$	2.2	×
10	3.54/6	73.88	$\mathcal{R}e(C_T)$,$\mathcal{R}e(C_{V_2})$	1.12	✓	6.27/7	50.81	$\mathcal{R}e(C_{S_2})$,$\mathcal{R}e(C_{V_1})$	1.79	✓!	5.65/7	58.1	$\mathcal{I}m(C_{S_2})$,$\mathcal{R}e(C_{S_2})$	2.19	×
11	3.54/6	73.88	$\mathcal{R}e(C_{S_1})$,$\mathcal{R}e(C_{S_2})$	1.12	×	6.29/7	50.66	$\mathcal{R}e(C_{V_1})$,$\mathcal{R}e(C_{V_2})$	1.76	✓	5.67/7	57.87	$\mathcal{R}e(C_{S_1})$,$\mathcal{R}e(C_{V_2})$	2.15	✓!
12	3.54/6	73.88	$\mathcal{R}e(C_{S_1})$,$\mathcal{R}e(C_T)$	1.12	✓!	6.29/7	50.66	$\mathcal{I}m(C_{V_2})$,$\mathcal{R}e(C_{V_2})$	1.76	✓	5.72/7	57.26	$\mathcal{R}e(C_{S_1})$,$\mathcal{R}e(C_{V_1})$	2.05	✓!
13	3.54/6	73.88	$\mathcal{R}e(C_{S_2})$,$\mathcal{R}e(C_T)$	1.12	✓!	6.34/7	50.05	$\mathcal{R}e(C_T)$,$\mathcal{R}e(C_{V_1})$	1.67	✓	5.74/7	56.98	$\mathcal{I}m(C_{V_2})$,$\mathcal{R}e(C_{V_2})$	2.	✓
14	3.54/6	73.88	$\mathcal{I}m(C_{V_2})$,$\mathcal{R}e(C_{V_2})$	1.12	✓	6.4/7	49.4	$\mathcal{R}e(C_{S_1})$,$\mathcal{R}e(C_{S_2})$	1.58	×	5.74/7	56.98	$\mathcal{R}e(C_{V_1})$,$\mathcal{R}e(C_{V_2})$	2.	✓
15	3.54/6	73.88	$\mathcal{I}m(C_{S_2})$,$\mathcal{R}e(C_{S_2})$	1.12	×	6.4/7	49.39	$\mathcal{I}m(C_{S_2})$,$\mathcal{R}e(C_{S_2})$	1.58	×	5.81/7	56.26	$\mathcal{R}e(C_T)$,$\mathcal{R}e(C_{V_1})$	1.88	✓
16	3.54/6	73.88	$\mathcal{I}m(C_T)$,$\mathcal{R}e(C_T)$	1.12	✓	6.9/7	43.92	$\mathcal{I}m(C_T)$,$\mathcal{R}e(C_T)$	0.95	✓	6.36/7	49.81	$\mathcal{I}m(C_{V_1})$,$\mathcal{R}e(C_{V_1})$	1.08	✓
17	–	–	–	–	–	6.92/7	43.72	$\mathcal{I}m(C_{V_1})$,$\mathcal{R}e(C_{V_1})$	0.94	✓	–	–	–	–	–

TABLE 5.5: Results similar to table 5.4, but with $P_\tau(D^*)$ dropped (with or without $\mathcal{R}_{J/\Psi}$).

For each such scenario k, we define a χ^2 statistic, which is a function of the real and/or imaginary parts of the Wilson coefficients (C^k_W) associated with the scenario in question, and is defined as:

$$\chi^2_k(C^k_W) = \sum_{i,j=1}^{\text{data}} \left(O^{exp}_i - O^{th}_i(C^k_W)\right) \left(V^{stat} + V^{syst}\right)^{-1}_{ij} \left(O^{exp}_j - O^{th}_j(C^k_W)\right) \\ + \chi^2_{Nuis.} \,. \tag{5.3}$$

Here, $O^{th}_p(C^k_W)$ are given by eqns. 1.39, 1.40 and sec. 1.2.2.2 as applicable and O^{exp}_p is the central value of the p^{th} experimental result. Statistical (systematic) covariance

	Belle + LHCb (Except $\mathcal{R}_{J/\Psi}$)					Belle + LHCb ($\mathcal{R}_{J/\Psi}$ with LFCQ)					Belle + LHCb ($\mathcal{R}_{J/\Psi}$ with PQCD)				
Index	χ^2_{min} / DoF	p-val (%)	Param.s	w^{AIC_c}	$B_c \to \tau\nu$	χ^2_{min} / DoF	p-val (%)	Param.s	w^{AIC_c}	$B_c \to \tau\nu$	χ^2_{min} / DoF	p-val (%)	Param.s	w^{AIC_c}	$B_c \to \tau\nu$
1	1.74/6	94.2	$\mathcal{R}e(C_{V_1})$	45.38	✓	4.56/7	71.35	$\mathcal{R}e(C_{V_1})$	46.67	✓	4.01/7	77.87	$\mathcal{R}e(C_{V_1})$	43.7	✓
2	2.41/6	87.8	$\mathcal{R}e(C_T)$	23.13	✓	5.47/7	60.25	$\mathcal{R}e(C_{S_2})$	18.72	×	4.66/7	70.08	$\mathcal{R}e(C_{S_2})$	22.69	×
3	2.78/6	83.57	$\mathcal{R}e(C_{S_2})$	16.	×	5.77/7	56.65	$\mathcal{R}e(C_T)$	13.88	✓	5.21/7	63.45	$\mathcal{R}e(C_T)$	13.17	✓
4	4.74/6	57.81	$\mathcal{R}e(C_{S_1})$	2.27	✓	7.92/7	33.97	$\mathcal{R}e(C_{V_2})$	1.62	✓	7.35/7	39.34	$\mathcal{R}e(C_{V_2})$	1.55	✓
5	5.03/6	54.	$\mathcal{R}e(C_{V_2})$	1.69	✓	4.23/6	64.62	$\mathcal{R}e(C_T)$,$\mathcal{R}e(C_{V_2})$	1.56	✓	3.65/6	72.33	$\mathcal{R}e(C_{S_2})$,$\mathcal{R}e(C_{V_1})$	1.49	✓!
6	1.45/5	91.9	$\mathcal{I}m(C_{S_2})$,$\mathcal{R}e(C_{S_2})$	0.91	×	8.04/7	32.94	$\mathcal{R}e(C_{S_1})$	1.44	✓	3.67/6	72.11	$\mathcal{R}e(C_{S_1})$,$\mathcal{R}e(C_{S_2})$	1.47	×
7	1.45/5	91.9	$\mathcal{R}e(C_{S_1})$,$\mathcal{R}e(C_{S_2})$	0.91	×	4.36/6	62.76	$\mathcal{R}e(C_{S_1})$,$\mathcal{R}e(C_T)$	1.36	✓!	3.67/6	72.09	$\mathcal{I}m(C_{S_2})$,$\mathcal{R}e(C_{S_2})$	1.46	×
8	1.48/5	91.58	$\mathcal{R}e(C_{S_2})$,$\mathcal{R}e(C_T)$	0.89	✓!	4.38/6	62.49	$\mathcal{R}e(C_{S_2})$,$\mathcal{R}e(C_T)$	1.33	✓!	3.68/6	71.99	$\mathcal{R}e(C_{S_2})$,$\mathcal{R}e(C_{V_2})$	1.45	✓!
9	1.48/5	91.58	$\mathcal{R}e(C_{S_2})$,$\mathcal{R}e(C_{V_1})$	0.89	✓!	4.39/6	62.42	$\mathcal{R}e(C_{S_1})$,$\mathcal{R}e(C_{S_2})$	1.32	×	3.69/6	71.85	$\mathcal{R}e(C_T)$,$\mathcal{R}e(C_{V_2})$	1.44	✓
10	1.48/5	91.55	$\mathcal{R}e(C_{S_2})$,$\mathcal{R}e(C_{V_2})$	0.88	✓!	4.39/6	62.4	$\mathcal{I}m(C_{S_2})$,$\mathcal{R}e(C_{S_2})$	1.32	×	3.71/6	71.57	$\mathcal{R}e(C_{S_2})$,$\mathcal{R}e(C_T)$	1.41	✓!
11	1.53/5	91.	$\mathcal{R}e(C_T)$,$\mathcal{R}e(C_{V_2})$	0.84	✓	4.43/6	61.83	$\mathcal{R}e(C_{S_1})$,$\mathcal{R}e(C_{V_2})$	1.27	✓!	7.49/7	38.	$\mathcal{R}e(C_{S_1})$	1.35	✓
12	1.53/5	90.96	$\mathcal{I}m(C_T)$,$\mathcal{R}e(C_T)$	0.84	✓	4.47/6	61.38	$\mathcal{R}e(C_{S_2})$,$\mathcal{R}e(C_{V_1})$	1.22	✓!	3.79/6	70.57	$\mathcal{R}e(C_{S_1})$,$\mathcal{R}e(C_T)$	1.31	✓!
13	–	–	–	–	–	4.48/6	61.21	$\mathcal{R}e(C_{S_1})$,$\mathcal{R}e(C_{V_1})$	1.21	✓!	3.83/6	69.91	$\mathcal{R}e(C_{S_1})$,$\mathcal{R}e(C_{V_2})$	1.24	✓!
14	–	–	–	–	–	4.48/6	61.2	$\mathcal{R}e(C_{S_2})$,$\mathcal{R}e(C_{V_2})$	1.21	✓!	3.92/6	68.68	$\mathcal{R}e(C_{S_1})$,$\mathcal{R}e(C_{V_1})$	1.14	✓!
15	–	–	–	–	–	4.49/6	61.06	$\mathcal{R}e(C_{V_1})$,$\mathcal{R}e(C_{V_2})$	1.2	✓	3.95/6	68.39	$\mathcal{I}m(C_{V_2})$,$\mathcal{R}e(C_{V_2})$	1.11	✓
16	–	–	–	–	–	4.49/6	61.06	$\mathcal{I}m(C_{V_2})$,$\mathcal{R}e(C_{V_2})$	1.2	✓	3.95/6	68.39	$\mathcal{R}e(C_{V_1})$,$\mathcal{R}e(C_{V_2})$	1.11	✓
17	–	–	–	–	–	4.52/6	60.66	$\mathcal{R}e(C_T)$,$\mathcal{R}e(C_{V_1})$	1.16	✓	3.98/6	67.99	$\mathcal{R}e(C_T)$,$\mathcal{R}e(C_{V_1})$	1.08	✓
18	–	–	–	–	–	4.56/6	60.14	$\mathcal{I}m(C_{V_1})$,$\mathcal{R}e(C_{V_1})$	1.12	✓	4.01/6	67.55	$\mathcal{I}m(C_{V_1})$,$\mathcal{R}e(C_{V_1})$	1.05	✓
19	–	–	–	–	–	4.67/6	58.65	$\mathcal{I}m(C_T)$,$\mathcal{R}e(C_T)$	1.	✓	–	–	–	–	–

TABLE 5.6: Results similar to table 5.4, but with data from *BaBaR* dropped (i.e., only with Belle and LHCb data; with or without $\mathcal{R}_{J/\Psi}$).

	All $\mathcal{R}_{D^*}$					All $\mathcal{R}_{D^*}$ + $\mathcal{R}_{J/\Psi}$ (LFCQ)					All $\mathcal{R}_{D^*}$ + $\mathcal{R}_{J/\Psi}$ (PQCD)				
Index	χ^2_{min} / DoF	p-val (%)	Param.s	w^{AIC_c}	$B_c \to \tau\nu$	χ^2_{min} / DoF	p-val (%)	Param.s	w^{AIC_c}	$B_c \to \tau\nu$	χ^2_{min} / DoF	p-val (%)	Param.s	w^{AIC_c}	$B_c \to \tau\nu$
1	2.43/5	78.76	$\mathcal{R}e(C_{V_1})$	19.6	✓	5.08/6	53.35	$\mathcal{R}e(C_T)$	21.21	✓	4.51/6	60.75	$\mathcal{R}e(C_T)$	19.79	✓
2	2.43/5	78.76	$\mathcal{R}e(C_{V_2})$	19.6	✓	5.15/6	52.53	$\mathcal{R}e(C_{V_2})$	19.89	✓	4.53/6	60.49	$\mathcal{R}e(C_{S_1})$	19.41	×
3	2.43/5	78.76	$\mathcal{R}e(C_{S_1})$	19.6	×	5.16/6	52.29	$\mathcal{R}e(C_{V_1})$	19.51	✓	4.53/6	60.49	$\mathcal{R}e(C_{S_2})$	19.41	×
4	2.43/5	78.76	$\mathcal{R}e(C_{S_2})$	19.6	×	5.28/6	50.8	$\mathcal{R}e(C_{S_1})$	17.31	×	4.56/6	60.13	$\mathcal{R}e(C_{V_2})$	18.89	✓
5	2.43/5	78.76	$\mathcal{R}e(C_T)$	19.6	✓	5.28/6	50.8	$\mathcal{R}e(C_{S_2})$	17.31	×	4.61/6	59.47	$\mathcal{R}e(C_{V_1})$	17.98	✓
6	–	–	–	–	–	4.8/5	44.03	$\mathcal{R}e(C_T)$,$\mathcal{R}e(C_{V_2})$	0.42	✓	–	–	–	–	–

TABLE 5.7: Results similar to table 5.4, but only with all $\mathcal{R}_{D^*}$ data (with or without $\mathcal{R}_{J/\Psi}$).

Parameters	Value	Correlation				
ρ^2_D	1.138(23)	1.	0.15	-0.01	-0.07	0
$\rho^2_{D^*}$	1.251(113)		1.	0.08	-0.80	0
$R_1(1)$	1.370(36)			1.	-0.08	0
$R_2(1)$	0.888(65)				1.	0
$R_0(1)$	1.196(102)					1

TABLE 5.8: Nuisance inputs to create $\chi^2_{nuis.}$ defined in eq. 5.4. These are obtained from the analysis in ref. [26].

matrices $V^{stat(syst)}$, are constructed by taking separate correlations, wherever available. The nuisance parameters (Table 5.8) occurring in the theoretical expressions are tuned in to the fit using a term

$$\chi^2_{Nuis.} = \sum_{i,j=1}^{\text{theory}} \left(\mathrm{I}^p_i - \mathrm{v}^p_i\right) \ \left(V^{Nuis}\right)^{-1}_{ij} \left(\mathrm{I}^p_j - \mathrm{v}^p_j\right) \,,$$

where I^p_k and v^p_k are the k^{th} input parameter and its respective value. For each scenario,

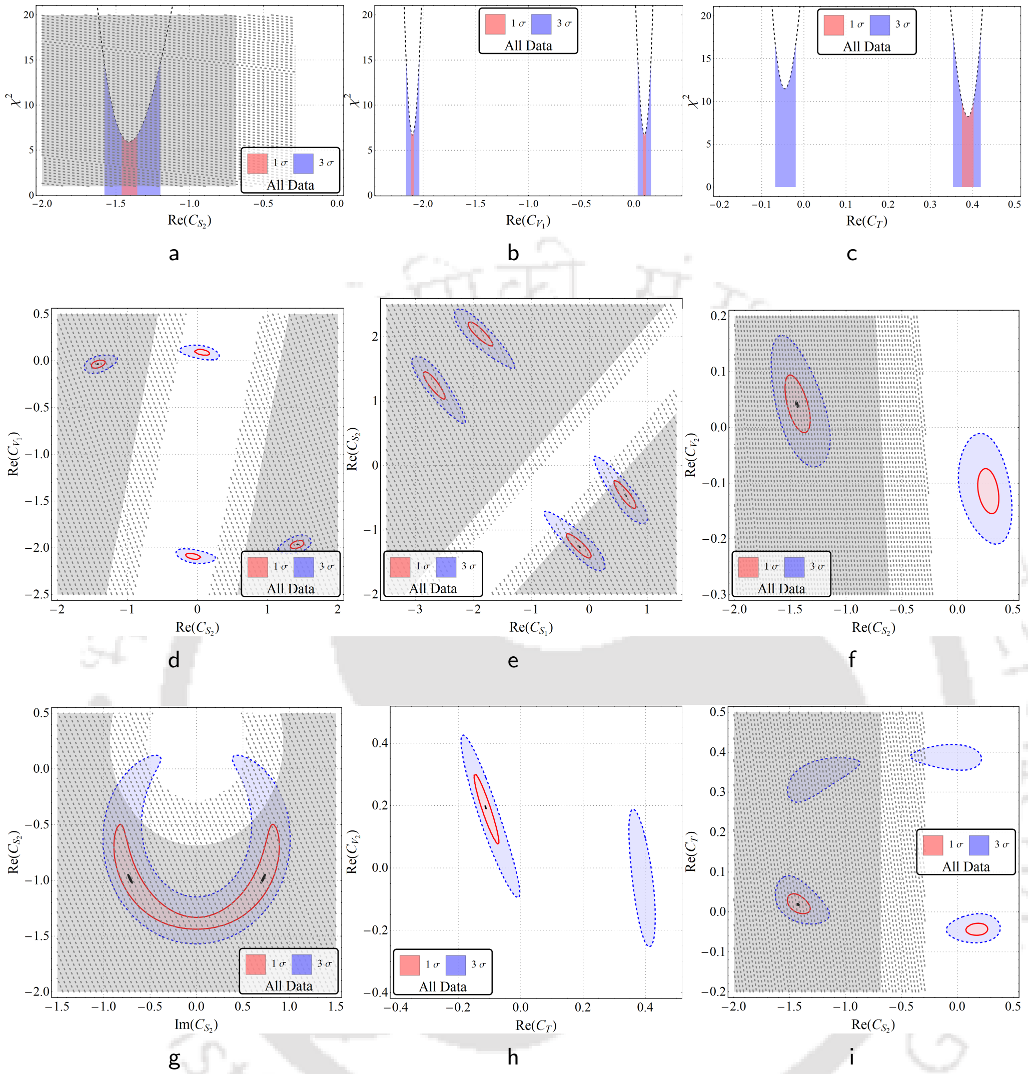

Fig. 5.1 The allowed parameter space of NP Wilson coefficients and their correlations considered in different scenarios for the dataset with all data, where $\mathcal{R}_{J/\Psi}$ is calculated in PQCD (last dataset of tables 5.4 and 5.9). Red (solid) and blue (dashed) contours enclose respectively 1σ and 3σ confidence levels(C.L.), as defined in section 5.4.1. Shaded and diagonally hatched overlay regions represents parameter space disallowed by constraints $\mathcal{B}(B_c \to \tau\nu_\tau) \leq 30\%$ and 10% respectively. These plots are continued to the next figure 5.2.

we perform two sets of fits. First, we use different combinations of the experimental results of $\mathcal{R}_{D^{(*)}}$ (and $P_\tau(D^*)$). For the second set, we redo the fits including $\mathcal{R}_{J/\psi}$. As the form factor parametrization, as well as the single experimental result for $\mathcal{R}_{J/\psi}$ are quite imprecise, instead of defining a $\chi^2_{nuis.}(\mathcal{R}_{J/\psi})$, we add the SM uncertainty of $\mathcal{R}_{J/\psi}$

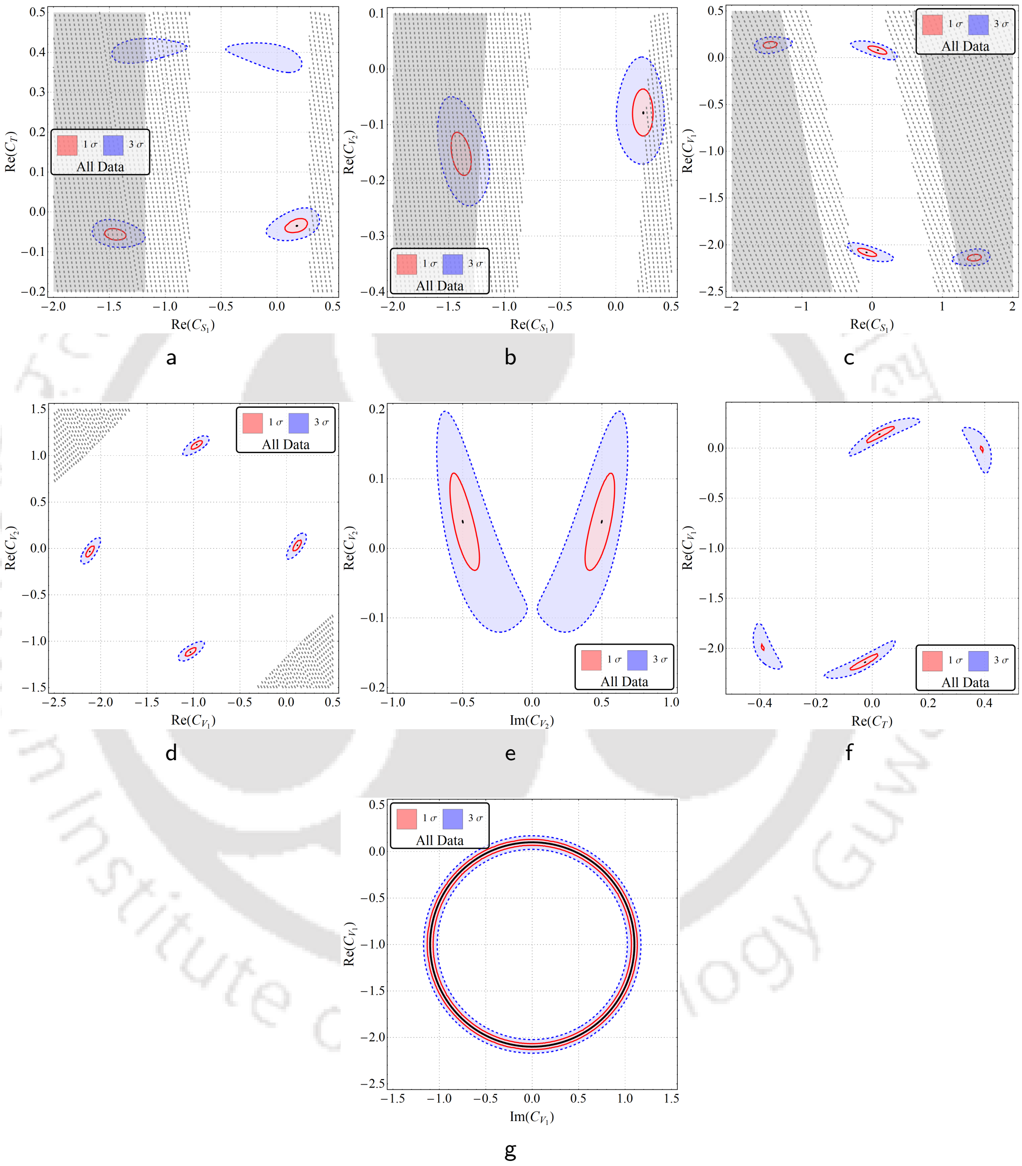

Fig. 5.2 Plots for the remaining scenarios, continued from figure 5.1.

in quadrature to the experimental one. Following the discussion in sec. 1.2.2.2, we do two sets of fits in this stage, with two different sets of form factor parametrization for $B_c \to J/\Psi$, namely LFCQ and PQCD.

After each fit, we determine the quality of it in terms of the p-value obtained corresponding to the χ^2_{min} values and the degrees of freedom (DoF) for that fit. We also double check the quality of the fit and existence of outliers in the fitted dataset by constructing a 'Pull' ($= \left(O_i^{exp} - O_i^{th}(C_W^k)\right) / (\Delta O_i^{exp})$) for each data-point and checking the normality (i.e. the probability that it is consistent with a Gaussian of $\mu = 0$ and $\sigma = 1$) of their distribution. Due to the small number of data-points in this analysis, no readily available normality test can perform with certainty and it is necessary to scrutinize each individual pull distribution. Still, we perform a variant of the "Shapiro-Wik" normality test as an extra criteria for elimination of scenarios. In other words, we drop the fits which have a pull distribution with probability to be a normal distribution $\leq 5\%$. Finally, we add the constraints according to sec. 1.2.2.5 and 1.3 to our analysis and obtain the allowed parameter space. Next, we perform a model-selection procedure on the remaining set of viable scenarios for each data-set. In the following sub-section, we elaborate the method used to do the multi-model selection procedure.

5.4 Results

Following the methodology described in the previous subsection, we have taken several combinations of the available data and have performed the analysis in the following stages for each dataset.

5.4.1 Model selection

We have created the χ^2_k statistic for the k^{th} scenario containing real and imaginary parts of Wilson coefficients C_W^k, and repeated that for all k (let us reiterate here that scenarios containing all imaginary C_Ws are neglected). We have taken scenarios with as many as 4 individual components of $\mathcal{R}e$(or $\mathcal{I}m$)(C_W). Then we have minimized each of those over the corresponding parameter space (with the form factor parameters as nuisance parameters). After checking normality for each fit and dropping scenarios with $\leq 5\%$

Data Without $\mathcal{R}_{J/\Psi}$				All Data ($\mathcal{R}_{J/\Psi}$ with LFCQ)				All Data ($\mathcal{R}_{J/\Psi}$ with PQCD)			
Index	Param.s	Best-fit	Correlation	Index	Param.s	Best-fit	Correlation	Index	Param.s	Best-fit	Correlation
1	$\mathcal{R}e(C_T)$	0.387(11)	–	1	$\mathcal{R}e(C_{V_1})$	0.100(22)	–	2	$\mathcal{R}e(C_{V_1})$	0.100(21)	–
2	$\mathcal{R}e(C_{V_1})$	0.098(22)	–	3	$\mathcal{R}e(C_T)$	0.389(10)	–	3	$\mathcal{R}e(C_T)$	0.389(10)	–
6	$\mathcal{R}e(C_{S_2})$ $\mathcal{R}e(C_{V_1})$	0.073(79) 0.089(24)	-0.409	4	$\mathcal{R}e(C_T)$ $\mathcal{R}e(C_{V_2})$	-0.113(26) 0.195(74)	-0.93	4	$\mathcal{R}e(C_{S_2})$ $\mathcal{R}e(C_{V_1})$	0.072(79) 0.090(24)	-0.411
7	$\mathcal{R}e(C_{S_2})$ $\mathcal{R}e(C_T)$	0.181(67) -0.043(11)	0.075	5	$\mathcal{R}e(C_{S_1})$ $\mathcal{R}e(C_T)$	0.179(66) -0.034(12)	0.35	6	$\mathcal{R}e(C_{S_2})$ $\mathcal{R}e(C_{V_2})$	0.280(68) -0.112(29)	-0.3
8	$\mathcal{R}e(C_{S_2})$ $\mathcal{R}e(C_{V_2})$	0.279(68) -0.111(29)	-0.302	8	$\mathcal{R}e(C_{S_2})$ $\mathcal{R}e(C_T)$	0.181(67) -0.043(11)	0.074	8	$\mathcal{R}e(C_T)$ $\mathcal{R}e(C_{V_2})$	-0.113(26) 0.195(74)	-0.93
9	$\mathcal{R}e(C_T)$ $\mathcal{R}e(C_{V_2})$	-0.112(26) 0.196(74)	-0.93	9	$\mathcal{R}e(C_{S_2})$ $\mathcal{R}e(C_{V_1})$	0.072(79) 0.090(24)	-0.411	9	$\mathcal{R}e(C_{S_2})$ $\mathcal{R}e(C_T)$	0.181(67) -0.043(11)	0.078
10	$\mathcal{R}e(C_{S_1})$ $\mathcal{R}e(C_T)$	0.179(66) -0.033(12)	0.351	10	$\mathcal{R}e(C_{S_1})$ $\mathcal{R}e(C_{V_2})$	0.246(61) -0.078(28)	-0.009	10	$\mathcal{R}e(C_{S_1})$ $\mathcal{R}e(C_T)$	0.179(66) -0.034(12)	0.35
11	$\mathcal{R}e(C_{S_1})$ $\mathcal{R}e(C_{V_2})$	0.245(60) -0.075(28)	-0.01	11	$\mathcal{R}e(C_{S_2})$ $\mathcal{R}e(C_{V_2})$	0.280(68) -0.112(29)	-0.3	11	$\mathcal{R}e(C_{S_1})$ $\mathcal{R}e(C_{V_2})$	0.247(61) -0.079(28)	-0.008
12	$\mathcal{R}e(C_{S_1})$ $\mathcal{R}e(C_{V_1})$	0.086(90) 0.078(30)	-0.684	12	$\mathcal{R}e(C_{S_1})$ $\mathcal{R}e(C_{V_1})$	0.085(90) 0.079(30)	-0.684	12	$\mathcal{R}e(C_{S_1})$ $\mathcal{R}e(C_{V_1})$	0.085(90) 0.079(30)	-0.684
13	$\mathcal{R}e(C_{V_1})$ $\mathcal{R}e(C_{V_2})$	0.117(31) 0.037(41)	0.709	13	$\mathcal{I}m(C_{V_2})$ $\mathcal{R}e(C_{V_2})$	0.499(68) 0.039(46)	0.718	13	$\mathcal{R}e(C_{V_1})$ $\mathcal{R}e(C_{V_2})$	0.118(31) 0.034(41)	0.712
14	$\mathcal{I}m(C_{V_2})$ $\mathcal{R}e(C_{V_2})$	0.497(68) 0.042(46)	0.716	14	$\mathcal{R}e(C_{V_1})$ $\mathcal{R}e(C_{V_2})$	0.117(31) 0.037(41)	0.709	14	$\mathcal{I}m(C_{V_2})$ $\mathcal{R}e(C_{V_2})$	0.499(68) 0.038(46)	0.718
15	$\mathcal{R}e(C_T)$ $\mathcal{R}e(C_{V_1})$	0.030(34) 0.142(54)	0.917	15	$\mathcal{R}e(C_T)$ $\mathcal{R}e(C_{V_1})$	0.026(34) 0.140(54)	0.918	15	$\mathcal{R}e(C_T)$ $\mathcal{R}e(C_{V_1})$	0.026(34) 0.139(54)	0.918
16	$\mathcal{I}m(C_T)$ $\mathcal{R}e(C_T)$	0.16(15) 0.32(15)	-0.995	16	$\mathcal{I}m(C_T)$ $\mathcal{R}e(C_T)$	-0.18(11) 0.30(15)	0.993	16	See figure 5.2g		
17	See Plot			17	See Plot			-	-	-	-

TABLE 5.9: Best fit results and correlations of the scenarios listed in table 5.4. We omit the scenarios disallowed by the constraint $\mathcal{B}(B_c \to \tau\nu_\tau) \leq 30\%$. For the cases where only some of the minima are allowed by the constraint, we quote only those of them allowed by the constraint and closest to the SM point at the same time. Elaboration is in section 5.4.2. For scenarios where the best fit, instead of being an isolated point, is actually a contour in the parameter-space, we ask the reader to check the corresponding plot. Figure 5.2g is the plot for scenario 16 in the last dataset of this table.

significance, we have arranged the remaining scenarios in ascending order of AIC$_c$ and have kept only those with $\Delta\text{AIC}_c \leq 4$. These are, essentially, the best scenarios to explain the data in that specific dataset under the present experimental constraints.

Tables 5.4, 5.5, 5.6 and 5.7 contain the listed scenarios of the data sets which are obtained from table 1.4. Each table essentially contains three variations of similar datasets: the first one is data without $\mathcal{R}_{J/\Psi}$ and the rest two, with it. The reason for treating $\mathcal{R}_{J/\Psi}$ separately is the apparent tension of the measured central value with that of the SM one, as explained in section 1.3. Moreover, the theoretical values of $\mathcal{R}_{J/\Psi}$ are heavily dependent on form factor parametrisation and differ considerably over different choices of it, as explained in section 1.2.2.2. Thus we treat two parametrisations, namely LFCQ and PQCD separately in second and third datasets of each table respectively. As PQCD predicts relatively higher values for $\mathcal{R}_{J/\Psi}$, fits are generally better for these sets than those corresponding to the LFCQ ones, as can be checked from the p-values listed in the

Data without $P_\tau(D^*)$ and $\mathcal{R}_{J/\Psi}$				Data without $P_\tau(D^*)$ ($\mathcal{R}_{J/\Psi}$ with LFCQ)				Data without $P_\tau(D^*)$ ($\mathcal{R}_{J/\Psi}$ with PQCD)			
Index	Param.s	Best-fit	Correlation	Index	Param.s	Best-fit	Correlation	Index	Param.s	Best-fit	Correlation
1	$\mathcal{R}e(C_T)$	0.387(11)	–	1	$\mathcal{R}e(C_{V_1})$	0.101(22)	–	1	$\mathcal{R}e(C_{V_1})$	0.101(22)	–
2	$\mathcal{R}e(C_{V_1})$	0.099(22)	–	2	$\mathcal{R}e(C_T)$	0.389(11)	–	3	$\mathcal{R}e(C_T)$	0.389(11)	–
4	$\mathcal{R}e(C_{V_1})$ $\mathcal{R}e(C_{V_2})$	0.118(31) 0.036(41)	0.707	4	$\mathcal{R}e(C_T)$ $\mathcal{R}e(C_{V_2})$	-0.112(26) 0.193(74)	-0.93	4	$\mathcal{R}e(C_T)$ $\mathcal{R}e(C_{V_2})$	-0.112(26) 0.193(74)	-0.93
5	$\mathcal{R}e(C_{S_1})$ $\mathcal{R}e(C_{V_1})$	0.082(90) 0.080(30)	-0.687	5	$\mathcal{R}e(C_{S_1})$ $\mathcal{R}e(C_T)$	0.178(67) -0.034(12)	0.353	5	$\mathcal{R}e(C_{S_2})$ $\mathcal{R}e(C_{V_1})$	0.070(79) 0.091(24)	-0.412
6	$\mathcal{R}e(C_{S_2})$ $\mathcal{R}e(C_{V_1})$	0.071(79) 0.090(24)	-0.409	6	$\mathcal{R}e(C_{S_2})$ $\mathcal{R}e(C_T)$	0.180(67) -0.044(11)	0.075	6	$\mathcal{R}e(C_{S_2})$ $\mathcal{R}e(C_T)$	0.180(67) -0.044(11)	0.074
7	$\mathcal{R}e(C_T)$ $\mathcal{R}e(C_{V_1})$	0.029(34) 0.143(54)	0.916	7	$\mathcal{R}e(C_{S_1})$ $\mathcal{R}e(C_{V_2})$	0.245(61) -0.077(28)	-0.01	7	$\mathcal{R}e(C_{S_1})$ $\mathcal{R}e(C_T)$	0.178(67) -0.034(12)	0.352
8	$\mathcal{R}e(C_{S_1})$ $\mathcal{R}e(C_{V_2})$	0.245(61) -0.077(28)	-0.009	8	$\mathcal{R}e(C_{S_1})$ $\mathcal{R}e(C_{V_1})$	0.081(90) 0.081(30)	-0.687	8	$\mathcal{R}e(C_{S_2})$ $\mathcal{R}e(C_{V_2})$	0.282(68) -0.114(30)	-0.302
9	$\mathcal{R}e(C_{S_2})$ $\mathcal{R}e(C_{V_2})$	0.280(68) -0.113(30)	-0.304	9	$\mathcal{R}e(C_{S_2})$ $\mathcal{R}e(C_{V_2})$	0.282(68) -0.116(29)	-0.302	11	$\mathcal{R}e(C_{S_1})$ $\mathcal{R}e(C_{V_2})$	0.247(61) -0.080(28)	-0.007
10	$\mathcal{R}e(C_T)$ $\mathcal{R}e(C_{V_2})$	-0.111(26) 0.194(75)	-0.93	10	$\mathcal{R}e(C_{S_2})$ $\mathcal{R}e(C_{V_1})$	0.067(79) 0.093(24)	-0.407	12	$\mathcal{R}e(C_{S_1})$ $\mathcal{R}e(C_{V_1})$	0.081(90) 0.081(30)	-0.686
12	$\mathcal{R}e(C_{S_1})$ $\mathcal{R}e(C_T)$	0.178(67) -0.034(12)	0.353	11	$\mathcal{R}e(C_{V_1})$ $\mathcal{R}e(C_{V_2})$	0.118(31) 0.036(41)	0.707	13	$\mathcal{I}m(C_{V_2})$ $\mathcal{R}e(C_{V_2})$	-0.500(68) 0.037(46)	-0.716
13	$\mathcal{R}e(C_{S_2})$ $\mathcal{R}e(C_T)$	-0.011(89) 0.387(11)	-0.129	12	$\mathcal{I}m(C_{V_2})$ $\mathcal{R}e(C_{V_2})$	0.500(68) 0.037(46)	0.716	14	$\mathcal{R}e(C_{V_1})$ $\mathcal{R}e(C_{V_2})$	0.118(31) 0.036(41)	0.707
14	$\mathcal{I}m(C_{V_2})$ $\mathcal{R}e(C_{V_2})$	0.499(68) 0.040(46)	0.714	13	$\mathcal{R}e(C_T)$ $\mathcal{R}e(C_{V_1})$	0.025(34) 0.140(54)	0.917	15	$\mathcal{R}e(C_T)$ $\mathcal{R}e(C_{V_1})$	0.025(34) 0.139(54)	0.917
16	$\mathcal{I}m(C_T)$ $\mathcal{R}e(C_T)$	0.094(359) 0.37(17)	-0.998	16	$\mathcal{I}m(C_T)$ $\mathcal{R}e(C_T)$	0.15(19) 0.33(17)	-0.997	16	See Plot		
-	-	-	-	17	See Plot			-	-	-	-

TABLE 5.10: Results for the scenarios listed in table 5.5, following the convention of table 5.9.

Belle + LHCb (Except $\mathcal{R}_{J/\Psi}$)				Belle + LHCb ($\mathcal{R}_{J/\Psi}$ with LFCQ)				Belle + LHCb ($\mathcal{R}_{J/\Psi}$ with PQCD)			
Index	Param.s	Best-fit	Correlation	Index	Param.s	Best-fit	Correlation	Index	Param.s	Best-fit	Correlation
1	$\mathcal{R}e(C_{V_1})$	0.075(26)	–	1	$\mathcal{R}e(C_{V_1})$	0.078(26)	–	1	$\mathcal{R}e(C_{V_1})$	0.078(26)	–
2	$\mathcal{R}e(C_T)$	0.379(13)	–	3	$\mathcal{R}e(C_T)$	-0.037(13)	–	3	$\mathcal{R}e(C_T)$	-0.037(13)	–
4	$\mathcal{R}e(C_{S_1})$	0.179(81)	–	4	$\mathcal{R}e(C_{V_2})$	-0.074(34)	–	4	$\mathcal{R}e(C_{V_2})$	-0.074(33)	–
5	$\mathcal{R}e(C_{V_2})$	-0.069(34)	–	5	$\mathcal{R}e(C_T)$ $\mathcal{R}e(C_{V_2})$	-0.086(38) 0.14(10)	-0.951	5	$\mathcal{R}e(C_{S_2})$ $\mathcal{R}e(C_{V_1})$	0.033(108) 0.073(27)	-0.309
8	$\mathcal{R}e(C_{S_2})$ $\mathcal{R}e(C_T)$	0.126(96) -0.035(13)	0.015	6	$\mathcal{R}e(C_{S_1})$	0.180(81)	–	8	$\mathcal{R}e(C_{S_2})$ $\mathcal{R}e(C_{V_2})$	0.209(98) -0.092(34)	-0.295
9	$\mathcal{R}e(C_{S_2})$ $\mathcal{R}e(C_{V_1})$	0.034(108) 0.072(27)	-0.306	7	$\mathcal{R}e(C_{S_1})$ $\mathcal{R}e(C_T)$	0.125(94) -0.029(14)	0.361	9	$\mathcal{R}e(C_T)$ $\mathcal{R}e(C_{V_2})$	-0.086(38) 0.14(10)	-0.952
10	$\mathcal{R}e(C_{S_2})$ $\mathcal{R}e(C_{V_2})$	0.207(98) -0.091(34)	-0.298	8	$\mathcal{R}e(C_{S_2})$ $\mathcal{R}e(C_T)$	0.126(96) -0.035(13)	0.015	10	$\mathcal{R}e(C_{S_2})$ $\mathcal{R}e(C_T)$	0.126(96) -0.036(13)	0.019
11	$\mathcal{R}e(C_T)$ $\mathcal{R}e(C_{V_2})$	-0.085(38) 0.14(10)	-0.951	11	$\mathcal{R}e(C_{S_1})$ $\mathcal{R}e(C_{V_2})$	0.183(86) -0.065(33)	0.062	11	$\mathcal{R}e(C_{S_1})$	0.181(81)	–
12	$\mathcal{I}m(C_T)$ $\mathcal{R}e(C_T)$	0.206(29) 0.20(19)	-0.898	12	$\mathcal{R}e(C_{S_2})$ $\mathcal{R}e(C_{V_1})$	0.033(108) 0.073(27)	-0.309	12	$\mathcal{R}e(C_{S_1})$ $\mathcal{R}e(C_T)$	0.125(94) -0.029(14)	0.361
- -	- -	- -	- -	13	$\mathcal{R}e(C_{S_1})$ $\mathcal{R}e(C_{V_1})$	0.043(122) 0.067(34)	-0.656	13	$\mathcal{R}e(C_{S_1})$ $\mathcal{R}e(C_{V_2})$	0.183(86) -0.065(33)	0.062
- -	- -	- -	- -	14	$\mathcal{R}e(C_{S_2})$ $\mathcal{R}e(C_{V_2})$	0.208(98) -0.092(34)	-0.295	14	$\mathcal{R}e(C_{S_1})$ $\mathcal{R}e(C_{V_1})$	0.043(122) 0.067(34)	-0.656
- -	- -	- -	- -	15	$\mathcal{R}e(C_{V_1})$ $\mathcal{R}e(C_{V_2})$	0.086(42) 0.018(54)	0.788	15	$\mathcal{I}m(C_{V_2})$ $\mathcal{R}e(C_{V_2})$	0.42(11) 0.015(59)	0.794
- -	- -	- -	- -	16	$\mathcal{I}m(C_{V_2})$ $\mathcal{R}e(C_{V_2})$	-0.42(11) 0.016(59)	-0.794	16	$\mathcal{R}e(C_{V_1})$ $\mathcal{R}e(C_{V_2})$	0.086(42) 0.018(54)	0.788
- -	- -	- -	- -	17	$\mathcal{R}e(C_T)$ $\mathcal{R}e(C_{V_1})$	0.0086(433) 0.092(77)	0.941	17	$\mathcal{R}e(C_T)$ $\mathcal{R}e(C_{V_1})$	0.0078(429) 0.091(76)	0.941
- -	- -	- -	- -	18	See Plot			18	See Plot		
- -	- -	- -	- -	19	$\mathcal{I}m(C_T)$ $\mathcal{R}e(C_T)$	0.210(15) 0.16(19)	0.55	- -	- -	- -	- -

TABLE 5.11: Results for the scenarios listed in table 5.6, following the convention of table 5.9.

All $\mathcal{R}_{D^*}$				All $\mathcal{R}_{D^*}$ + $\mathcal{R}_{J/\Psi}$ (LFCQ)				All $\mathcal{R}_{D^*}$ + $\mathcal{R}_{J/\Psi}$ (PQCD)			
Index	Param.s	Best-fit	Correlation	Index	Param.s	Best-fit	Correlation	Index	Param.s	Best-fit	Correlation
1	$\mathcal{R}e(C_{V_1})$	0.086(26)	–	1	$\mathcal{R}e(C_T)$	-0.040(11)	–	1	$\mathcal{R}e(C_T)$	-0.040(11)	–
2	$\mathcal{R}e(C_{V_2})$	-0.095(29)	–	2	$\mathcal{R}e(C_{V_2})$	-0.099(28)	–	4	$\mathcal{R}e(C_{V_2})$	-0.099(28)	–
5	$\mathcal{R}e(C_T)$	-0.039(11)	–	3	$\mathcal{R}e(C_{V_1})$	0.089(26)	–	5	$\mathcal{R}e(C_{V_1})$	0.089(26)	–
-	-	-	-	6	See Plot			-	-	-	-

Table 5.12: Results for the scenarios listed in table 5.7, following the convention of table 5.9.

second column of these datasets. The measured value of $P_\tau(D^*)$ has large error. Therefore,we have dropped τ-polarization asymmetry from the list of inputs in one of the fits (table 5.5). The measured values of $\mathcal{R}_{D^{(*)}}$ by BABAR are relatively old, and are largely deviated from the respective SM predictions. Therefore, in order to check the impact of BABAR data on our model selections, in one of the fit scenario we have dropped the BABAR data (table 5.6). We have also done the analysis with the measured $\mathcal{R}_{D^*}$ alone, which will help us to figure out the sensitivity of this observable towards a particular type of NP scenario.

We notice that for all datasets, the maximum number of independent fit parameters (for listed scenarios) is 2. As is explained in the previous sections, this is natural, because AIC$_c$ penalises the increased variance associated with increase in number of independent parameters. The fourth column in these tables, for each dataset, lists the w^{AIC_c} for each scenario, which estimates the relative likelihood for that scenario (among the given set of scenarios, the number of which is $\approx 90 \sim 95$ for our analysis) to explain the data. As can be seen, the first few scenarios take up a large chunk of the total likelihood and it is evident that all unselected scenarios together constitute a very small fraction of it. This is another way of understanding why the listed scenarios are the best ones suited to describe the given dataset.

Once we have listed the best scenarios, we scrutinise the allowed parameter space for each of them. As all the finally selected models have a most of two parameters (other than the nuisance parameters), we can plot the marginal confidence levels in the fit-parameter-space with the help of the defined χ^2 function. We have prepared plots for each of these scenarios either in terms of the goodness-of-fit contours (for two parameter scenarios), or by directly plotting the χ^2 with respect to the parameter (for single parameter scenarios). The contour plots are prepared with constant χ^2 contours equivalent to 1σ and 3σ that correspond to confidence levels of 68.27% and 99.73% respectively. For two parameters, the constant χ^2 values are $= \chi^2_{min} + \Delta\chi^2$, where χ^2_{min} is the minimum value of χ^2 obtained after minimization over the parameter space, and $\Delta\chi^2 = 2.296$ and 11.83 for 1σ and 3σ respectively. Similarly, for single parameter case, 1σ and 3σ intervals are shown with $\Delta\chi^2 = 1$ and 9 respectively. As a representative case, we have shown the plots for all scenarios listed in the last dataset of table 5.4 ('All data', where the theoretical value of $\mathcal{R}_{J/\Psi}$ is calculated in PQCD) in figures 5.1 and 5.2.

We then use the limits on $\mathcal{B}(B_c \to \tau\nu)$ mentioned in section 1.3 as our conservative constraint on each scenario. In the aforementioned tables (5.4, 5.5, 5.6 and 5.7), the last column of each dataset indicates whether the corresponding scenario passes the constraint of $\mathcal{B}(B_c \to \tau\nu) \leq 30\%$ ('✓') or not ('✗'). For many scenarios, there are multiple best-fit points (or at least, multiple 68% confidence regions). In some cases, some of these multiple minima are ruled out from the $\mathcal{B}(B_c \to \tau\nu) \leq 30\%$ constraints, while the rest are allowed. These scenarios are marked as '✓!' in the said column. By observing the nature of the confidence levels in the parameter space, we can pick out the minima which are allowed.

In case of the plots depicting the parameter space, we show two limits: regions disallowed by $\mathcal{B}(B_c \to \tau\nu) \leq 30\%$ (gray shaded region) and $\mathcal{B}(B_c \to \tau\nu) \leq 10\%$ (diagonally hatched region) respectively. The first one is the conservative limit from B_c decay width and the second aggressive one is motivated from the studies quoted in section 1.3 (though we are calling it aggressive, it is a perfectly reasonable upper bound, given the $\sim 2\%$ SM prediction as shown in table 5.1). We know that even if present, any NP effect is going to be small. Thus when multiple minima are allowed by these constraints, we quote the results for those which are closest to the origin (corresponding to SM) in further analysis[1]. One more thing to note here is that scenarios with either real or imaginary part of C_T will not have any constraint on the corresponding axis in the parameter space, as $\mathcal{B}(B_c \to \tau\nu)$ is unaffected by tensor interactions.

Our results of the model selection with all the available data are shown in table 5.4. We note that the best possible scenarios are the models with either of the operator $\mathcal{O}_T^\ell$ or $\mathcal{O}_{V_1}^\ell$ with real C_W. The explanations with the operator $\mathcal{O}_{S_1}^\ell$ are disfavoured by the bound from $\mathcal{B}(B_c \to \tau\nu_\tau)$. These one-operator scenarios are allowed even if we choose $\Delta\text{AIC}_c \leq 2$. The same criterion does not allow the two-operator scenarios. However, the constrain

---

[1] As an example, for scenario 4 given in the last dataset of table 5.4 (with $\mathcal{R}e(C_{S_2})$ and $\mathcal{R}e(C_{V_1})$), the symbol for the constraint column is '✓!'. The corresponding plot in figure 5.1d shows that out of the 4 possible minima, only 2 are outside the shaded regions. Interestingly, the global minima of the χ^2 in this case lies within the shaded region (thus disallowed), but there are two more allowed local 1σ C.L regions. In table 5.9 (last dataset), the corresponding result is quoted for the one closest to zero.

Data without $\mathcal{R}_{J/\Psi}$						
Scenario	$\mathcal{R}_{D^*}$	$\mathcal{R}_D$	$P_\tau(D^*)$	$P_\tau(D)$	$F_L^{D^*}$	$\mathcal{A}^*_{FB}$
1	0.306(12)(14)	0.412(4)(3)	0.125(11)(11)	0.1799(4)(33)	0.134(15)(6)	0.027 (8)(12)
2	0.312(7)(12)	0.368(4)(14)	-0.493(25)(0)	0.3355(4)(0)	0.456(10)(0)	-0.059(14)(0)
6	0.305(7)(15)	0.406(4)(47)	-0.504(23)(13)	0.4080(5)(746)	0.452(10)(5)	-0.063(13)(5)
7	0.305(5)(15)	0.406(4)(47)	-0.485(16)(15)	0.5321 (5)(531)	0.431(7)(5)	-0.021(10)(13)
8	0.305(6)(15)	0.406(4)(47)	-0.534(19)(10)	0.6055 (6)(493)	0.450(9)(4)	-0.038(11)(10)
9	0.305(5)(15)	0.407(4)(46)	-0.381(12)(35)	0.3845 (4)(92)	0.396(7)(18)	0.006(8)(11)
10	0.305(7)(15)	0.407(4)(46)	-0.436(25)(12)	0.5263(5)(512)	0.457(10)(8)	-0.007(13)(12)
11	0.305(8)(15)	0.407(4)(46)	-0.443(32)(12)	0.5737(6)(447)	0.480(12)(5)	-0.017(15)(10)
12	0.305(7)(15)	0.407(4)(46)	-0.475(27)(17)	0.4212 (5)(840)	0.463(11)(6)	-0.052(14)(6)
13	0.305(7)(15)	0.407(4)(46)	-0.492(25)(1)	0.3355(4)(0)	0.454(10)(4)	-0.070(14)(14)
14	0.305(7)(15)	0.407(4)(46)	-0.492(25)(1)	0.3355(4)(0)	0.454(10)(4)	0.010(12)(13)
15	0.305(8)(15)	0.406(4)(47)	-0.505(28)(12)	0.3227(4)(1411)	0.463(12)(5)	-0.090(15)(37)
16	0.308(11)(14)	0.394(4)(42)	0.036(9)(211)	0.2001(4)(499)	0.181(14)(111)	0.023(8)(17)

TABLE 5.13: Predictions for observables listed in table 5.1, for different scenarios listed in the first dataset of table 5.9. We have omitted the scenario where the best fit is a contour instead of a curve (scenario 17). Each result contains two uncertainties: the first one for uncertainties in form factors and the second one for uncertainties of the fitted NP Wilson coefficients. Though in most cases the NP error is predominant compared to the form factor ones, we quote both of them. These results continue in the next table 5.14.

$\Delta\text{AIC}_c \leq 4$ allows a few of the two-operator scenarios. In all these less preferred two-operator scenarios, the operators like $\mathcal{O}^\ell_{V_2}$, $\mathcal{O}^\ell_{S_1}$, $\mathcal{O}^\ell_{S_2}$ appears in combination with either of $\mathcal{O}^\ell_T$ and $\mathcal{O}^\ell_{V_1}$. Also, we note that the operator $\mathcal{O}^\ell_{V_2}$ with complex C_W is favoured by the data.

As can be seen in table 5.5, our conclusions on the selected models will not change if we drop the experimental input on $P_\tau(D^*)$ from our fit. Also, if we drop the BABAR data on $\mathcal{R}_{D^{(*)}}$ from the list of the inputs for the fit, the best preferred scenarios are still the one with the operator $\mathcal{O}^\ell_T$ or $\mathcal{O}^\ell_{V_1}$ with real C_Ws. However, there are other one-operator scenarios with $\mathcal{O}^\ell_{V_2}$ or $\mathcal{O}^\ell_{S_1}$ with real C_Ws which are then allowed by the criterion $\Delta\text{AIC}_c \leq 4$; see table 5.6 for detail. Here too, there are a few two-operator scenarios which successfully pass the above mentioned criterion. Finally, in order to understand the impact of the $\mathcal{R}_{D^*}$, we have also done an analysis considering only the data on $\mathcal{R}_{D^*}$ (table 5.7). It shows that all of $\mathcal{O}^\ell_{V_1}$, $\mathcal{O}^\ell_T$, $\mathcal{O}^\ell_{V_2}$, $\mathcal{O}^\ell_{S_1}$ and $\mathcal{O}^\ell_{S_2}$ are allowed by the criterion $\Delta\text{AIC}_c \leq 4$. However, the constraints from $\mathcal{B}(B_c \to \tau\nu_\tau)$ disfavours the scenarios with scalar operators. As can be seen across all the tables, our conclusions will not change much if we incorporate $\mathcal{R}_{J/\psi}$ as input in our fit. This could be due to the large uncertainties present both in the predictions and measured values of $\mathcal{R}_{J/\psi}$.

After ensuring that we are dealing only with the scenarios allowed by ΔAIC_c, as well as constraints, we estimate the values of the parameters along with their uncertainties.

Data without $\mathcal{R}_{J/\Psi}$						
Scenario	$\mathcal{A}_{FB}$	$\mathcal{R}_{J/\Psi}$	$\mathcal{R}^{\mu}_{\Lambda}$	$\mathcal{R}^{e}_{\Lambda}$	$\mathcal{A}^{\lambda}_{FB}$	$\mathcal{B}(B_c \to \tau\nu) \times 10^2$
1	0.4400(0)(11)	0.201(17)(10)	0.462(18)(18)	0.460(18)(18)	0.1674(0)(48)	2.08(18)(0)
2	0.3586(3)(0)	0.348(34)(14)	0.397(16)(16)	0.396(16)(16)	0.0231(0)(0)	2.51(21)(10)
6	0.3489(3)(116)	0.339(33)(16)	0.401(16)(17)	0.400(16)(17)	0.0273(0)(45)	1.31(11)(110)
7	0.3124(4)(128)	0.348(35)(18)	0.406(17)(18)	0.405(17)(18)	0.0434(0)(30)	0.15(1)(30)
8	0.3053 (4)(144)	0.343(34)(17)	0.400(16)(16)	0.399(16)(16)	0.0318(0)(20)	0
9	0.3233(3)(70)	0.353(36)(18)	0.418(17)(21)	0.417(17)(21)	0.0614(0)(70)	1.35(11)(25)
10	0.3164(3)(114)	0.348(34)(18)	0.404(16)(17)	0.402(16)(17)	0.0608(0)(78)	6.21(53)(194)
11	0.3142 (4)(120)	0.344(33)(17)	0.398(16)(16)	0.397(16)(16)	0.0573(0)(76)	8.90(76)(213)
12	0.3468(3)(137)	0.340(33)(16)	0.400(16)(16)	0.399(16)(16)	0.0370(0)(141)	4.24(36)(205)
13	0.3586(3)(0)	0.338(33)(17)	0.402(16)(17)	0.400(16)(17)	0.0251(0)(26)	2.43(20)(13)
14	0.3586(3)(0)	0.338(33)(17)	0.402(16)(17)	0.400(16)(17)	0.0889(0)(172)	2.43(20)(13)
15	0.3672(2)(93)	0.332(32)(23)	0.398(16)(16)	0.397(16)(16)	0.0151(0)(77)	2.72(23)(26)
16	0.4290(0)(272)	0.225(19)(58)	0.450(17)(33)	0.449(17)(33)	0.1512(0)(400)	2.08(18)(0)

TABLE 5.14: Prediction of observables, continued from table 5.13.

$\mathcal{R}_{X_c}$ (SM + NP) for Data without $\mathcal{R}_{J/\Psi}$				
Scenario	m_c in scheme:			
	$\overline{MS}$		Kinetic	
	NNLO + $\mathcal{O}(1/m_b^2)$	NNLO + $\mathcal{O}(1/m_b^3)$	NNLO + $\mathcal{O}(1/m_b^2)$	NNLO + $\mathcal{O}(1/m_b^3)$
1	0.410(19)	0.387(19)	0.395(18)	0.372(18)
3	0.281(10)	0.258(10)	0.2741(98)	0.2511(98)
7	0.283(10)	0.260(10)	0.276(10)	0.253(10)
8	0.298(14)	0.275(14)	0.291(14)	0.268(14)
9	0.287(11)	0.264(11)	0.280(11)	0.257(11)
10	0.317(19)	0.294(19)	0.309(19)	0.286(19)
11	0.296(14)	0.273(14)	0.289(13)	0.266(13)
12	0.288(11)	0.265(11)	0.281(11)	0.258(11)
13	0.283(10)	0.260(10)	0.276(10)	0.253(10)
14	0.281(10)	0.258(10)	0.2743(99)	0.2513(99)
15	0.301(15)	0.278(15)	0.293(14)	0.270(14)
16	0.275(11)	0.252(11)	0.268(11)	0.245(11)
17	0.392(48)	0.369(48))	0.378(45)	0.356(45)

TABLE 5.15: Predictions for $\mathcal{R}_{X_c}$, in different NP scenarios (same as table 5.13). Here, the mentioned accuracy levels are for the SM predictions. Two sets of calculations are done with m_c in either $\overline{MS}$ or kinetic scheme. The corresponding SM predictions are given in table 5.3. Quoted uncertainties are for NP only. The SM uncertainties are to be added in quadrature to respective cases.

Ideally, these would be obtained from the projections of the $\Delta\chi^2 = 1$ regions on the parameter line [2]. For simplicity, and to avoid asymmetric uncertainties, we consider a parabolic approximation around the chosen minimum and not only obtain the uncertainties of all parameters for each case, but also the correlation between them in the 2 parameter cases. These results are tabulated in tables 5.9, 5.10, 5.11 and 5.12. For some scenarios, instead of the results, the reader is asked to check the corresponding plots. In these scenarios, the best fit, instead of being an isolated point, is actually a contour in the parameter-space. Figure 5.2g is such an example. We note that we do not need large values of the C_Ws (< 1) to explain the observed discrepancies in general. Among the best possible scenarios, the data is more sensitive to the model with operator $\mathcal{O}^{\ell}_{V_1}$ (with real C_W) or $\mathcal{O}^{\ell}_{V_2}$ (with complex C_W) than the one with operator $\mathcal{O}^{\ell}_{T}$. From the best fit values we note that $\mathcal{R}e(C_{V_2}) < \mathcal{R}e(C_{V_1}) << \mathcal{R}e(C_T) < 1$.

These results could be used by model builders to effectively put bounds on the parameter space of their lepton-flavour universality violating model, satisfying $b \to c\ell\nu$ transitions.

5.4.2 Prediction of observables and correlations amongst them

Using these NP results, we have predicted the values of the observables listed in table 5.1. Our predictions for all pertinent scenarios for the dataset without $\mathcal{R}_{J/\Psi}$ are listed in tables 5.13 and 5.14. Predictions for the inclusive ratio $\mathcal{R}_{X_c}$ are given in a separate table (table 5.15).

All of the predicted values for NP show deviations from their respective SM predictions. Moreover, neither all observables are equally deviated for a particular type of NP scenario, nor a single observable has similar deviations for different types of NP scenarios. Therefore, in trying to explain the deviations in $\mathcal{R}_{D^{(*)}}$ for a specific type of NP, we get information about the expected deviations in other associated observables. The obtained patterns then can be compared with the future measurements of these observables for a consistency check of the SM and to look for the types of NP. Any result, inconsistent with SM, but consistent with a future prediction of some observable, could be an indirect

---

[2] For an illustration with the one parameter case, check figure 5.1c, where there are two minima. Only one of them is the global minimum and the end points of the red projection region on the parameter line gives the 1σ uncertainty. There is another region allowed by 3σ around the other local minimum, coloured in blue.

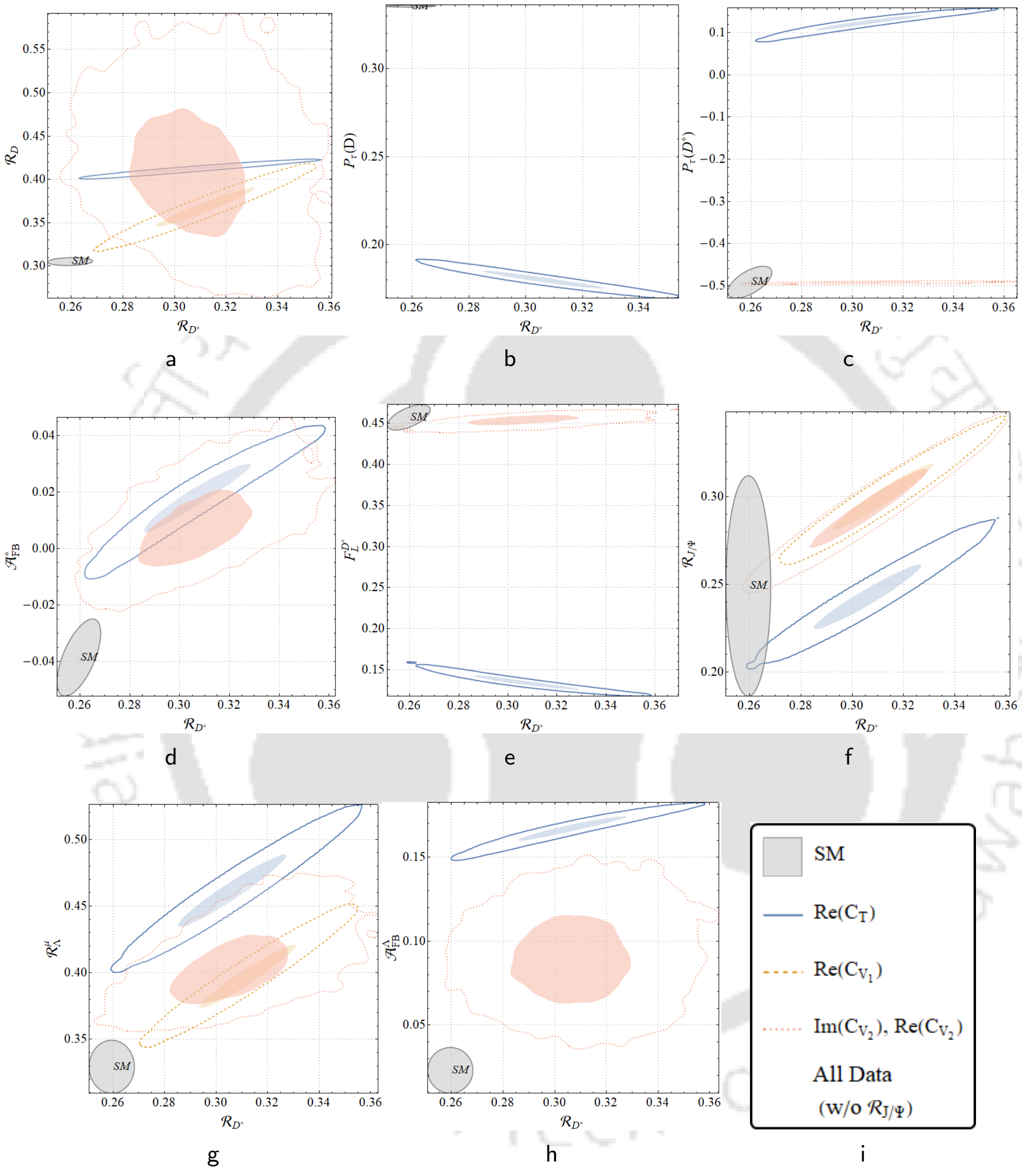

Fig. 5.3 Correlation plots among different observables for one-operator scenarios listed in the first column of Table 5.9. Blue (solid), Orange(dashed), and Red(dotted) contours correspond to the scenarios with $\mathcal{R}e(C_T)$, $\mathcal{R}e(C_{V_1})$, and complex C_{V_2} respectively. For each of these scenarios, 1σ (filled region) and 3σ contours are given.

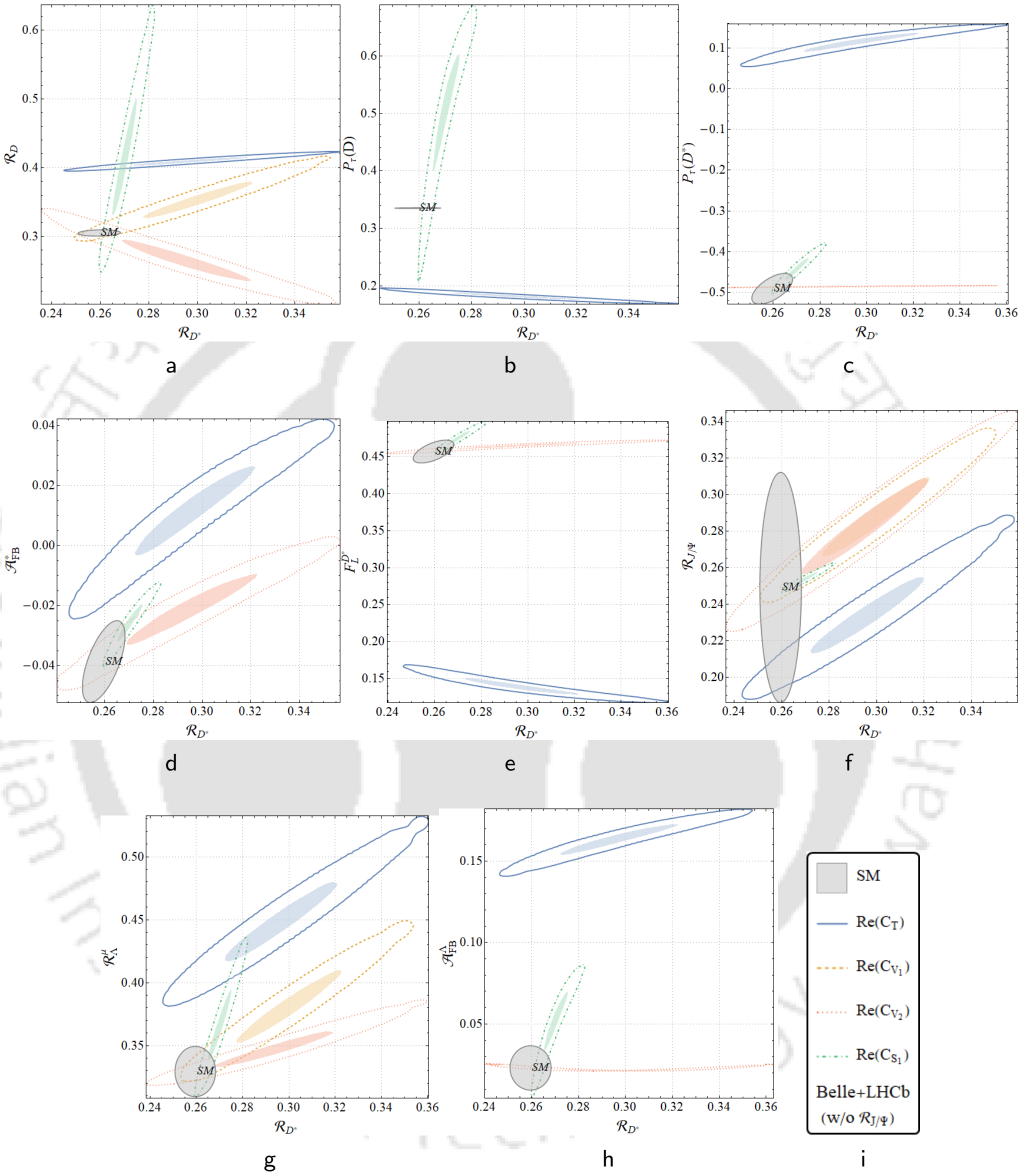

a b c

d e f

g h i

Fig. 5.4 Correlation plots among different observables for all one-operator scenarios listed in the first column of Table 5.11. Blue (solid), Orange (dashed), Red(dotted), and Green (dot-dashed) contours correspond to the scenarios with $\mathcal{R}e(C_T)$, $\mathcal{R}e(C_{V_1})$, $\mathcal{R}e(C_{V_2})$, and $\mathcal{R}e(C_{S_1})$ respectively. For each of these scenarios, 1σ (filled region) and 3σ contours are given.

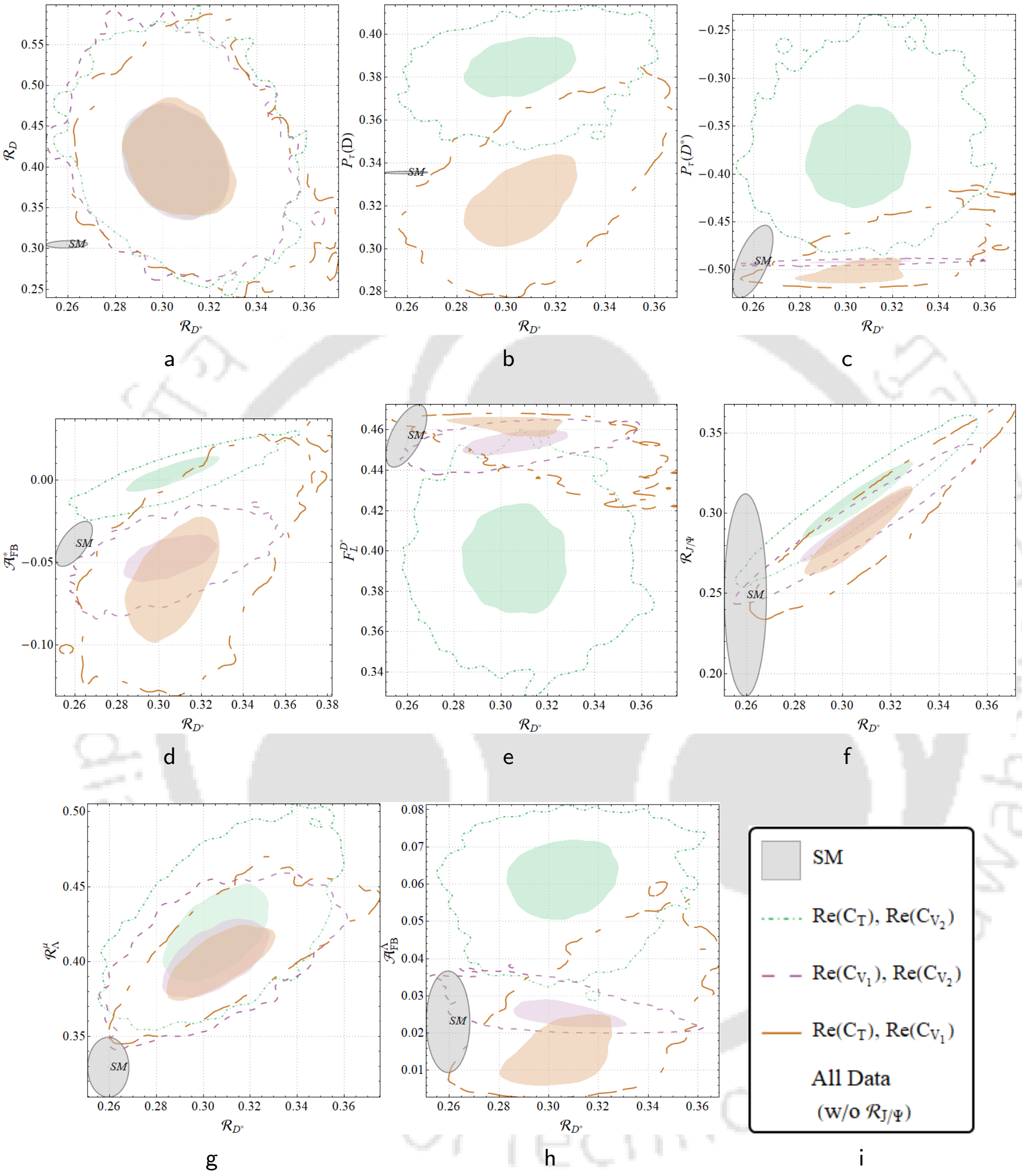

Fig. 5.5 Correlation plots among different observables for some of the two-operator scenarios listed in the first column of Table 5.9. Green (dot-dashed), Magenta (dashed) and Brown (non-uniform dot-dashed) contours correspond to the scenarios with $[\mathcal{R}e(C_T), \mathcal{R}e(C_{V_2})]$, $[\mathcal{R}e(C_{V_1}), \mathcal{R}e(C_{V_2})]$ and $[\mathcal{R}e(C_T), \mathcal{R}e(C_{V_1})]$ respectively. For each of these scenarios, 1σ (filled region) and 3σ contours are given.

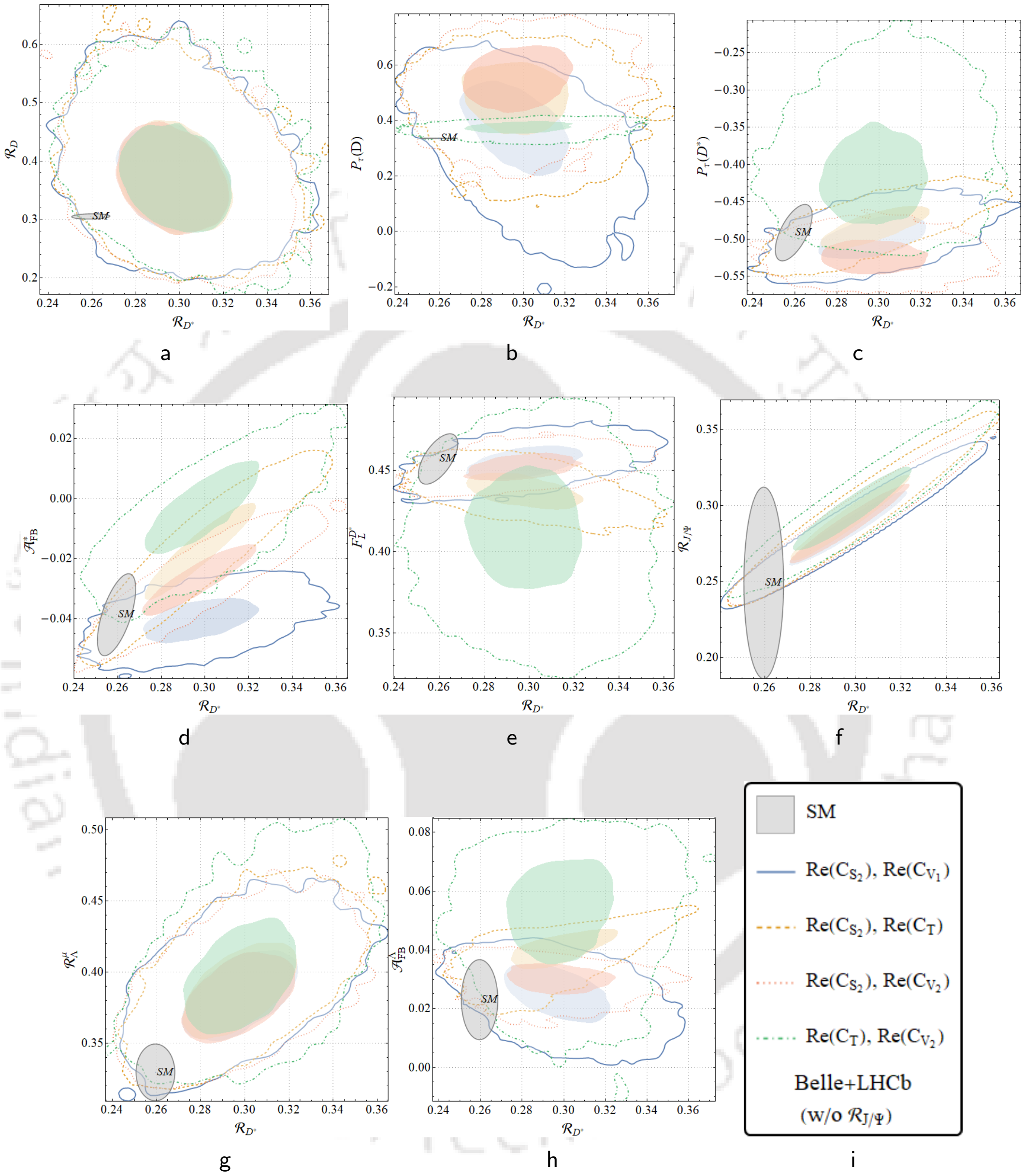

Fig. 5.6 Correlation plots among different observables for two-operator scenarios listed in the first column of Table 5.11. Blue (solid), Orange (dashed), Red(dotted) and Green (dot-dashed) contours correspond to the scenarios with $[\mathcal{R}e(C_{S_2}), \mathcal{R}e(C_{V_1})]$, $[\mathcal{R}e(C_{S_2}), \mathcal{R}e(C_T)]$, $[\mathcal{R}e(C_{S_2}), \mathcal{R}e(C_{V_2})]$ and $[\mathcal{R}e(C_T), \mathcal{R}e(C_{V_2})]$ respectively. For each of these scenarios, 1σ (filled region) and 3σ contours are given.

evidence in support for that specific scenario. In this regard, the correlations between the observables will play an important role. In figs. 5.3, 5.4, 5.5, and 5.6 we have shown the correlations between the various observables in different NP scenarios which are allowed by our model selection criteria. Following points illuminate our findings after scrutinising these plots:

1. Let us first note the very important correlations between $\mathcal{R}_D$ and $\mathcal{R}_{D^*}$ in the scenarios which are allowed by our model selection criteria. In figs. 5.3a and 5.4a, we plot these correlations for the scenarios with one operator at a time, such as $\mathcal{O}^\ell_T$, $\mathcal{O}^\ell_{V_1}$, $\mathcal{O}^\ell_{V_2}$, and $\mathcal{O}^\ell_{S_1}$. We note that in all the scenarios, except the one with $\mathcal{O}^\ell_{V_2}$, the above two observables are positively correlated but the slopes are very different. By looking at the correlations, one can distinguish between the contributions from different NP operators. In the presence of either $\mathcal{R}e(C_{V_1})$, $\mathcal{R}e(C_{V_2})$, or $\mathcal{R}e(C_{S_1})$, if one of the observables is consistent with the SM, then so must be the other. However, in the case of $\mathcal{R}e(C_T)$, there are regions in which $\mathcal{R}_{D^*}$ is consistent with the SM, whereas $\mathcal{R}_D$ is largely deviated from its SM prediction. Therefore, if future data shows that $\mathcal{R}_{D^*}$ is within the SM ballpark but $\mathcal{R}_D$ has a large value above its SM prediction, then any scenario with either $\mathcal{R}e(C_{V_1})$, $\mathcal{R}e(C_{V_2})$ or $\mathcal{R}e(C_{S_1})$ has less chance to explain the data, but one with the operator $\mathcal{O}^\ell_T$ will still be able to explain it. The situation is completely opposite in the case of $\mathcal{R}e(C_{V_2})$, where the enhancement in $\mathcal{R}_{D^*}$ over its SM prediction is associated with a decrease in $\mathcal{R}_D$ from its SM value. On the other hand, the contributions from $\mathcal{O}^\ell_{V_2}$ with complex C_{V_2} will show deviations in both the observables.

2. All the asymmetric and angular observables are insensitive to the operator $\mathcal{O}_{V_1}$, as its effect gets cancelled in the ratios. Thus, if future measurements show deviations only in $\mathcal{R}_D$ and $\mathcal{R}_{D^*}$, and all the other asymmetric and angular observables in $B \to D^{(*)}\tau\nu_\tau$ decays are consistent with their SM values, then the presence of $\mathcal{O}_{V_1}$ can be singled out.

3. On top of this, $P_\tau(D)$ is insensitive to the operator $\mathcal{O}_{V_2}$; detailed correlations can be seen in figs. 5.3b and 5.4b. Therefore, large deviations in $P_\tau(D)$ in future experiments could point to either tensor or scalar operators. Also, a measured value, well above its SM prediction, can only be explained by the scalar operator. On the other hand, if the value is below its SM prediction, then depending on

whether or not there are deviations in $\mathcal{R}_{D^*}$, tensor or scalar operators are favoured. Hence, if future measurements do not see large deviations in $\mathcal{R}_D$ and $P_\tau(D)$, then the presence of a scalar or tensor operator can be ruled out.

4. As explained earlier, the effects of $\mathcal{O}_{V_2}$ can be distinguished from those of the other operators in the $\mathcal{R}_D - \mathcal{R}_{D^*}$ correlations. Further observations about $\mathcal{O}_{V_2}$, which can be seen in figs. 5.3 and 5.4, are as follows:
   - Large deviations in both $\mathcal{R}_D$ and $\mathcal{R}_{D^*}$.
   - $P_\tau(D)$ will be consistent with its SM value.
   - Measured values of $P_\tau(D^*)$ and $F_L(D^*)$ are consistent with their respective SM predictions.
   - The measured value of $\mathcal{A}^*_{FB}$ will be above its SM prediction.

5. Let us accentuate a few other important points here. In figs. 5.3b and 5.3c, we have shown the correlations between $P_\tau(D^{(*)})$ and $\mathcal{R}_{D^*}$. In the presence of a tensor operator $\mathcal{O}_T$, the $\mathcal{R}_{D^*}$ is negatively and positively correlated with $P_\tau(D)$ and $P_\tau(D^*)$, respectively. However, when $\mathcal{R}_{D^*}$ is consistent with the SM, the τ polarization asymmetries will not be consistent with their respective SM predictions. In the presence of C_T, the values of $P_\tau(D)$ and $P_\tau(D^*)$ will be below and above their respective SM predictions, respectively. Also, $P_\tau(D^*)$ can be positive, whereas the SM predicted value is negative. In the same scenario, the correlations of $\mathcal{R}_{D^*}$ with $\mathcal{A}^*_{FB}$ and $F_L(D^*)$ are similar to those obtained for $P_\tau(D^*)$ and $P_\tau(D)$, respectively, for instances see figs. 5.3d and 5.3e. Also, here the forward-backward and the D^* polarisation asymmetries are largely deviated from their respective SM predictions even when $\mathcal{R}_{D^*}$ is consistent with the SM. On the other hand, we do not see such behaviour in the presence of $\mathcal{O}_{S_1}$. In this case, the $P_\tau(D^{(*)})$, $\mathcal{A}^*_{FB}$ and $F_L(D^*)$ are consistent with their SM predictions depending on whether or not $\mathcal{R}_{D^*}$ is consistent with its SM prediction (see figs. 5.4b, 5.4c, 5.4d and 5.4e).

6. In case of the dataset with only $\mathcal{R}_{J/\psi}$ dropped from the fit, the correlations of $\mathcal{R}_{D^*}$ with other observables like $\mathcal{R}_{J/\psi}$, $\mathcal{R}^\mu_\Lambda$, and A^Λ_{FB} are shown in figs. 5.3f, 5.3g,and 5.3h, respectively. Similar plots, which are obtained by dropping the BABAR data, are given in 5.4f, 5.4g, and 5.4h, respectively. In all the one-operator scenarios, the correlations are positive. Due to the large uncertainty in the SM prediction of $\mathcal{R}_{J/\psi}$, the predicted values of these observables are consistent with its SM prediction in

all these cases. It is difficult to distinguish between the cases with either $\mathcal{R}e(C_{V_1})$, $\mathcal{R}e(C_{V_2})$ or $\mathcal{R}e(C_{S_1})$. A very large deviation in $\mathcal{R}_{D^*}$ may allow us to see a small deviation in $\mathcal{R}_{J/\psi}$. Also, the contribution from $\mathcal{R}e(C_T)$ can be distinguished from other new operators. In a high precision experiment, contributions of various above mentioned operators are separable from each other by observing the correlation between $\mathcal{R}_\Lambda^\mu$ and $\mathcal{R}_{D^*}$. The contribution from $\mathcal{R}e(C_T)$ may allow a large deviation in $\mathcal{R}_\Lambda^\mu$, with a sizeable effect in $\mathcal{R}_{D^*}$. Similar patterns are observed in the correlations of A_{FB}^Λ.

7. Similar correlations in the allowed two-operator scenarios are shown in figs. 5.5 and 5.6. We note that it will be hard to distinguish the allowed two-operator scenarios from each other just from the correlations of $\mathcal{R}_{D^*}$ with $\mathcal{R}_D$, $\mathcal{R}_{J/\psi}$, and $\mathcal{R}_\Lambda^\mu$, as all the scenarios have similar correlations. However, the shape of the confidence regions the two-operator scenarios are different from those of the one-operator ones.

   For the two operator scenarios containing $\mathcal{O}_{V_1}$, the NP-predicted values of the angular and asymmetric observables are consistent with their SM values in general. Here too the $P_\tau(D)$ is insensitive to the operator-combination $[\mathcal{O}_{V_1}, \mathcal{O}_{V_2}]$. We note that the contributions from $[\mathcal{R}e(C_T),\ \mathcal{R}e(C_{V_2})]$ in $P_\tau(D^*)$, $\mathcal{A}_{FB}^*$ and $F_L(D^*)$ can be identified. It is hard to distinguish the contributions of the rest of the operators with $\mathcal{O}_{S_2}$ and all the asymmetric and angular observables are consistent with their respective SM values for them. The correlation of A_{FB}^Λ shows that except the contribution from $[\mathcal{R}e(C_T),\ \mathcal{R}e(C_{V_2})]$, all other allowed two-operator scenarios are consistent with the SM even if there is a large deviation in $\mathcal{R}_{D^*}$. By looking at these correlations, one will be able to distinguish a two-operator scenario from the one-operator ones.

5.5 Summary

In this chapter, we have predicted the SM values of the angular observables associated with the $B \to D^{(*)}\tau\nu_\tau$ decays, following the results of an earlier up-to-date analysis on $B \to D^{(*)}\ell\nu_\ell$. Also, we have updated the SM prediction of $\mathcal{R}_{X_c}$ using the results of [99] along with the proper correlations between the various non-perturbative parameters and masses. These predictions are based on two different schemes of the charm quark mass ($\overline{MS}$ and Kinetic). These include the NNLO perturbative corrections, and power-corrections up to order $1/m_b{}^3$. We have separately mentioned results with power-corrections up to $1/m_b{}^2$ order as well.

In the next part of our analysis, we have analysed the semitaunic $b \to c\tau\nu_\tau$ decays in a model independent framework with the $\Delta B = \Delta C = 1$ semileptonic operators. We have included the complete set of vector, scalar and tensor operators, while assuming the neutrinos to be left handed. Different possible combinations of all the effective operators have been considered, and following AIC$_c$, the combinations, which are best suited for the available data, are considered for further studies. We have performed the analysis on several different prepared data sets. We note that for all of the data sets, the one-operator scenarios, with a real C_W, can best explain the available data. However, in most of them, the scalar operators are not allowed by the constraint $Br(B_c \to \tau\nu_\tau) \leq 30\%$. The most favoured scenarios are the ones with tensor ($\mathcal{O}_T$) or $(V-A)$ ($\mathcal{O}_{V_1}$) type of operators. Also, the $(V+A)$ type of interactions, with a complex C_W, though less favoured, are allowed. In the absence of the BABAR data on $\mathcal{R}_{D^{(*)}}$ from our analysis, one-operator scenarios like $(V \pm A)$, $S-P$, and tensor operators with real C_W are the most favoured ones. These one operator scenarios are easily distinguishable from each other by studying the correlations of $\mathcal{R}_{D^*}$ with $\mathcal{R}_D$ and all the other asymmetric and angular observables. Also, the patterns of the future measurements of all such observables can easily discriminate the types of NP. Among all the possible combinations of $(V \pm A)$, tensor and $(S-P)$ operators, there are quite a few two-operator scenarios which pass all the selection criteria. In these cases, one cannot differentiate between the contributions from NP scenarios by looking at the correlations of $\mathcal{R}_{D^*}$ with $\mathcal{R}_D$, $\mathcal{R}_{J/\psi}$, and $\mathcal{R}^\mu_\Lambda$. However, the correlations of $\mathcal{R}_{D^*}$ with the various angular and asymmetric observables could be useful for such a discrimination. We have also predicted the numerical values of all the observables along with their errors, for the allowed scenarios.

Chapter 6

Summary and Conclusions

The compelling signatures of the insufficiency of the SM has prescribed us to extend the theory further to consolidate all the observed phenomena in nature. In absence of any direct detection of new particle at the collider experiments, the precision measurements in the flavour sector play a very important role to explore the possibility of new physics. Over the last few years, some intriguing anomalies have been found in different channels of B meson decay. In this thesis, we have analysed semitaunic $b \to c$ inclusive and exclusive decays in order to identify the signature of new physics from the mismatch of the experimental data with SM predictions. Due to the large mass of τ, the helicity suppression is less for semitaunic decays with respect to the other with light leptons (e and μ) in the final state. Moreover, for $B \to D^* \tau \nu_\tau$ decay, we have two detectable particles with nonzero spin in the final state (D^*, τ). These are the main advantages to investigate the structure of possible NP contribution for $b \to c\tau\nu_\tau$ transitions.

Theoretically, the prospect of NP in these decays has been discussed in several literatures, some of which are based on specific NP models. Other studies follow a model-independent approach, in which a general effective Hamiltonian for the transition including non-SM operators is imposed to explore the impact of various NP scenarios on different physical observables. In our analysis, using the model independent approach, we first try to identify specific observables suitable for the extraction of a particular type of NP coupling with optimal observable technique. Secondly, we perform a separate analysis to point out which type of NP interaction(s) can best explain and elucidate(s) the current experimental data in $b \to c\tau\nu_\tau$ decay using Akaike Information Criteria.

In this chapter, we present a brief summary of the works carried out in this thesis, whereas in Section 3.4, Section 4.4, and Section 5.5 we have presented a detailed summery of all our works separately.

In Chapter 1, we first present a very brief review of flavor symmetry in SM, different properties of CKM matrix and Unitary triangles. Thenceforth we describe the importance of semileptonic B decays to extract the CKM matrix elements $|V_{ub}|$ and $|V_{cb}|$ and to understand the origin of CP violation in SM. With a short review of the phenomenon of Lepton flavor Universality violation we then discuss how it can play an important role to identify the possible signature of new physics beyond SM. Thereafter a discussion on the current experimental status of several observables in $b \to c\tau\nu_\tau$ decays are presented. We end this chapter with a concise discussion on the deviation of experimental results with the SM predictions of these observables. All these things together sets the background for the studies performed in the thesis.

In Chapter 2, We make a pitch for the statistical methods used in our study to identify the possible new physics effects in semitaunic decays of B meson. These methods are the tools needed to compare data with theory and quantify the extent to which one stands in agreement with the other.

In the first part of this chapter, we present a detailed discussion on the Optimal Observable technique. With this procedure we can systematically estimate the statistical uncertainties of the measurable parameters, which in turn will help us to identify the observable that shows its maximal sensitivity to a particular type of NP structure. In the next part, we introduce the concepts and general framework of data based model selection with an information theoretic approach to identify the new interactions which can best explain the available data. At the end of this chapter an introductory idea of the Akaike Information Criterion for model selection is discussed.

In Chapter 3, we look for all possible observables in $B \to D^{(*)}\tau\nu_\tau$ with NP, including new vector, scalar and tensor interactions, and investigate the prospects of extracting NP Wilson coefficients with Optimal Observables analysis. Using this technique one can estimate, with what significance some observable may differentiate a particular type of NP from the SM. In our analysis, we consider the q^2 distribution of differential branching fractions, $R(D^{(*)})$, the τ polarisation asymmetries, forward backward asymmetries of the decay $B \to D^{(*)}\tau\nu_\tau$, and D^* polarisation asymmetry, as relevant observables.

From our numerical study, we find that in $B \to D\tau\nu_\tau$ channel, it would be hard to decide what type of new interaction will show the maximum sensitivity. However, from the analysis of the q^2 distribution of the decay rate, we find that the low q^2 region is more sensitive to scaler interaction whereas for the high q^2 region it is the tensor interaction . The overall sensitivity of the observables in $B \to D^*\tau\nu_\tau$ is more towards tensor interactions. If we switch off the tensor operator from the analysis, the real part of both the vector and scalar wilson coefficients are equally sensitive for this decay. The analysis of the q^2 distributions of the decay rate shows distinct regions of q^2, which are sensitive to vector, scalar, and tensor interactions respectively. These information are lost in the full q^2 integrated observables. Nonetheless, the present data on different bins do not have sufficient statistics to conclude anything, more precise data could help us to pinpoint the type of NP interaction. Therefore, our suggestion to the experimentalists is to give more priority to gain more statistics at those regions of q^2.

In Chapter 4, we study the decays $B \to D^{(*)}\tau\nu_\tau$ in light of the available data from BABAR, Belle and LHCb. This analysis is systematically divided in two parts. In the first part, the form-factors, relevant in these decays, are fitted assuming the absence of any contribution coming from NP operators. The fitted results are then compared with those obtained by HFAG from the analysis with the available data on $B \to D^{(*)}\ell\nu_\ell$. In the next part of this study, we consider the new physics contributions only in $B \to D^{(*)}\tau\nu_\tau$ decays. In this case, the relevant form-factors are taken from the fit results by HFAG. Different possible NP scenarios are defined by considering all possible combinations of the new operators in many different ways. To obtain a data-based selection of a best case and to rank and weigh the remaining cases from a multi-scenario analysis, we here use the information-theoretic approaches, especially of AIC_c in the analysis of empirical data. Such procedures lead to more robust inferences in simultaneous comparative analysis of multiple competing scenarios. Traditional statistical inference like confidence levels, errors on fit parameters,bias and variance can then be obtained based on the selected best models.

Our analysis of the available binned data on $R(D^*)$ from BABAR, Belle, and LHCb shows that the most plausible explanation of these data can be obtained from the presence of new effective operators with left or right handed charged vector current. In addition, if we include $R(D)$ in our fit, apart from the vector currents, the contributions from charged scalar currents might become relevant, either alone or along with right handed vector current operators.

In Chapter 5, we have updated the SM predictions of all possible asymmetric and angular observables in $B \to D^{(*)}\tau\nu_\tau$ decays, using the results of the newly revised analysis in $B \to D^{(*)}\ell\nu_\ell$. We here also consider a few other $b \to c\tau\nu_\tau$ decay modes like $B_c \to \tau\nu_\tau$, $\Lambda_b \to \Lambda_c\tau\nu_\tau$ and the inclusive decay $B \to X_c\tau\nu_\tau$, which are potentially sensitive to the new interactions present in the observables in $B \to D^{(*)}\tau\nu_\tau$ decays. Hence, we have studied the correlation of the various observables associated with these decay modes which will be an important probe for an indirect detection of NP. Our study also predicts the values of all the relevant observables for the above mentioned decay modes, which can further be used to check for consistency with the future measurements.

It is mentioned earlier that the binned data used in the analysis described in chapter 4, contain large error which in turn cause large errors in our fitted results. Hence, following the same methodology of our previous work, here we also perform a data based model selection analysis with the experimentally available results on the charged current anomalies in conjunction with other relevant results. Additionally, the constraint from the decay of $B_c \to \tau\nu_\tau$ is taken into account in this analysis. Though this channel is out of the experimental reach for now, it can be used as an effective constraint on any NP effects that could potentially explain the $R(D^{(*)})$ excess. A conservative upper limit quoted for $\mathcal{B}(B_c \to \tau\nu_\tau)$, even after adding NP effect is $\lesssim 30\%$. A stronger upper bound of $\lesssim 10\%$ is obtained from LEP data taken at Z-peak with a prospect of an even tighter bound from the full L3 data. In our analysis we have used both of these constraints.

After ensuring that we are dealing only with the scenarios allowed by ΔAIC_c, and constraints from $B_c \to \tau\nu_\tau$, we estimate the values of the NP parameters along with their uncertainties. In most of the cases, the scalar operators are not allowed by the constraint $\mathcal{B}(B_c \to \tau\nu_\tau) \lesssim 30\%$. The most favoured scenarios are the ones with tensor $(\mathcal{O}_T)$ or $(V-A)(\mathcal{O}_{V_1})$ type of operators. In the absence of the BABAR data on $R(D^*)$ from our analysis, one-operator scenarios like $(V \pm A)$, $S-P$, and tensor operators with real CW are the most favoured ones. These one operator scenarios are easily distinguishable from each other by studying the correlations of $R(D^*)$ with $R(D)$ and all the other asymmetric and angular observables. Also, the obtained patterns then can be compared with the future measurements of these observables for a consistency check of the SM and to look for the types of NP. Finally, we also predict the numerical values of all the observables along with their errors, for the allowed scenarios.

In brief, the thesis mainly explores the following aspects.

- We have tried to identify the NP structure that can be best extracted from a particular observable, with reasonable statistics. To achieve this goal the Optimal Observable technique is used.

  In general, the sensitivity to various NP interactions may be q^2 dependent. Hence, here we also analyze the bin-by-bin q^2 distribution of the differential decay rate of $B \to D^{(*)}\tau\nu_\tau$ to look for more possibilities, and zoom in to the regions of q^2 , within which the sensitivity to a specific type of new interaction is much larger than most other regions. However, because of poor statistics in data it is premature to conclude anything. Therefore, the experimental effort should be in gathering more statistics in specific regions of q^2 potentially sensitive to NP, which may in turn help the clean extraction of NP couplings.

- In a different analysis, we have studied the decays $B \to D^{(*)}\tau\nu_\tau$ in light of the available binned data from BABAR, Belle and LHCb. In the first part of this study, we assume that there is no NP in $B \to D^{(*)}\tau\nu_\tau$, just as in $B \to D^{(*)}\ell\nu_\ell$, and fit the form factors. Different experimental collaborations have already fitted the form-factor parameters from the data collected for the decays of $B \to D^{(*)}\ell\nu_\ell$. However, in the decays of $B \to D^{(*)}\tau\nu_\tau$, there are additional form factors that cannot be extracted directly from the available data on $B \to D^{(*)}\ell\nu_\ell$. Hence, in this study, we extract those additional form factors along with the common form factors for both the channels and check whether the fitted form factors are in good agreement with those obtained from the decay of $B \to D^{(*)}\ell\nu_\ell$. Any discrepancy between the two indicates a possible new effect in $B \to D^{(*)}\tau\nu_\tau$, which is absent in $B \to D^{(*)}\ell\nu_\ell$.

  In the next part of this analysis, we consider the contributions from different NP interactions only in $B \to D^{(*)}\tau\nu_\tau$. Our goal is to search for new interactions that are most compatible with the present data and best elucidates them.

- In our latest work, we have also predicted the SM values of the asymmetric and angular observables in $B \to D^{(*)}\tau\nu_\tau$ decays using the results of the new up-to-date analysis in $B \to D^{(*)}\ell\nu_\ell$. The correlations among these observables are also discussed.These correlations are found to be useful in distinguishing various NP scenarios.

Appendix A

Decay distributions for angular observables in $B \to D^{(*)}\tau\nu_\tau$ decays:

The q^2-distributions for different polarization of τ in $B \to D^{(*)}\tau\nu_\tau$ decays in terms of different helicity amplitudes are given below [67],

$$
\begin{aligned}
\frac{d\Gamma^{\lambda_\tau=1/2}(\bar{B}\to D\tau\bar{\nu}_l)}{dq^2} =& \frac{G_F^2|V_{cb}|^2}{192\pi^3 m_B^3} q^2 \sqrt{\lambda_D(q^2)}\left(1-\frac{m_\tau^2}{q^2}\right)^2 \times \Bigg\{ \\
& \frac{1}{2}|\delta_{l\tau}+C^l_{V_1}+C^l_{V_2}|^2 \frac{m_\tau^2}{q^2}\left(H^{s\,2}_{V,0}+3H^{s\,2}_{V,t}\right) \\
& +\frac{3}{2}|C^l_{S_1}+C^l_{S_2}|^2\, H^{s\,2}_S + 8|C^l_T|^2\, H^{s\,2}_T \\
& +3Re[(\delta_{l\tau}+C^l_{V_1}+C^l_{V_2})(C^{l*}_{S_1}+C^{l*}_{S_2})]\frac{m_\tau}{\sqrt{q^2}}\, H^s_S H^s_{V,t} \\
& -4Re[(\delta_{l\tau}+C^l_{V_1}+C^l_{V_2})C^{l*}_T]\frac{m_\tau}{\sqrt{q^2}}\, H^s_T H^s_{V,0} \Bigg\},
\end{aligned}
\tag{A.1a}
$$

$$
\begin{aligned}
\frac{d\Gamma^{\lambda_\tau=-1/2}(\bar{B}\to D\tau\bar{\nu}_l)}{dq^2} =& \frac{G_F^2|V_{cb}|^2}{192\pi^3 m_B^3} q^2 \sqrt{\lambda_D(q^2)}\left(1-\frac{m_\tau^2}{q^2}\right)^2 \times \Bigg\{ \\
& |\delta_{l\tau}+C^l_{V_1}+C^l_{V_2}|^2\, H^{s\,2}_{V,0} + 16|C^l_T|^2 \frac{m_\tau^2}{q^2}\, H^{s\,2}_T \\
& -8\Re[(\delta_{l\tau}+C^l_{V_1}+C^l_{V_2})C^{l*}_T]\frac{m_\tau}{\sqrt{q^2}}\, H^s_T H^s_{V,0} \Bigg\},
\end{aligned}
\tag{A.1b}
$$

$$
\begin{aligned}
\frac{d\Gamma^{\lambda_\tau=1/2}(\bar{B}\to D^*\tau\bar{\nu}_l)}{dq^2} = {} & \frac{G_F^2|V_{cb}|^2}{192\pi^3 m_B^3} q^2 \sqrt{\lambda_D^*(q^2)} \left(1-\frac{m_\tau^2}{q^2}\right)^2 \times \Bigg\{ \\
& \frac{1}{2}(|\delta_{l\tau}+C_{V_1}^l|^2+|C_{V_2}^l|^2)\frac{m_\tau^2}{q^2}\left(H_{V,+}^2+H_{V,-}^2+H_{V,0}^2+3H_{V,t}^2\right) \\
& -\Re[(\delta_{l\tau}+C_{V_1}^l)C_{V_2}^{l*}]\frac{m_\tau^2}{q^2}\left(H_{V,0}^2+2H_{V,+}H_{V,-}+3H_{V,t}^2\right) \\
& +\frac{3}{2}|C_{S_1}^l-C_{S_2}^l|^2\,H_S^2+8|C_T^l|^2\left(H_{T,+}^2+H_{T,-}^2+H_{T,0}^2\right) \\
& +3\Re[(\delta_{l\tau}+C_{V_1}^l-C_{V_2}^l)(C_{S_1}^{l*}-C_{S_2}^{l*})]\frac{m_\tau}{\sqrt{q^2}}\,H_S H_{V,t} \\
& -4\Re[(\delta_{l\tau}+C_{V_1}^l)C_T^{l*}]\frac{m_\tau}{\sqrt{q^2}}\left(H_{T,0}H_{V,0}+H_{T,+}H_{V,+}-H_{T,-}H_{V,-}\right) \\
& +4\Re[C_{V_2}^l C_T^{l*}]\frac{m_\tau}{\sqrt{q^2}}\left(H_{T,0}H_{V,0}+H_{T,+}H_{V,-}-H_{T,-}H_{V,+}\right)\Bigg\},
\end{aligned}
\tag{A.2a}
$$

$$
\begin{aligned}
\frac{d\Gamma^{\lambda_\tau=-1/2}(\bar{B}\to D^*\tau\bar{\nu}_l)}{dq^2} = {} & \frac{G_F^2|V_{cb}|^2}{192\pi^3 m_B^3} q^2 \sqrt{\lambda_D^*(q^2)} \left(1-\frac{m_\tau^2}{q^2}\right)^2 \times \Bigg\{ \\
& (|\delta_{l\tau}+C_{V_1}^l|^2+|C_{V_2}^l|^2)\left(H_{V,+}^2+H_{V,-}^2+H_{V,0}^2\right) \\
& -2\Re[(\delta_{l\tau}+C_{V_1}^l)C_{V_2}^{l*}]\left(H_{V,0}^2+2H_{V,+}H_{V,-}\right) \\
& +16|C_T^l|^2\frac{m_\tau^2}{q^2}\left(H_{T,+}^2+H_{T,-}^2+H_{T,0}^2\right) \\
& -8\Re[(\delta_{l\tau}+C_{V_1}^l)C_T^{l*}]\frac{m_\tau}{\sqrt{q^2}}\left(H_{T,0}H_{V,0}+H_{T,+}H_{V,+}-H_{T,-}H_{V,-}\right) \\
& +8\Re[C_{V_2}^l C_T^{l*}]\frac{m_\tau}{\sqrt{q^2}}\left(H_{T,0}H_{V,0}+H_{T,+}H_{V,-}-H_{T,-}H_{V,+}\right)\Bigg\},
\end{aligned}
\tag{A.2b}
$$

For the fixed polarization of D^*, the distributions are given by

$$\begin{aligned}\frac{d\Gamma^{\lambda_{D^*}=\pm1}(\bar{B}\to D^*\tau\bar{\nu}_l)}{dq^2} =& \frac{G_F^2|V_{cb}|^2}{192\pi^3 m_B^3} q^2\sqrt{\lambda_{D^*}(q^2)}\left(1-\frac{m_\tau^2}{q^2}\right)^2 \times \Bigg\{\\ & \left(1+\frac{m_\tau^2}{2q^2}\right)\Big(|\delta_{l\tau}+C^l_{V_1}|^2 H^2_{V,\pm} + |C^l_{V_2}|^2 H^2_{V,\mp}\\ & - 2\Re[(\delta_{l\tau}+C^l_{V_1})C^{l*}_{V_2}]H_{V,+}H_{V,-}\Big)\\ & + 8|C^l_T|^2\left(1+\frac{2m_\tau^2}{q^2}\right)H^2_{T,\pm}\\ & \mp 12\Re[(\delta_{l\tau}+C^l_{V_1})C^{l*}_T]\frac{m_\tau}{\sqrt{q^2}}H_{T,\pm}H_{V,\pm}\\ & \pm 12\Re[C^l_{V_2}C^{l*}_T]\frac{m_\tau}{\sqrt{q^2}}H_{T,\pm}H_{V,\mp}\Bigg\},\end{aligned} \tag{A.3a}$$

$$\begin{aligned}\frac{d\Gamma^{\lambda_{D^*}=0}(\bar{B}\to D^*\tau\bar{\nu}_l)}{dq^2} =& \frac{G_F^2|V_{cb}|^2}{192\pi^3 m_B^3} q^2\sqrt{\lambda_{D^*}(q^2)}\left(1-\frac{m_\tau^2}{q^2}\right)^2 \times\\ & \Bigg\{|\delta_{l\tau}+C^l_{V_1}-C^l_{V_2}|^2\left[\left(1+\frac{m_\tau^2}{2q^2}\right)H^2_{V,0}+\frac{3}{2}\frac{m_\tau^2}{q^2}H^2_{V,t}\right]\\ & + \frac{3}{2}|C^l_{S_1}-C^l_{S_2}|^2\,H_S^2 + 8|C^l_T|^2\left(1+\frac{2m_\tau^2}{q^2}\right)H^2_{T,0}\\ & + 3\Re[(\delta_{l\tau}+C^l_{V_1}-C^l_{V_2})(C^{l*}_{S_1}-C^{l*}_{S_2})]\frac{m_\tau}{\sqrt{q^2}}\,H_S H_{V,t}\\ & - 12\Re[(\delta_{l\tau}+C^l_{V_1}-C^l_{V_2})C^{l*}_T]\frac{m_\tau}{\sqrt{q^2}}H_{T,0}H_{V,0}\Bigg\}.\end{aligned} \tag{A.3b}$$

Decay distribution of $b_\theta^{(D^{(*)})}$ to define $\mathcal{A}_{\rm FB}^{(*)}$ in Eq. (1.43)

$$\begin{aligned}
b_\theta^{(D)}(q^2) =& \frac{G_F^2 |V_{cb}|^2}{128\pi^3 m_B^3} q^2 \sqrt{\lambda_D(q^2)} \left(1 - \frac{m_\tau^2}{q^2}\right)^2 \times \Bigg\{ \\
& |\delta_{l\tau} + C_{V_1}^l + C_{V_2}^l|^2 \frac{m_\tau^2}{q^2} H_{V,0}^s H_{V,t}^s \\
& + Re[(\delta_{l\tau} + C_{V_1}^l + C_{V_2}^l)(C_{S_1}^{l*} + C_{S_2}^{l*})] \frac{m_\tau}{\sqrt{q^2}} H_S^s H_{V,0}^s \\
& - 4Re[(\delta_{l\tau} + C_{V_1}^l + C_{V_2}^l) C_T^{l*}] \frac{m_\tau}{\sqrt{q^2}} H_T^s H_{V,t}^s \\
& - 4Re[(C_{S_1}^l + C_{S_2}^l) C_T^{l*}] \, H_T^s H_S^s \Bigg\},
\end{aligned} \tag{A.4a}$$

$$\begin{aligned}
b_\theta^{(D^*)}(q^2) =& \frac{G_F^2 |V_{cb}|^2}{128\pi^3 m_B^3} q^2 \sqrt{\lambda_{D^*}(q^2)} \left(1 - \frac{m_\tau^2}{q^2}\right)^2 \times \\
& \Bigg\{ \frac{1}{2} (|\delta_{l\tau} + C_{V_1}^l|^2 - |C_{V_2}^l|^2) \left(H_{V,+}^2 - H_{V,-}^2\right) + |\delta_{l\tau} + C_{V_1}^l - C_{V_2}^l|^2 \frac{m_\tau^2}{q^2} H_{V,0} H_{V,t} \\
& + 8 |C_T^l|^2 \frac{m_\tau^2}{q^2} \left(H_{T,+}^2 - H_{T,-}^2\right) + \Re[(\delta_{l\tau} + C_{V_1}^l - C_{V_2}^l)(C_{S_1}^{l*} - C_{S_2}^{l*})] \frac{m_\tau}{\sqrt{q^2}} H_S H_{V,0} \\
& - 4\Re[(\delta_{l\tau} + C_{V_1}^l) C_T^{l*}] \frac{m_\tau}{\sqrt{q^2}} \left(H_{T,0} H_{V,t} + H_{T,+} H_{V,+} + H_{T,-} H_{V,-}\right) \\
& + 4\Re[C_{V_2}^l C_T^{l*}] \frac{m_\tau}{\sqrt{q^2}} \left(H_{T,0} H_{V,t} + H_{T,+} H_{V,-} + H_{T,-} H_{V,+}\right) \\
& - 4\Re[(C_{S_1}^l - C_{S_2}^l) C_T^{l*}] H_{T,0} H_S \Bigg\}.
\end{aligned} \tag{A.4b}$$

Appendix B

Helicity amplitudes for $\Lambda_b \to \Lambda_c \tau \nu_\tau$ decay

The scalar and pseudo-scalar helicity amplitudes associated with the new physics scalar and pseudo-scalar operators are [85]

$$H^{SP}_{1/2,0} = F_0 g_S \frac{\sqrt{Q_+}}{m_b - m_c}(m_{\Lambda_b} - m_{\Lambda_c}) - G_0 g_P \frac{\sqrt{Q_-}}{m_b + m_c}(m_{\Lambda_b} + m_{\Lambda_c}), \tag{B.1}$$

$$H^{SP}_{-1/2,0} = F_0 g_S \frac{\sqrt{Q_+}}{m_b - m_c}(m_{\Lambda_b} - m_{\Lambda_c}) + G_0 g_P \frac{\sqrt{Q_-}}{m_b + m_c}(m_{\Lambda_b} + m_{\Lambda_c}). \tag{B.2}$$

where $g_S = (C_{S_1} + C_{S_2})$ and $g_P = (C_{S_1} - C_{S_2})$.

The parity-related amplitudes are

$$\begin{aligned} H^S_{\lambda_{\Lambda_c},\lambda_{NP}} &= H^S_{-\lambda_{\Lambda_c},-\lambda_{NP}}, \\ H^P_{\lambda_{\Lambda_c},\lambda_{NP}} &= -H^P_{-\lambda_{\Lambda_c},-\lambda_{NP}}. \end{aligned} \tag{B.3}$$

For the vector and axial-vector helicity amplitudes, we have

$$\begin{aligned}
H^{VA}_{1/2,0} &= F_+(1+g_L+g_R)\frac{\sqrt{Q_-}}{\sqrt{q^2}}(m_{\Lambda_b}+m_{\Lambda_c}) \\
&\quad -G_+(1+g_L-g_R)\frac{\sqrt{Q_+}}{\sqrt{q^2}}(m_{\Lambda_b}-m_{\Lambda_c}), && \text{(B.4)} \\
H^{VA}_{1/2,+1} &= -F_\perp(1+g_L+g_R)\sqrt{2Q_-}+G_\perp(1+g_L-g_R)\sqrt{2Q_+}, && \text{(B.5)} \\
H^{VA}_{1/2,t} &= F_0(1+g_L+g_R)\frac{\sqrt{Q_+}}{\sqrt{q^2}}(m_{\Lambda_b}-m_{\Lambda_c}) \\
&\quad -G_0(1+g_L-g_R)\frac{\sqrt{Q_-}}{\sqrt{q^2}}(m_{\Lambda_b}+m_{\Lambda_c}), && \text{(B.6)} \\
H^{VA}_{-1/2,0} &= F_+(1+g_L+g_R)\frac{\sqrt{Q_-}}{\sqrt{q^2}}(m_{\Lambda_b}+m_{\Lambda_c}) \\
&\quad +G_+(1+g_L-g_R)\frac{\sqrt{Q_+}}{\sqrt{q^2}}(m_{\Lambda_b}-m_{\Lambda_c}), && \text{(B.7)} \\
H^{VA}_{-1/2,-1} &= -F_\perp(1+g_L+g_R)\sqrt{2Q_-}-G_\perp(1+g_L-g_R)\sqrt{2Q_+}, && \text{(B.8)} \\
H^{VA}_{-1/2,t} &= F_0(1+g_L+g_R)\frac{\sqrt{Q_+}}{\sqrt{q^2}}(m_{\Lambda_b}-m_{\Lambda_c}) \\
&\quad +G_0(1+g_L-g_R)\frac{\sqrt{Q_-}}{\sqrt{q^2}}(m_{\Lambda_b}+m_{\Lambda_c}). && \text{(B.9)}
\end{aligned}$$

where $g_L = C_{V_1}$ and $g_R = C_{V_2}$.

We also have the relations

$$\begin{aligned}
H^V_{\lambda_{\Lambda_c},\lambda_w} &= H^V_{-\lambda_{\Lambda_c},-\lambda_w}, \\
H^A_{\lambda_{\Lambda_c},\lambda_w} &= -H^A_{-\lambda_{\Lambda_c},-\lambda_w}. && \text{(B.10)}
\end{aligned}$$

The tensor helicity amplitudes are

$$H^{(T)-1/2}_{-1/2,t,0} = -C_T\Big[-h_+\sqrt{Q_-}+\widetilde{h}_+\sqrt{Q_+}\Big], \tag{B.11}$$

$$H^{(T)+1/2}_{+1/2,t,0} = C_T\Big[h_+\sqrt{Q_-}+\widetilde{h}_+\sqrt{Q_+}\Big], \tag{B.12}$$

$$H^{(T)-1/2}_{+1/2,t,+1} = -C_T\frac{\sqrt{2}}{\sqrt{q^2}}\Big[h_\perp(m_{\Lambda_b}+m_{\Lambda_c})\sqrt{Q_-}+\widetilde{h}_\perp(m_{\Lambda_b}-m_{\Lambda_c})\sqrt{Q_+}\Big], \tag{B.13}$$

$$H^{(T)+1/2}_{-1/2,t,-1} = -C_T\frac{\sqrt{2}}{\sqrt{q^2}}\Big[h_\perp(m_{\Lambda_b}+m_{\Lambda_c})\sqrt{Q_-}-\widetilde{h}_\perp(m_{\Lambda_b}-m_{\Lambda_c})\sqrt{Q_+}\Big], \tag{B.14}$$

$$H^{(T)-1/2}_{+1/2,0,+1} = -C_T\frac{\sqrt{2}}{\sqrt{q^2}}\Big[h_\perp(m_{\Lambda_b}+m_{\Lambda_c})\sqrt{Q_-}+\widetilde{h}_\perp(m_{\Lambda_b}-m_{\Lambda_c})\sqrt{Q_+}\Big], \tag{B.15}$$

$$H^{(T)+1/2}_{-1/2,0,-1} = C_T\frac{\sqrt{2}}{\sqrt{q^2}}\Big[h_\perp(m_{\Lambda_b}+m_{\Lambda_c})\sqrt{Q_-}-\widetilde{h}_\perp(m_{\Lambda_b}-m_{\Lambda_c})\sqrt{Q_+}\Big], \tag{B.16}$$

$$H^{(T)+1/2}_{+1/2,+1,-1} = -C_T\Big[h_+\sqrt{Q_-}+\widetilde{h}_+\sqrt{Q_+}\Big], \tag{B.17}$$

$$H^{(T)-1/2}_{-1/2,+1,-1} = -C_T\Big[h_+\sqrt{Q_-}-\widetilde{h}_+\sqrt{Q_+}\Big]. \tag{B.18}$$

The other non-vanishing helicity amplitudes of tensor type are related to the above by

$$H^{(T)\lambda_{\Lambda_b}}_{\lambda_{\Lambda_c},\lambda,\lambda'} = -H^{(T)\lambda_{\Lambda_b}}_{\lambda_{\Lambda_c},\lambda',\lambda}. \tag{B.19}$$

Appendix C

$f_i(q^2)$ for different observables used in Chapter 3:

In the following tables, the various $f_i(q^2)$ for different observables used in our analysis are shown [153].

Obs / f_i	$R(D)$	P_τ^R
f_1	$\mathcal{G}\left(\left(1+\frac{m_\tau^2}{2q^2}\right){H_{V,0}^s}^2+\frac{3}{2}\frac{m_\tau^2}{q^2}{H_{V,t}^s}^2\right)$	$\mathcal{G}\left(\left(-1+\frac{m_\tau^2}{2q^2}\right){H_{V,0}^s}^2+\frac{3}{2}\frac{m_\tau^2}{q^2}{H_{V,t}^s}^2\right)$
f_2	$\frac{3}{2}\mathcal{G}{H_S^s}^2$	$\frac{3}{2}\mathcal{G}{H_S^s}^2$
f_3	$8\mathcal{G}\left(1+\frac{2m_\tau^2}{q^2}\right){H_T^s}^2$	$8\mathcal{G}\left(1-\frac{2m_\tau^2}{q^2}\right){H_T^s}^2$
f_4	$3\mathcal{G}\frac{m_\tau}{\sqrt{q^2}}H_S^sH_{V,t}^s$	$3\mathcal{G}\frac{m_\tau}{\sqrt{q^2}}H_S^sH_{V,t}^s$
f_5	$-12\mathcal{G}\frac{m_\tau}{\sqrt{q^2}}H_T^sH_{V,0}^s$	$4\mathcal{G}\frac{m_\tau}{\sqrt{q^2}}H_T^sH_{V,0}^s$

TABLE C.1: f_is for $R(D)$ and τ polarisation asymmetry in $B \to D\tau\nu_\tau$.

Obs / f_i	$R(D^*)$	$P_\tau^{R^*}$
f_1	$\mathcal{G}^*\left(\left(1+\frac{m_\tau^2}{2q^2}\right)\left(H_{V,+}^2+H_{V,-}^2+H_{V,0}^2\right)+\frac{3}{2}\frac{m_\tau^2}{q^2}H_{V,t}^2\right)$	$\mathcal{G}^*\left(\left(-1+\frac{m_\tau^2}{2q^2}\right)\left(H_{V,+}^2+H_{V,-}^2+H_{V,0}^2\right)+\frac{3}{2}\frac{m_\tau^2}{q^2}H_{V,t}^2\right)$
f_2	$-2\mathcal{G}^*\left(\left(1+\frac{m_\tau^2}{2q^2}\right)\left(H_{V,0}^2+2H_{V,+}H_{V,-}\right)+\frac{3}{2}\frac{m_\tau^2}{q^2}H_{V,t}^2\right)$	$\mathcal{G}^*\left(\left(2-\frac{m_\tau^2}{q^2}\right)\left(H_{V,0}^2+2H_{V,+}H_{V,-}\right)-3\frac{m_\tau^2}{q^2}H_{V,t}^2\right)$
f_3	$\frac{3}{2}\mathcal{G}^*H_S^2$	$\frac{3}{2}\mathcal{G}^*H_S^2$
f_4	$8\mathcal{G}^*\left(\left(1+\frac{2m_\tau^2}{q^2}\right)\left(H_{T,+}^2+H_{T,-}^2+H_{T,0}^2\right)\right)$	$8\mathcal{G}^*\left(\left(1-\frac{2m_\tau^2}{q^2}\right)\left(H_{T,+}^2+H_{T,-}^2+H_{T,0}^2\right)\right)$
f_5	$3\mathcal{G}^*\frac{m_\tau}{\sqrt{q^2}}H_SH_{V,t}$	$3\mathcal{G}^*\frac{m_\tau}{\sqrt{q^2}}H_SH_{V,t}$
f_6	$-12\mathcal{G}^*\frac{m_\tau}{\sqrt{q^2}}\left(H_{T,0}H_{V,0}+H_{T,+}H_{V,+}-H_{T,-}H_{V,-}\right)$	$4\mathcal{G}^*\frac{m_\tau}{\sqrt{q^2}}\left(H_{T,0}H_{V,0}+H_{T,+}H_{V,+}-H_{T,-}H_{V,-}\right)$
f_7	$12\mathcal{G}^*\frac{m_\tau}{\sqrt{q^2}}\left(H_{T,0}H_{V,0}+H_{T,+}H_{V,-}-H_{T,-}H_{V,+}\right)$	$-4\mathcal{G}^*\frac{m_\tau}{\sqrt{q^2}}\left(H_{T,0}H_{V,0}+H_{T,+}H_{V,-}-H_{T,-}H_{V,+}\right)$

TABLE C.2: f_is for R_{D^*} and τ polarisation asymmetry in $B \to D^*\tau\nu_\tau$.

Obs / f_i	$\mathcal{A}_{\mathcal{FB}}^{\mathcal{R}}$	$\mathcal{A}_{\mathcal{FB}}^{\mathcal{R}^*}$	$P_{D^*}^R$
f_1	$\mathcal{F}\left(\frac{m_\tau^2}{q^2}H_{V,0}^sH_{V,t}^s\right)$	$\frac{1}{2}\mathcal{F}^*\left(H_{V,+}^2-H_{V,-}^2\right)$	$\mathcal{G}^*\left(\left(1+\frac{m_\tau^2}{2q^2}\right)H_{V,0}^2+\frac{3}{2}\frac{m_\tau^2}{q^2}H_{V,t}^2\right)$
f_2	$\mathcal{F}\left(\frac{m_\tau}{\sqrt{q^2}}H_{V,0}^sH_S^s\right)$	$\mathcal{F}^*\frac{m_\tau^2}{q^2}H_{V,0}H_{V,t}$	$\frac{3}{2}\mathcal{G}^*H_S^2$
f_3	$-4\mathcal{F}\left(\frac{m_\tau}{\sqrt{q^2}}H_{V,t}^sH_T^s\right)$	$8\mathcal{F}^*\frac{m_\tau^2}{q^2}\left(H_{T,+}^2-H_{T,-}^2\right)$	$8\mathcal{G}^*\left(1+\frac{2m_\tau^2}{q^2}\right)H_{T,0}^2$
f_4	$-4\mathcal{F}H_S^sH_T^s$	$\mathcal{F}^*\frac{m_\tau}{\sqrt{q^2}}H_SH_{V,0}$	$3\mathcal{G}^*\frac{m_\tau}{\sqrt{q^2}}H_SH_{V,t}$
f_5	–	$-4\mathcal{F}^*\frac{m_\tau}{\sqrt{q^2}}\left(H_{T,0}H_{V,t}+H_{T,+}H_{V,+}+H_{T,-}H_{V,-}\right)$	$-12\mathcal{G}^*\frac{m_\tau}{\sqrt{q^2}}H_{T,0}H_{V,0}$
f_6	–	$4\mathcal{F}^*\frac{m_\tau}{\sqrt{q^2}}\left(H_{T,0}H_{V,t}+H_{T,+}H_{V,-}+H_{T,-}H_{V,+}\right)$	–
f_7	–	$-4\mathcal{F}^*H_{T,0}H_S$	–

TABLE C.3: f_is for τ forward-backward asymmetries in $B \to D^{(*)}\tau\nu_\tau$ decays, and D^* polarisation asymmetry in $B \to D^*\tau\nu_\tau$.

The expressions for $\mathcal{F}$, $\mathcal{F}^*$, $\mathcal{G}$, $\mathcal{G}^*$ are given by [67]

$$
\begin{aligned}
\mathcal{G} &= \frac{\tau_B}{\mathcal{B}(B\to Dl\nu)}\frac{G_F^2|V_{cb}|^2}{192\pi^3m_B^3}q^2\sqrt{\lambda_D(q^2)}\left(1-\frac{m_\tau^2}{q^2}\right)^2, \\
\mathcal{G}^* &= \frac{\tau_B}{\mathcal{B}(B\to D^*l\nu)}\frac{G_F^2|V_{cb}|^2}{192\pi^3m_B^3}q^2\sqrt{\lambda_{D^*}(q^2)}\left(1-\frac{m_\tau^2}{q^2}\right)^2 \\
\mathcal{F} &= \frac{\tau_B}{\mathcal{B}(B\to Dl\nu)}\frac{G_F^2|V_{cb}|^2}{128\pi^3m_B^3}q^2\sqrt{\lambda_D(q^2)}\left(1-\frac{m_\tau^2}{q^2}\right)^2 \\
\mathcal{F}^* &= \frac{\tau_B}{\mathcal{B}(B\to D^*l\nu)}\frac{G_F^2|V_{cb}|^2}{128\pi^3m_B^3}q^2\sqrt{\lambda_{D^*}(q^2)}\left(1-\frac{m_\tau^2}{q^2}\right)^2 \qquad \text{(C.1)}
\end{aligned}
$$

Bibliography

[1] S. L. Glashow, Nucl. Phys. **22** (1961) 579. doi:10.1016/0029-5582(61)90469-2

[2] S. Weinberg, Phys. Rev. Lett. **19** (1967) 1264. doi:10.1103/PhysRevLett.19.1264

[3] A. Salam, Conf. Proc. C **680519** (1968) 367.

[4] F. Englert and R. Brout, Phys. Rev. Lett. **13** (1964) 321. doi:10.1103/PhysRevLett.13.321

[5] P. W. Higgs, Phys. Rev. Lett. **13** (1964) 508. doi:10.1103/PhysRevLett.13.508

[6] G. Aad *et al.* [ATLAS Collaboration], Phys. Lett. B **716** (2012) 1 doi:10.1016/j.physletb.2012.08.020 [arXiv:1207.7214 [hep-ex]].

[7] S. Chatrchyan *et al.* [CMS Collaboration], Phys. Lett. B **716** (2012) 30 doi:10.1016/j.physletb.2012.08.021 [arXiv:1207.7235 [hep-ex]].

[8] R. Oerter, New York, USA: Pi Pr. (2006) 327 p

[9] S. Fukuda *et al.* [Super-Kamiokande Collaboration], Phys. Lett. B **539**, 179 (2002) [hep-ex/0205075]; P. Adamson *et al.* [MINOS Collaboration], Phys. Rev. Lett. **106**, 181801 (2011) [arXiv:1103.0340 [hep-ex]]; T. Araki *et al.* [KamLAND Collaboration], Phys. Rev. Lett. **94**, 081801 (2005) [hep-ex/0406035].

[10] Weinberg, Steven (1972). Gravitation and Cosmology: Principles and Applications of the General Theory of Relativity. New York: Wiley.

[11] P. A. R. Ade *et al.* [Planck Collaboration], Astron. Astrophys. **571** (2014) A16 doi:10.1051/0004-6361/201321591 [arXiv:1303.5076 [astro-ph.CO]].

[12] M. Fukugita and T. Yanagida, Phys. Lett. B **174** (1986) 45. doi:10.1016/0370-2693(86)91126-3

[13] M. Drees, hep-ph/9611409.

[14] Y. Grossman and M. P. Worah, Phys. Lett. B **395** (1997) 241 doi:10.1016/S0370-2693(97)00068-3 [hep-ph/9612269].

[15] M. Gronau and D. London, Phys. Rev. D **55** (1997) 2845 doi:10.1103/PhysRevD.55.2845 [hep-ph/9608430].

[16] M. Neubert, Phys. Lett. B **513** (2001) 88 doi:10.1016/S0370-2693(01)00668-2 [hep-ph/0104280].

[17] A. K. Leibovich, I. Low and I. Z. Rothstein, Phys. Lett. B **513** (2001) 83 doi:10.1016/S0370-2693(01)00667-0 [hep-ph/0105066].

[18] A. H. Hoang, Z. Ligeti and M. Luke, Phys. Rev. D **71** (2005) 093007 doi:10.1103/PhysRevD.71.093007 [hep-ph/0502134].

[19] B. O. Lange, JHEP **0601** (2006) 104 doi:10.1088/1126-6708/2006/01/104 [hep-ph/0511098].

[20] J. M. Flynn, T. Izubuchi, T. Kawanai, C. Lehner, A. Soni, R. S. Van de Water and O. Witzel, Phys. Rev. D **91** (2015) no.7, 074510 doi:10.1103/PhysRevD.91.074510 [arXiv:1501.05373 [hep-lat]].

[21] M. C. Arnesen, B. Grinstein, I. Z. Rothstein and I. W. Stewart, Phys. Rev. Lett. **95** (2005) 071802 doi:10.1103/PhysRevLett.95.071802 [hep-ph/0504209].

[22] Y. Amhis *et al.* [HFLAV Collaboration], Eur. Phys. J. C **77** (2017) no.12, 895 doi:10.1140/epjc/s10052-017-5058-4 [arXiv:1612.07233 [hep-ex]].

[23] A. Alberti, P. Gambino, K. J. Healey and S. Nandi, Nucl. Part. Phys. Proc. **273-275** (2016) 1325. doi:10.1016/j.nuclphysbps.2015.09.212

[24] D. Bigi, P. Gambino and S. Schacht, Phys. Lett. B **769** (2017) 441 doi:10.1016/j.physletb.2017.04.022 [arXiv:1703.06124 [hep-ph]].

[25] D. Bigi, P. Gambino and S. Schacht, JHEP **1711** (2017) 061 doi:10.1007/JHEP11(2017)061 [arXiv:1707.09509 [hep-ph]].

[26] S. Jaiswal, S. Nandi and S. K. Patra, JHEP **1712** (2017) 060 doi:10.1007/JHEP12(2017)060 [arXiv:1707.09977 [hep-ph]].

[27] A. Pich, NATO Sci. Ser. B **363** (1997) 173 [hep-ph/9701263].

[28] Y. Nir, CERN-2015-001, pp.123-156 doi:10.5170/CERN-2015-001.123 [arXiv:1605.00433 [hep-ph]].

[29] Y. Grossman and P. Tanedo, doi:10.1142/9789813233348-0004 arXiv:1711.03624 [hep-ph].

[30] B. Grinstein, arXiv:1501.05283 [hep-ph].

[31] Z. Ligeti, doi:10.1142/9789814678766-0006 arXiv:1502.01372 [hep-ph].

[32] S. J. Lee and H. Serdio, doi:10.23730/CYRSP-2017-002.125 arXiv:1504.07549 [hep-ph].

[33] N. Cabibbo, Phys. Rev. Lett. **10** (1963) 531. doi:10.1103/PhysRevLett.10.531

[34] M. Kobayashi and T. Maskawa, Prog. Theor. Phys. **49** (1973) 652. doi:10.1143/PTP.49.652

[35] L. L. Chau and W. Y. Keung, Phys. Rev. Lett. **53** (1984) 1802. doi:10.1103/PhysRevLett.53.1802

[36] L. Wolfenstein, Phys. Rev. Lett. **51** (1983) 1945. doi:10.1103/PhysRevLett.51.1945

[37] M. Jeitler [NA48 Collaboration], Nucl. Instrum. Meth. A **478** (2002) 404. doi:10.1016/S0168-9002(01)01784-3

[38] A. Aloisio *et al.* [KLOE Collaboration], LNF-93-002-IR.

[39] G. Amelino-Camelia *et al.*, Eur. Phys. J. C **68** (2010) 619 doi:10.1140/epjc/s10052-010-1351-1 [arXiv:1003.3868 [hep-ex]].

[40] H. Albrecht *et al.* [ARGUS Collaboration], Nucl. Instrum. Meth. A **275** (1989) 1. doi:10.1016/0168-9002(89)90334-3

[41] D. Andrews *et al.* [CLEO Collaboration], Nucl. Instrum. Meth. **211** (1983) 47. doi:10.1016/0167-5087(83)90556-2

[42] B. Aubert *et al.* [BaBar Collaboration], Nucl. Instrum. Meth. A **479** (2002) 1 doi:10.1016/S0168-9002(01)02012-5 [hep-ex/0105044].

[43] A. Abashian *et al.*, Nucl. Instrum. Meth. A **479** (2002) 117. doi:10.1016/S0168-9002(01)02013-7

[44] T. Kuhr, Springer Tracts Mod. Phys. **249** (2013) 1. doi:10.1007/978-3-642-10300-1

[45] T. Abe *et al.* [Belle-II Collaboration], arXiv:1011.0352 [physics.ins-det].

[46] G. Aad *et al.* [ATLAS Collaboration], JINST **3** (2008) S08003. doi:10.1088/1748-0221/3/08/S08003

[47] S. Chatrchyan *et al.* [CMS Collaboration], JINST **3** (2008) S08004. doi:10.1088/1748-0221/3/08/S08004

[48] M. Ablikim *et al.* [BESIII Collaboration], Nucl. Instrum. Meth. A **614** (2010) 345 doi:10.1016/j.nima.2009.12.050 [arXiv:0911.4960 [physics.ins-det]].

[49] S. Descotes-Genon and P. Koppenburg, Ann. Rev. Nucl. Part. Sci. **67** (2017) 97 doi:10.1146/annurev-nucl-101916-123109 [arXiv:1702.08834 [hep-ex]].

[50] R. Aaij *et al.* [LHCb Collaboration], Phys. Rev. Lett. **115** (2015) no.3, 031601 doi:10.1103/PhysRevLett.115.031601 [arXiv:1503.07089 [hep-ex]].

[51] A. Hocker, H. Lacker, S. Laplace and F. Le Diberder, Eur. Phys. J. C **21** (2001) 225 doi:10.1007/s100520100729 [hep-ph/0104062].

[52] M. Gronau and D. London, Phys. Lett. B **253** (1991) 483. doi:10.1016/0370-2693(91)91756-L

[53] M. Gronau and D. Wyler, Phys. Lett. B **265** (1991) 172. doi:10.1016/0370-2693(91)90034-N

[54] D. Atwood, I. Dunietz and A. Soni, Phys. Rev. Lett. **78** (1997) 3257 doi:10.1103/PhysRevLett.78.3257 [hep-ph/9612433].

[55] D. Atwood, I. Dunietz and A. Soni, Phys. Rev. D **63** (2001) 036005 doi:10.1103/PhysRevD.63.036005 [hep-ph/0008090].

[56] A. Giri, Y. Grossman, A. Soffer and J. Zupan, Phys. Rev. D **68** (2003) 054018 doi:10.1103/PhysRevD.68.054018 [hep-ph/0303187].

[57] C. Alpigiani *et al.*, arXiv:1710.09644 [hep-ph].

[58] M. A. Shifman, A. I. Vainshtein and V. I. Zakharov, Nucl. Phys. B **147** (1979) 385. doi:10.1016/0550-3213(79)90022-1

[59] M. A. Shifman, A. I. Vainshtein and V. I. Zakharov, Nucl. Phys. B **147** (1979) 448. doi:10.1016/0550-3213(79)90023-3

[60] A. G. Grozin, hep-ph/9908366.

[61] M. Tanaka, Z. Phys. C **67** (1995) 321 doi:10.1007/BF01571294 [hep-ph/9411405].

[62] U. Nierste, S. Trine and S. Westhoff, Phys. Rev. D **78** (2008) 015006 doi:10.1103/PhysRevD.78.015006 [arXiv:0801.4938 [hep-ph]].

[63] M. Tanaka and R. Watanabe, Phys. Rev. D **82** (2010) 034027 doi:10.1103/PhysRevD.82.034027 [arXiv:1005.4306 [hep-ph]].

[64] S. Davidson, D. C. Bailey and B. A. Campbell, Z. Phys. C **61** (1994) 613 doi:10.1007/BF01552629 [hep-ph/9309310].

[65] E. Ponton, arXiv:1207.3827 [hep-ph].

[66] Y. Sakaki, M. Tanaka, A. Tayduganov and R. Watanabe, Phys. Rev. D **91**, no. 11, 114028 (2015) [arXiv:1412.3761 [hep-ph]].

[67] Y. Sakaki, M. Tanaka, A. Tayduganov and R. Watanabe, Phys. Rev. D **88**, no. 9, 094012 (2013) [arXiv:1309.0301 [hep-ph]].

[68] I. Caprini, L. Lellouch and M. Neubert, Nucl. Phys. B **530**, 153 (1998) doi:10.1016/S0550-3213(98)00350-2 [hep-ph/9712417].

[69] F. U. Bernlochner, Z. Ligeti, M. Papucci and D. J. Robinson, Phys. Rev. D **95** (2017) no.11, 115008 Erratum: [Phys. Rev. D **97** (2018) no.5, 059902] doi:10.1103/PhysRevD.95.115008, 10.1103/PhysRevD.97.059902 [arXiv:1703.05330 [hep-ph]].

[70] C. G. Boyd, B. Grinstein and R. F. Lebed, Phys. Rev. D **56** (1997) 6895 doi:10.1103/PhysRevD.56.6895 [hep-ph/9705252].

[71] J. A. Bailey *et al.* [MILC Collaboration], Phys. Rev. D **92**, no. 3, 034506 (2015) doi:10.1103/PhysRevD.92.034506 [arXiv:1503.07237 [hep-lat]].

[72] Y. Amhis *et al.* [Heavy Flavor Averaging Group (HFAG) Collaboration], arXiv:1412.7515 [hep-ex].

[73] H. Na *et al.* [HPQCD Collaboration], Phys. Rev. D **92**, no. 5, 054510 (2015) Erratum: [Phys. Rev. D **93**, no. 11, 119906 (2016)] doi:10.1103/PhysRevD.93.119906, 10.1103/PhysRevD.92.054510 [arXiv:1505.03925 [hep-lat]].

[74] D. Bigi and P. Gambino, Phys. Rev. D **94** (2016) no.9, 094008 doi:10.1103/PhysRevD.94.094008 [arXiv:1606.08030 [hep-ph]].

[75] S. Fajfer, J. F. Kamenik and I. Nisandzic, Phys. Rev. D **85**, 094025 (2012) [arXiv:1203.2654 [hep-ph]].

[76] J. A. Bailey *et al.* [Fermilab Lattice and MILC Collaborations], Phys. Rev. D **89**, no. 11, 114504 (2014) doi:10.1103/PhysRevD.89.114504 [arXiv:1403.0635 [hep-lat]].

[77] W. F. Wang, Y. Y. Fan and Z. J. Xiao, Chin. Phys. C **37** (2013) 093102 doi:10.1088/1674-1137/37/9/093102 [arXiv:1212.5903 [hep-ph]].

[78] A. Y. Anisimov, I. M. Narodetsky, C. Semay and B. Silvestre-Brac, Phys. Lett. B **452** (1999) 129 doi:10.1016/S0370-2693(99)00273-7 [hep-ph/9812514].

[79] D. Ebert, R. N. Faustov and V. O. Galkin, Phys. Rev. D **68** (2003) 094020 doi:10.1103/PhysRevD.68.094020 [hep-ph/0306306].

[80] E. Hernandez, J. Nieves and J. M. Verde-Velasco, Phys. Rev. D **74** (2006) 074008 doi:10.1103/PhysRevD.74.074008 [hep-ph/0607150].

[81] V. V. Kiselev, hep-ph/0211021.

[82] M. A. Ivanov, J. G. Korner and P. Santorelli, Phys. Rev. D **73** (2006) 054024 doi:10.1103/PhysRevD.73.054024 [hep-ph/0602050].

[83] W. Wang, Y. L. Shen and C. D. Lu, Phys. Rev. D **79** (2009) 054012 doi:10.1103/PhysRevD.79.054012 [arXiv:0811.3748 [hep-ph]].

[84] A. Lytle, B. Colquhoun, C. Davies, J. Koponen and C. McNeile, PoS BEAUTY **2016**, 069 (2016) doi:10.22323/1.273.0069 [arXiv:1605.05645 [hep-lat]].

[85] A. Datta, S. Kamali, S. Meinel and A. Rashed, JHEP **1708**, 131 (2017) doi:10.1007/JHEP08(2017)131 [arXiv:1702.02243 [hep-ph]].

[86] F. Cardarelli and S. Simula, Phys. Lett. B **421**, 295 (1998) doi:10.1016/S0370-2693(97)01581-5 [hep-ph/9711207].

[87] H. G. Dosch, E. Ferreira, M. Nielsen and R. Rosenfeld, Phys. Lett. B **431**, 173 (1998) doi:10.1016/S0370-2693(98)00566-8 [hep-ph/9712350].

[88] C. S. Huang, C. F. Qiao and H. G. Yan, Phys. Lett. B **437**, 403 (1998) doi:10.1016/S0370-2693(98)00909-5 [hep-ph/9805452].

[89] R. S. Marques de Carvalho, F. S. Navarra, M. Nielsen, E. Ferreira and H. G. Dosch, Phys. Rev. D **60**, 034009 (1999) doi:10.1103/PhysRevD.60.034009 [hep-ph/9903326].

[90] M. q. Huang and D. W. Wang, Phys. Rev. D **69**, 094003 (2004) doi:10.1103/PhysRevD.69.094003 [hep-ph/0401094].

[91] M. Pervin, W. Roberts and S. Capstick, Phys. Rev. C **72**, 035201 (2005) doi:10.1103/PhysRevC.72.035201 [nucl-th/0503030].

[92] H. W. Ke, X. Q. Li and Z. T. Wei, Phys. Rev. D **77**, 014020 (2008) doi:10.1103/PhysRevD.77.014020 [arXiv:0710.1927 [hep-ph]].

[93] Y. M. Wang, Y. L. Shen and C. D. Lu, Phys. Rev. D **80**, 074012 (2009) doi:10.1103/PhysRevD.80.074012 [arXiv:0907.4008 [hep-ph]].

[94] K. Azizi, M. Bayar, Y. Sarac and H. Sundu, Phys. Rev. D **80**, 096007 (2009) doi:10.1103/PhysRevD.80.096007 [arXiv:0908.1758 [hep-ph]].

[95] A. Khodjamirian, C. Klein, T. Mannel and Y.-M. Wang, JHEP **1109**, 106 (2011) doi:10.1007/JHEP09(2011)106 [arXiv:1108.2971 [hep-ph]].

[96] T. Gutsche, M. A. Ivanov, J. G. Krner, V. E. Lyubovitskij and P. Santorelli, Phys. Rev. D **90**, no. 11, 114033 (2014) Erratum: [Phys. Rev. D **94**, no. 5, 059902 (2016)] doi:10.1103/PhysRevD.90.114033, 10.1103/PhysRevD.94.059902 [arXiv:1410.6043 [hep-ph]].

[97] T. Gutsche, M. A. Ivanov, J. G. Krner, V. E. Lyubovitskij, P. Santorelli and N. Habyl, Phys. Rev. D **91**, no. 7, 074001 (2015) Erratum: [Phys. Rev. D **91**, no. 11, 119907 (2015)] doi:10.1103/PhysRevD.91.074001, 10.1103/PhysRevD.91.119907 [arXiv:1502.04864 [hep-ph]].

[98] W. Detmold, C. Lehner and S. Meinel, Phys. Rev. D **92**, no. 3, 034503 (2015) doi:10.1103/PhysRevD.92.034503 [arXiv:1503.01421 [hep-lat]].

[99] A. Alberti, P. Gambino, K. J. Healey and S. Nandi, Phys. Rev. Lett. **114**, no. 6, 061802 (2015) doi:10.1103/PhysRevLett.114.061802 [arXiv:1411.6560 [hep-ph]].

[100] M. Trott, Phys. Rev. D **70** (2004) 073003 doi:10.1103/PhysRevD.70.073003 [hep-ph/0402120].

[101] V. Aquila, P. Gambino, G. Ridolfi and N. Uraltsev, Nucl. Phys. B **719** (2005) 77 doi:10.1016/j.nuclphysb.2005.04.031 [hep-ph/0503083].

[102] A. Pak and A. Czarnecki, Phys. Rev. Lett. **100** (2008) 241807 doi:10.1103/PhysRevLett.100.241807 [arXiv:0803.0960 [hep-ph]].

[103] K. Melnikov, Phys. Lett. B **666** (2008) 336 doi:10.1016/j.physletb.2008.07.089 [arXiv:0803.0951 [hep-ph]].

[104] S. Biswas and K. Melnikov, JHEP **1002** (2010) 089 doi:10.1007/JHEP02(2010)089 [arXiv:0911.4142 [hep-ph]].

[105] P. Gambino, JHEP **1109** (2011) 055 doi:10.1007/JHEP09(2011)055 [arXiv:1107.3100 [hep-ph]].

[106] I. I. Y. Bigi, N. G. Uraltsev and A. I. Vainshtein, Phys. Lett. B **293** (1992) 430 Erratum: [Phys. Lett. B **297** (1992) 477] doi:10.1016/0370-2693(92)90908-M, 10.1016/0370-2693(92)91287-J [hep-ph/9207214].

[107] B. Blok, L. Koyrakh, M. A. Shifman and A. I. Vainshtein, Phys. Rev. D **49** (1994) 3356 Erratum: [Phys. Rev. D **50** (1994) 3572] doi:10.1103/PhysRevD.50.3572, 10.1103/PhysRevD.49.3356 [hep-ph/9307247].

[108] A. V. Manohar and M. B. Wise, Phys. Rev. D **49** (1994) 1310 doi:10.1103/PhysRevD.49.1310 [hep-ph/9308246].

[109] M. Gremm and A. Kapustin, Phys. Rev. D **55** (1997) 6924 doi:10.1103/PhysRevD.55.6924 [hep-ph/9603448].

[110] T. Mannel, A. V. Rusov and F. Shahriaran, Nucl. Phys. B **921**, 211 (2017) doi:10.1016/j.nuclphysb.2017.05.016 [arXiv:1702.01089 [hep-ph]].

[111] A. Czarnecki, M. Jezabek and J. H. Kuhn, Phys. Lett. B **346**, 335 (1995) doi:10.1016/0370-2693(94)01681-2 [hep-ph/9411282].

[112] A. F. Falk, Z. Ligeti, M. Neubert and Y. Nir, Phys. Lett. B **326**, 145 (1994) doi:10.1016/0370-2693(94)91206-8 [hep-ph/9401226].

[113] W. D. Goldberger, hep-ph/9902311.

[114] S. Kamali, A. Rashed and A. Datta, Phys. Rev. D **97**, no. 9, 095034 (2018) doi:10.1103/PhysRevD.97.095034 [arXiv:1801.08259 [hep-ph]].

[115] P. Colangelo and F. De Fazio, JHEP **1806**, 082 (2018) doi:10.1007/JHEP06(2018)082 [arXiv:1801.10468 [hep-ph]].

[116] M. Gonzlez-Alonso and J. Martin Camalich, JHEP **1612** (2016) 052 doi:10.1007/JHEP12(2016)052 [arXiv:1605.07114 [hep-ph]].

[117] R. Alonso, B. Grinstein and J. Martin Camalich, Phys. Rev. Lett. **118** (2017) no.8, 081802 doi:10.1103/PhysRevLett.118.081802 [arXiv:1611.06676 [hep-ph]].

[118] J. P. Lees *et al.* [BaBar Collaboration], Phys. Rev. D **88** (2013) no.7, 072012 doi:10.1103/PhysRevD.88.072012 [arXiv:1303.0571 [hep-ex]].

[119] M. Huschle *et al.* [Belle Collaboration], Phys. Rev. D **92** (2015) no.7, 072014 doi:10.1103/PhysRevD.92.072014 [arXiv:1507.03233 [hep-ex]].

[120] A. Abdesselam *et al.* [Belle Collaboration], arXiv:1603.06711 [hep-ex].

[121] S. Hirose *et al.* [Belle Collaboration], Phys. Rev. Lett. **118** (2017) no.21, 211801 doi:10.1103/PhysRevLett.118.211801 [arXiv:1612.00529 [hep-ex]].

[122] R. Aaij *et al.* [LHCb Collaboration], Phys. Rev. Lett. **115** (2015) no.11, 111803 Erratum: [Phys. Rev. Lett. **115** (2015) no.15, 159901] doi:10.1103/PhysRevLett.115.159901, 10.1103/PhysRevLett.115.111803 [arXiv:1506.08614 [hep-ex]].

[123] R. Aaij *et al.* [LHCb Collaboration], Phys. Rev. D **97** (2018) no.7, 072013 doi:10.1103/PhysRevD.97.072013 [arXiv:1711.02505 [hep-ex]].

[124] R. Aaij *et al.* [LHCb Collaboration], Phys. Rev. Lett. **120** (2018) no.12, 121801 doi:10.1103/PhysRevLett.120.121801 [arXiv:1711.05623 [hep-ex]].

[125] C. Bourrely, I. Caprini and L. Lellouch, Phys. Rev. D **79** (2009) 013008 Erratum: [Phys. Rev. D **82** (2010) 099902] doi:10.1103/PhysRevD.82.099902, 10.1103/PhysRevD.79.013008 [arXiv:0807.2722 [hep-ph]].

[126] I. P. Gouz, V. V. Kiselev, A. K. Likhoded, V. I. Romanovsky and O. P. Yushchenko, Phys. Atom. Nucl. **67** (2004) 1559 [Yad. Fiz. **67** (2004) 1581] doi:10.1134/1.1788046 [hep-ph/0211432].

[127] A. G. Akeroyd and C. H. Chen, Phys. Rev. D **96** (2017) no.7, 075011 doi:10.1103/PhysRevD.96.075011 [arXiv:1708.04072 [hep-ph]].

[128] M. Acciarri *et al.* [L3 Collaboration], Phys. Lett. B **396** (1997) 327. doi:10.1016/S0370-2693(97)00138-X

[129] M. Diehl and O. Nachtmann, Z. Phys. C **62** (1994) 397. doi:10.1007/BF01555899

[130] D. Atwood and A. Soni, Phys. Rev. D **45** (1992) 2405. doi:10.1103/PhysRevD.45.2405

[131] J. F. Gunion, B. Grzadkowski and X. G. He, Phys. Rev. Lett. **77**, 5172 (1996) [hep-ph/9605326].

[132] M. Diehl and O. Nachtmann, Eur. Phys. J. C **1**, 177 (1998) [hep-ph/9702208].

[133] R. Andrae, T. Schulze-Hartung and P. Melchior, arXiv:1012.3754 [astro-ph.IM].

[134] S. S. Shapiro and M. B. Wilk, Biometrika **52**(3-4): 591-611 (1965) doi:10.1093/biomet/52.3-4.591

[135] P. Royston, *Journal of the Royal Statistical Society. Series C (Applied Statistics)*, **44**, No. 4 (1995), 547-551 doi:10.2307/2986146

[136] N. M. Razali and Y. B. Wah, *Journal of Statistical Modelling and Analysis*, **2**, No.1, 21-33, (2011)
M. Mendes and A. Pala, Pak. J. Inform. and Technol., **2** (2): 135-139, (2003)

S. Keskin, J. Appl. Sci. Res., **2**(5): 296-300, (2006)

N. A. Ahad, T. S. Yin, A. R. Othman and C. R. Yaacob *Sains Malaysiana* **40**(6)(2011): 637641

[137] S. S. Wilks, Annals Math. Statist. **9** (1938) no.1, 60. doi:10.1214/aoms/1177732360

[138] Schwarz, Gideon E. (1978), "Estimating the dimension of a model", *Annals of Statistics*, **6** (2): 461464, doi:10.1214/aos/1176344136, MR 468014.

[139] Shibata, Ritei. "An Optimal Selection of Regression Variables." Biometrika 68, no. 1 (1981): 45-54.

[140] Box, G.E.P., and Jenkins, G.M. (1970). *Time series analysis: forecasting and control.* Holden-Day, London.

[141] Breiman L. (1992). The little bootstrap and other methods for dimensionality selection in regression: X-fixed prediction error. *Journal of the American Statistical Association* **87**, 738754.

[142] Akaike, H. (1973). Information theory as an extension of the maximum likelihood principle. Pages 267281 in B. N. Petrov, and F. Csaki, (eds.) *Second International Symposium on Information Theory.* Akademiai Kiado, Budapest.

[143] Sugiura, N. (1978). Further analysis of the data by Akaikes information criterion and the finite corrections. *Communications in Statistics, Theory and Methods* **A7**, 1326.

[144] Akaike, H. (1983). Information measures and model selection. *International Statistical Institute* **44**, 277291.

[145] M. Davier, L. Duflot, F. Le Diberder and A. Rouge, Phys. Lett. B **306**, 411 (1993).

[146] B. Grzadkowski, Z. Hioki, K. Ohkuma and J. Wudka, Phys. Lett. B **593**, 189 (2004) [hep-ph/0403174].

[147] Z. Calcuttawala, A. Kundu, S. Nandi and S. K. Patra, Eur. Phys. J. C **77** (2017) no.9, 650 doi:10.1140/epjc/s10052-017-5227-5 [arXiv:1702.06679 [hep-ph]].

[148] Z. Calcuttawala, A. Kundu, S. Nandi and S. Kumar Patra, Phys. Rev. D **97** (2018) no.9, 095009 doi:10.1103/PhysRevD.97.095009 [arXiv:1802.09218 [hep-ph]].

[149] M. Tanaka, Z. Phys. C **67**, 321 (1995) [hep-ph/9411405].

[150] M. Duraisamy, P. Sharma and A. Datta, Phys. Rev. D **90**, no. 7, 074013 (2014) [arXiv:1405.3719 [hep-ph]].

[151] M. Tanaka and R. Watanabe, Phys. Rev. D **87**, no. 3, 034028 (2013) [arXiv:1212.1878 [hep-ph]].

[152] M. Freytsis, Z. Ligeti and J. T. Ruderman, Phys. Rev. D **92**, no. 5, 054018 (2015) doi:10.1103/PhysRevD.92.054018 [arXiv:1506.08896 [hep-ph]].

[153] S. Bhattacharya, S. Nandi and S. K. Patra, Phys. Rev. D **93**, no. 3, 034011 (2016) doi:10.1103/PhysRevD.93.034011 [arXiv:1509.07259 [hep-ph]].

[154] M. Okamoto *et al.*, Nucl. Phys. Proc. Suppl. **140**, 461 (2005) [hep-lat/0409116]; J. A. Bailey *et al.* [Fermilab Lattice and MILC Collaborations], PoS LATTICE **2010**, 311 (2010) [arXiv:1011.2166 [hep-lat]]; Y. Amhis *et al.* [Heavy Flavor Averaging Group Collaboration], arXiv:1207.1158 [hep-ex].

[155] B. Aubert *et al.* [BaBar Collaboration], Phys. Rev. Lett. **104**, 011802 (2010) [arXiv:0904.4063 [hep-ex]].

[156] B. Aubert *et al.* [BaBar Collaboration], Phys. Rev. Lett. **100**, 151802 (2008) [arXiv:0712.3503 [hep-ex]].

[157] A. Abdesselam *et al.* [Belle Collaboration], arXiv:1603.06711 [hep-ex].

[158] A. Abdesselam *et al.*, arXiv:1608.06391 [hep-ex].

[159] S. Bhattacharya, S. Nandi and S. K. Patra, Phys. Rev. D **95**, no. 7, 075012 (2017) doi:10.1103/PhysRevD.95.075012 [arXiv:1611.04605 [hep-ph]].

[160] S. Fajfer, J. F. Kamenik and I. Nisandzic, Phys. Rev. D **85** (2012) 094025 doi:10.1103/PhysRevD.85.094025 [arXiv:1203.2654 [hep-ph]].

[161] K. A. Olive *et al.* [Particle Data Group Collaboration], Chin. Phys. C **38**, 090001 (2014). doi:10.1088/1674-1137/38/9/090001

[162] F. U. Bernlochner, Z. Ligeti, M. Papucci and D. J. Robinson, Phys. Rev. D **96**, no. 9, 091503 (2017) doi:10.1103/PhysRevD.96.091503 [arXiv:1708.07134 [hep-ph]].

[163] HFAG, Average of R(D) and R(D) for FPCP2017, http://www.slac.stanford.edu/xorg/ hflav/semi/fpcp17/RDRDs.html, accessed: 2010-09-30.

[164] D. Choudhury, A. Kundu, S. Nandi and S. K. Patra, Phys. Rev. D **95**, no. 3, 035021 (2017) doi:10.1103/PhysRevD.95.035021 [arXiv:1612.03517 [hep-ph]].

[165] A. Celis, M. Jung, X. Q. Li and A. Pich, Phys. Lett. B **771**, 168 (2017) doi:10.1016/j.physletb.2017.05.037 [arXiv:1612.07757 [hep-ph]].

[166] M. A. Ivanov, J. G. Krner and C. T. Tran, Phys. Rev. D **95**, no. 3, 036021 (2017) doi:10.1103/PhysRevD.95.036021 [arXiv:1701.02937 [hep-ph]].

[167] D. Buttazzo, A. Greljo, G. Isidori and D. Marzocca, JHEP **1711**, 044 (2017) doi:10.1007/JHEP11(2017)044 [arXiv:1706.07808 [hep-ph]].

[168] M. Gonzlez-Alonso, J. Martin Camalich and K. Mimouni, Phys. Lett. B **772**, 777 (2017) doi:10.1016/j.physletb.2017.07.003 [arXiv:1706.00410 [hep-ph]].

[169] A. Azatov, D. Bardhan, D. Ghosh, F. Sgarlata and E. Venturini, arXiv:1805.03209 [hep-ph].

[170] W. Altmannshofer, P. S. Bhupal Dev and A. Soni, Phys. Rev. D **96**, no. 9, 095010 (2017) doi:10.1103/PhysRevD.96.095010 [arXiv:1704.06659 [hep-ph]].

[171] J. Shang and J. E. Cavanaugh, Computational Statistics and Data Analysis 52, 2004 (2008).

[172] K. G. Chetyrkin, J. H. Kuhn, A. Maier, P. Maierhofer, P. Marquard, M. Steinhauser and C. Sturm, Phys. Rev. D **80**, 074010 (2009) doi:10.1103/PhysRevD.80.074010 [arXiv:0907.2110 [hep-ph]].

[173] A. Bazavov *et al.* [Fermilab Lattice and MILC and TUMQCD Collaborations], arXiv:1802.04248 [hep-lat].

[174] D. Benson, I. I. Bigi, T. Mannel and N. Uraltsev, Nucl. Phys. B **665**, 367 (2003) doi:10.1016/S0550-3213(03)00452-8 [hep-ph/0302262].

[175] K. Melnikov and T. v. Ritbergen, Phys. Lett. B **482**, 99 (2000) doi:10.1016/S0370-2693(00)00507-4 [hep-ph/9912391].